UNIVERSITÄT HAMBURG
DEPARTEMENT PHYSIK

Unidirectional photoluminescence emission of pierced microdisks

Dissertation
zur Erlangung des Doktorgrades
des Fachbereichs Physik
der Universität Hamburg

vorgelegt von
Fabian Wilde
aus Hamburg

Hamburg
2008

Gutachter der Dissertation: Professor Dr. D. Heitmann
Professor Dr. U. Merkt

Gutachter der Disputation: Professor Dr. D. Heitmann
Professor Dr. W. Hansen

Datum der Disputation: 7. November 2008

Vorsitzender des Prüfungsausschusses: Dr. T. Kipp

Vorsitzender des Promotionsausschusses: Professor Dr. R. Klanner

Dekan des Fakultät für Mathematik,
Informatik und Naturwissenschaften: Professor Dr. A. Frühwald

Abstract

Microdisks are optical semiconductor microresonators with very high optical qualities and they are easier to fabricate as compared to other microresonator systems. Light confinement in microdisks is a result of total reflection at the surface boundary in a thin, circularly shaped semiconductor slab. Light waves skimming along the circumference of the slab superpose with themselves after one roundtrip. For constructive interference the so-called *whispering-gallery modes* occur. The emitted light has no preferential direction in the plane of the slab due to the rotational symmetry of the microdisks. In order to generate a directional emission characteristic, this rotational symmetry has to be broken. Two methods for breaking the rotational symmetry have been reported so far: (i) a smooth alteration of the circular shape of the microdisk and (ii) the introduction of a scattering center in the circumference of the microdisk. Until now, the first method has been reported to lead to directional emission in more than one emission direction, whereas the second method yields good unidirectional emission characteristics, but leads to a dramatic decrease of the optical quality of the resonator. Theoretical works have shown that an air hole with a small distance to the circumference of the microdisk acts on some modes as a scattering center, while others are almost unaffected by the hole. A scattered mode has a unidirectional emission behavior whereas an unaffected mode shows uniform emission with a high quality factor. Two of these modes may interchange their characteristics under certain circumstances and hybridize into a mode with unidirectional emission *and* a high quality factor.

In this work semiconductor microdisks without and with an air hole were fabricated and investigated with a confocal micro-photoluminescence setup. First, a theoretical model is derived for the detailed analysis of the experimental results. It allows for the mode assignment and the calculation of field distributions. Afterwards the experimental confocal micro-photoluminescence setup is explained and special characteristics of this setup are discussed. The fabrication of microdisks is realized by wet-chemical etching processes that produces very smoothly etched surfaces and thus provides microdisks with high quality factors. An investigation on microdisks without an air hole and different radii gives the opportunity to compare the theoretical model with experimental results. Furthermore, microdisks with an air hole and a systematically varying hole distance are investigated with respect to their spatial emission behavior. Within this investigation a new method for detection of spatial emission behavior is introduced that allows for the investigation with a confocal setup without the need to rotate either the sample or the detector. With the help of the theoretical model and simulations the modes of all microdisks are assigned and investigated with respect to their emission spatial behavior. Our experiments strongly suggest a unidirectional emission behavior with very high quality factors for pierced microdisks.

Inhaltsangabe

Microdisks sind optische Halbleitermikroresonatoren, die sich durch besonders hohe optische Güten und vergleichsweise einfache Herstellung gegenüber anderen Mikroresonatorsystemen hervorheben. Der Lichteinschluss ergibt sich aus der Totalreflektion an den Außenwänden in einer dünnen, kreisförmigen Halbleiterscheibe. Am Rand der Scheibe umlaufendes Licht interferiert mit sich selbst nach einem Umlauf. Dabei bilden sich bei konstruktiver Überlagerung optische Moden aus, die so genannten *Whispering-Gallery Modes*. Durch die Rotationsymmetrie der Microdisks ergibt sich eine in der Scheibenebene ungerichtete Abstrahleigenschaft. Um eine gerichtete Abstrahlcharakteristik zu erzeugen, muss die Rotationssymmetrie gebrochen werden. Bisher ist von zwei Methoden zur Symmetriebrechung berichtet worden: (i) eine stetige Abweichung von der Kreisform der Microdisk und (ii) das Einbringen eines Streuzentrums auf dem Rand der Microdisk. Die erste Lösung führt nach bisherigen Erkenntnissen zwar zu gerichteter Abstrahlung, allerdings in mehr als einer einzigen Richtung. Letztere Methode birgt gute unidirektionale Abstrahleigenschaften, bringt jedoch meistens drastische Einbrüche in der optischen Güte des Resonators mit sich. Theoretische Arbeiten haben gezeigt, dass ein Luftloch mit einem kleinen Abstand vom Rand der Microdisk ein Streuzentrum nur für bestimmte Moden darstellt, während andere Moden nahezu unbeeinflusst sind. Die gestreute Mode hat eine unidirektionale Abstrahleigenschaft mit niedriger Güte, während die unbeeinflusste Mode gleichmässige Abstrahlung mit hoher Güte zeigt. Zwei solche Moden können unter Umständen ihre Eigenschaften tauschen und zu einer unidirektional abstrahlenden Mode mit hoher optischer Güte hybridisieren.

In dieser Arbeit wurden Halbleiter Microdisks sowohl ohne als auch mit Luftloch hergestellt und mit einem konfokalen Mikrophotolumineszenzaufbau untersucht. Zur genauen Untersuchung der experimentellen Ergebnisse wird zunächst ein theoretisches Modell hergeleitet, dass die Zuordnung von Moden und die Bestimmung der Feldverteilung in einer Microdisk ohne Luftloch erlaubt. Anschließend werden der experimentelle konfokale Mikrophotolumineszenzaufbau beschrieben und auf besondere Eigenschaften unserer Messapparatur eingegangen. Zur Herstellung der Microdisks wird ein nasschemisches Verfahren verwendet, das besonders glatte Flächen erzeugt und so die hohen optischen Güten der Microdisks sicherstellt. Eine Untersuchung an Microdisks ohne Luftloch mit unterschiedlichen Radien bietet die Gelegenheit, das theoretische Modell mit experimentellen Ergebnissen zu vergleichen. Weiterhin werden Microdisks mit Luftloch mit systematisch variierendem Lochabstand auf ihre räumliche Abstrahleingenschaft untersucht. In diesem Rahmen wird ein neues Verfahren zur Detektion der räumlichen Abstrahleigenschaft eingeführt, das die Untersuchung mit einem konfokalen Versuchsaufbau ohne Rotation der Probe oder des Detektors erlaubt. Mithilfe des theoretischen Modells und Simulationen werden die Moden aller Microdisks zugeordnet und auf ihre jeweilige räumliche Abstrahleigenschaft untersucht. Unsere Experimente legen eine unidirektionale Abstrahleigenschaft mit sehr hohen optischen Güten bei Microdisks mit Luftloch nahe.

Contents

1 Introduction **1**

2 Theory **5**
- 2.1 Fundamentals of the system . . . 5
- 2.2 The GaAs/vacuum interface . . . 6
- 2.3 Whispering-Gallery Modes . . . 9
  - 2.3.1 Modes in a coplanar waveguide . . . 9
  - 2.3.2 Ring contribution to the resonator modes . . . 13
  - 2.3.3 Theoretical quality factors . . . 19
- 2.4 Far-field emission characteristics . . . 21
  - 2.4.1 Ordinary microdisks . . . 21
  - 2.4.2 Pierced microdisks . . . 24

3 Experimental setup **27**
- 3.1 The micro-photoluminescence setup . . . 27
- 3.2 The macro-photoluminescence setup . . . 31

4 Preparation **35**
- 4.1 Vertical sample structure . . . 35
- 4.2 Sample fabrication . . . 36

5 Ordinary microdisks **41**
- 5.1 The sample . . . 41
- 5.2 Single microdisk spectra . . . 44
- 5.3 Microdisks of nominally the same size . . . 51
- 5.4 Microdisks with different sizes . . . 53

6 Pierced microdisks **57**
- 6.1 The sample design . . . 57
- 6.2 Mode allocation . . . 63
- 6.3 Influence of the hole position . . . 67
- 6.4 Spatial emission behavior . . . 74
  - 6.4.1 Emission image construction . . . 74
  - 6.4.2 Spatial emission comparison for different mode numbers . . . 79
- 6.5 Q factors and lasing . . . 85

7 Conclusion **91**

A Effective refractive index for resonant waveguide modes **95**

B Emission images of the a1aX experiment **99**

C Experimental data in the a1aX experiment **105**

References **113**

Acknowledgments **117**

List of Figures

1.1 Schematic illustration of a pierced microdisk 2

2.1 Rays of light in a microdisk 6
2.2 Refraction of light on a planar surface 7
2.3 Reflection coefficient and reflectivity of the $GaAs$-Air interface 8
2.4 Microdisk as a planar waveguide 10
2.5 Effective refractive index versus energy n_{eff} 12
2.6 Effective potential for a dielectric disk 15
2.7 Radial and planar field distribution in a microdisk. 18
2.8 Emission of a microdisk on a substrate 21
2.9 Angular far-field distribution of an isolated ordinary microdisk along the z-axis 22
2.10 Angular far-field distribution of a microdisk above a substrate 23
2.11 Spatial far-field emission of a microdisk on a substrate 23
2.12 Mode hybridization in pierced microdisks 25

3.1 Schematic micro-photoluminescence setup 28
3.2 Image construction in the micro-photoluminescence setup 30
3.3 Angular aperture of a microscope 32
3.4 Macro-photoluminescence setup 32
3.5 Detector quantum efficiencies 33

4.1 Wafer structure 36
4.2 Illustration of the microdisk fabrication process 38
4.3 Geometrical implications of the wet etching process 39

5.1 Photoluminescence of the unstructured sample A 42
5.2 Structure of sample A 44
5.3 Spectrum of a single microdisk 45
5.4 Calculation of whispering-gallery modes for varying radii 47
5.5 Comparison of a calculated and a measured spectrum 48
5.6 Mode allocation for a single microdisk 50
5.7 Calculated mode spacing 50
5.8 Spectra of microdisks with a nominally fixed radius 52
5.9 Shifted spectra of microdisks with nominally the same size. 52
5.10 Spectra of microdisks with increasing radius 54

5.11 Mode allocation for microdisks with increasing radius 55

6.1 Cross-section of a microdisk with its surrounding wall 58
6.2 SEM image of a pierced microdisk 59
6.3 Microscopic image of the sample with pierced microdisks 60
6.4 Pierced microdisk parameters 64
6.5 Whispering-gallery mode allocation for pierced microdisks 65
6.6 $Al_xGa_{1-x}As$ dispersion according to Pikhtin and Yas'kov 67
6.7 Calculated field distributions with varying mode numbers m and l 68
6.8 FDTD simulations of an experiment with varying parameter d 70
6.9 Spectra of the a1aX experiment 72
6.10 Comparison of experiment and FDTD simulations 73
6.11 Emission image of the microdisk a1a6 apart a whispering-gallery mode . 76
6.12 Emission images of the microdisk a1a6 on a whispering-gallery mode . . 78
6.13 Angular resolution of the setup 79
6.14 Profile plots for the a1aX experiment, $l = 1$ 80
6.15 Profile plots for the a1aX experiment, $l = 2$ 81
6.16 Profile plots for the a1aX experiment, $l = 3$ 82
6.17 Profile plots for the a1aX experiment, $l = 4$ 83
6.18 Excitation intensity dependent measurement 87
6.19 Mode variation with excitation power 88

B.1 Emission images of the a1aX experiment, $l = 1$ 100
B.2 Emission images of the a1aX experiment, $l = 2$ 101
B.3 Emission images of the a1aX experiment, $l = 3$ 102
B.4 Emission images of the a1aX experiment, $l = 4$ 103

1 Introduction

Light confinement to small volumes in optical microcavities today is a very active basic research field and has many applications. Research on this topic is quite broad and ranges from investigation of cavity characteristics with respect to light emission to research on new cavity quantum electrodynamical (CQED) effects. The applications base upon well understood mechanisms of the light emission of the microcavities and benefit from the very small dimensions of these systems.

Confinement to small volumes means that the dimensions of a cavity are of the same order as the wavelength of the trapped light. The fabrication of cavities of this size benefits from well known semiconductor preparation techniques. Wafer fabrication technology allows for the epitaxial growth of different semiconductor materials. Lateral structuring is usually realized by lithographic processes, due to their flexibility and ability to produce structures in the nanometer regime. The addition of optically active material like quantum wells or quantum dots gives the optical resonators the ability to act as lasers. With these fabrication techniques, optical microcavities can be produced with great versatility. Integrated optical circuits, a desirable goal for optical communication systems and networks, become feasible.

An optical microcavity can be realized in several different ways. A comprehensive overview of the different types of microresonators and their properties has been compiled in an article by Vahala [1]. One group are planar microresonators, which confine light in a Fabry-Perot resonator with the help of quarter-wavelength Bragg reflectors. Lasers with this kind of resonator emit light vertical to their layer structure and are thus called Vertical Cavity Surface Emitting Lasers (VCSEL). Another group of resonators base upon circular structures and enable the generation of so-called whispering-gallery modes. In these structures light is confined by total reflections at the boundary of the circularly shaped resonator. A third group uses two-dimensional photonic crystals to confine light. Here, periodically arranged holes in a semiconductor membrane induce an optical bandgap, analogous to the crystal lattice of semiconductors. In semiconductors, electrons can be confined at lattice defects. Similarly, intentionally leaving out a hole in the photonic crystal poses a tailored lattice ‘defect’ in which light can be confined.

In this work we present circularly shaped microcavities, the so-called microdisks. Microdisks were first introduced in 1992 by McCall et al. [2]. They consist of a circularly shaped semiconductor slab on a thin pedestal. Microdisk cavities can be fabricated with very high quality factors compared to Fabry-Perot cavities. The high quality factors are connected to the photon lifetime in a cavity and thus with the line-width of a resonant mode. The narrow line-widths of a whispering-gallery mode make microdisks a promising device for a lot of possible applications [3]. Among these applications is the ability of

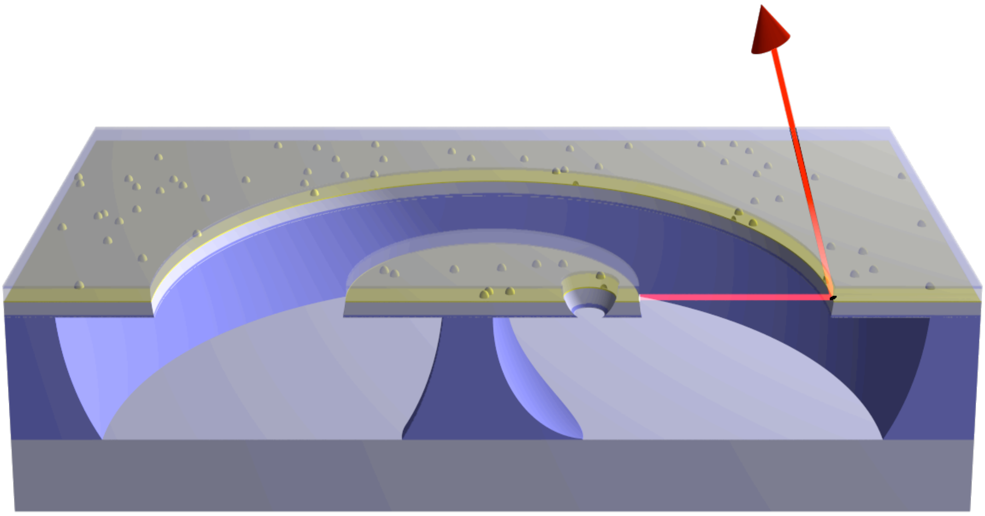

Figure 1.1: Schematic illustration of a pierced microdisk. The upper layer are translucent in order to show the buried quantum dots.

microdisks to act as optical filters or as laser light sources in integrated optical circuits. For such applications, it is desired that the whispering-gallery modes emit light. A usual circularly shaped microdisk generates whispering-gallery modes that emit uniformly in a narrow angle around the cavity plane. There is no single emission direction, as we find it in VCSELs. Unidirectional emission behavior in microdisks is nonetheless often desired. Several methods have been proposed to achieve unidirectional emission behavior in microdisks. In order to gain unidirectional emission from a microdisk, the rotational symmetry has to be broken. Three methods have been proposed so far: (i) a discontinuity in the boundary of a microdisk, (ii) a continuous shape deformation of a microdisk and (iii) a scattering center at a small distance from boundary of a microdisk. Discontinuities in the boundary as found in spirally shaped microdisks generally lead to good unidirectional emission results but are attended by the loss of high quality factors [4–6]. Alternatively, a continuous change in the shape of a microdisk preserves the high quality factors, but often produces multiple output beams [7–10]. In 2006 Wiersig and Hentschel [11] proposed in a theoretical work another way of producing high quality, unidirectional light emission from microdisks. An air hole, pierced near the boundary into a microdisk, should trigger the desired emission behavior. A cross-section of a pierced microdisk sketched in figure 1.1 illustrates the structure of the microdisks fabricated and investigated in the course of this work. In the center of the figure, a pierced microdisk on a pedestal can be seen. The microdisk is surrounded by a circularly shaped wall. The purpose of the wall is to scatter the emitted light in all directions. This way, a fraction of the light can be detected by a microscope objective looking on top of the microdisk. The wall and a certain measurement technique designed for our experimental setup enables the spatially and energetically resolved analysis of the whispering-gallery mode emission. The whispering-gallery modes are generated by the excitation of photoluminescence emission of buried $InAs$ quantum dots. The quantum dots are indicated as yellow bumps visible through the translucently drawn top layers. The influence of the air hole on a whispering-gallery mode depends on the mode number of the whispering-gallery mode, especially on the radial mode number l. Some whispering-gallery modes are almost unaffected by the hole maintaining their high quality factors. These modes emit uniformly into the cavity plane. Others scatter at the hole, emitting light in a single direction at the cost of a high quality factor. The latter case also induces an energetic shift of the whispering-gallery mode. This energetic shift opens the possibility for a set of two whispering-gallery modes to interact in case of a mode crossing. Near so-called avoided resonant crossings (ARCs), the two whispering-gallery modes switch their properties which may result in a high quality, unidirectional whispering-gallery mode. In figure 1.1, the unidirectional whispering-gallery mode emission behavior is indicated by a red arrow.

For unambiguous distinction we call microdisks without an airhole *ordinary microdisks*, whereas microdisks with an airhole will be called *pierced microdisks*.

This thesis describes the fabrication and experimental investigation of ordinary and pierced microdisks and their spatial emission behavior. The experimental investigation is supported by calculations based on a semi-analytical model, described in Chapter 2. This model allows for the calculation of the whispering-gallery mode energies and their field distributions in ordinary microdisks. In chapter 2 we also discuss the far-field emission behavior of ordinary microdisks.

Experimental investigations were carried out with a confocal photoluminescence setup. This setup is described in chapter 3 of the thesis. Spatially and energetically resolved emission images can be obtained in the setup by applying a certain measurement technique. The fundamentals of this measurement technique are also explained in this chapter.

We explain the details of the fabrication process in chapter 4. The preparation process of ordinary and pierced microdisks are basically the same. Nonetheless, the presence of the airhole has certain implications on the fabrication process. The limitations of the fabrication process due to the presence of the air hole will be explained at the end of chapter 4.

The spectroscopic results on ordinary microdisks are presented in chapter 5. Here, we compare in detail the results of experiments on microdisks with varying radii with calculations based on the model presented in chapter 2. On basis of this evaluation, we propose a new technique for whispering-gallery mode allocation.

Chapter 6 discusses the spectroscopic results on pierced microdisks. In the first section of this chapter our sample design is explained in detail. Here, we also analyze the fabrication process based on measurements in SEM images of series of microdisks. In the second section, we assign the mode numbers of the whispering-gallery modes observed in the experimentally obtained spectra with the help of the theoretical model introduced in chapter 2. The third section investigates the influence of the distance of the air hole to the boundary of a microdisk. We therefore calculated the field distribution with our theoretical model and used finite-difference time-domain (FDTD) simulations to calculate whispering-gallery mode spectra in dependence of the air hole distance. These results are compared to the experimentally obtained spectra of a series of microdisks with systematically increasing air hole distance. The fourth section analyzes the spatial emission behavior of pierced microdisks. In the fifth section we make some remarks about the quality factors of the measured whispering-gallery modes and investigate the lasing capability of pierced microdisks.

We conclude this thesis with a summary in chapter 7 and suggest possible further research on this topic.

2 Theory

This chapter deals with the theoretical background of the optical properties of microdisks. In the first section we will take a look at the optical properties of the $GaAs$/vacuum interface. In the second section, the principle of whispering-gallery modes will be introduced. Starting from Maxwell's equations, we present two theoretical models to calculate the mode energy and field distribution. This section concludes with some remarks on the influence of temperature on the whispering-gallery modes.

2.1 Fundamentals of the system

Before getting into the physical properties of microdisks, let us first consider the fundamental structure and working principle of a microdisk. A microdisk is basically a thin dielectric disk with a diameter of a few microns placed upon a pedestal, as depicted in Figure 2.1. The disk has a thickness of H, a radius R, a refractive index $n_{disk} > 1$ and is situated usually in air or vacuum[1] with $n_{vac} \approx 1$. Due to the rotational symmetry it stands to reason to describe microdisks in cylindrical coordinates (ρ, φ, z). The disk itself contains buried light emitters. When excited with monochromatic laser light, the emitters provide light inside the disk in the near infrared band. This light can either be transmitted outside the disk or reflected back into the disk due to the large difference of the refractive index at the boundary of the microdisk. The disk can thus act as a ring resonator. In a simplistic view we can explain the occurrence of resonances by a ray of light that travels around the circumference of the microdisk and interferes with itself after one roundtrip. Depending on the phase shift after one roundtrip, the light interferes constructively or destructively. The pedestal has almost no influence on the resonant light modes, since the light of high-Q modes is predominantly located near the disk's outer edge. The principle of waves skimming along the edge of a ring shape is known from the Whispering Gallery in the St. Paul's Cathedral in London, first investigated by Lord Rayleigh in 1910 [12]. Here, sound waves travel around the circular shaped dome of the cathedral, thus enabling a very efficient propagation of the sound waves along the wall of the dome. In reference to this phenomenon the resonances in a microdisk are called *whispering-gallery modes*.

Let us now take a closer look on the behavior of light at the boundary between the microdisk and its surrounding.

---

[1] In this work, all optical experiments on microdisks were performed in a low-pressure air environment with an air pressure in the order of $P_{air} \approx 1 \times 10^{-7}$ mbar. We consider and refer to this pressure as *vacuum* from now on.

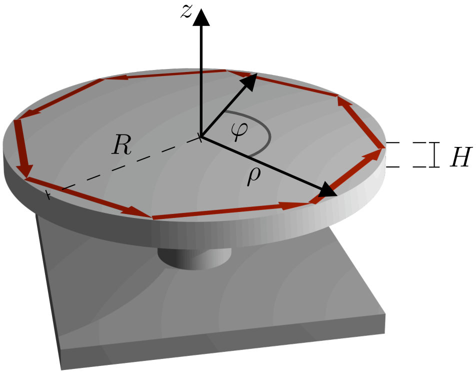

Figure 2.1: Microdisk in ray optics. Due to the rotational symmetry the system is best described in cylindrical coordinates (ρ, φ, z). The height of the microdisk is H, the radius R and the refractive index $n_{disk} > 1$ is large compared to the surrounding vacuum with $n_{vac} \approx 1$. The red arrows indicate constructively interfering waves propagating along the boundary of the microdisk.

2.2 The GaAs/vacuum interface

The ability of a semiconductor microdisk to act as a resonator is based on total reflection of light at its boundaries. Thus, consider a planar interface of two materials with different refractive indices n and n'. In classical optics, an incident ray of light can be either reflected or refracted. The reflection follows the law of reflection:

$$\theta_{incidence} = \theta_{reflected}, \qquad \text{(Law of reflection)}$$

whereas refraction is described by Snells's law:

$$n \sin\theta = n' \sin\theta'. \qquad \text{(Snell's law)}$$

For $n > n'$, the incidence angle θ can exceed a critical angle

$$\sin\theta_c := \frac{n'}{n}, \tag{2.1}$$

where incident light is no longer transmitted but is rather completely reflected. This effect is called total reflection.

Total reflection can also be explained in terms of wave optics. A ray of light can be described as a plane wave $e^{-i\mathbf{k}\cdot\mathbf{r}}$. In this case, an incident plane wave $\mathbf{k_i}$ is reflected into a plane wave $\mathbf{k_r}$ and transmitted into a plane wave $\mathbf{k_t}$ as illustrated in figure 2.2. Each pair of the vectors $\mathbf{k_i}$, $\mathbf{k_r}$ and $\mathbf{k_t}$ span the plane of incidence. The magnitude of the reflected and transmitted wave vectors is determined by $k_r = n\,\omega/c$ and $k_t = n'\,\omega/c$. The incident wave $\mathbf{k_i}$ can be composed with components parallel and perpendicular to

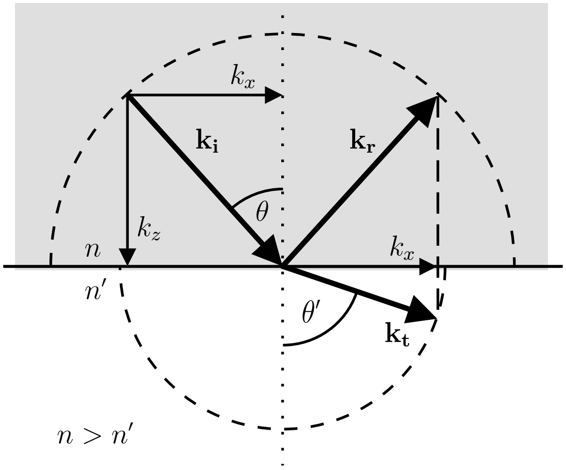

Figure 2.2: Refraction of light on a plane surface. In the depicted case, $n > n'$ holds. The angle of the refracted part of the light is thus larger than the angle of the reflected part. When θ approaches a certain critical angle θ_c, θ' approaches $\pi/2$. For incidence angles above θ_c, total reflection occurs.

the interface $\mathbf{k_i} = \mathbf{k_x} + \mathbf{k_z}$. Note that $\mathbf{k_x}$ is preserved for both the reflected and the transmitted fraction of the wave. The z component of the transmitted part of the wave is $\mathbf{k_t} \cdot \mathbf{e_z} = \sqrt{n'^2\,\omega^2/c^2 - k_x^2}$. If the incidence angle θ is larger than θ_c in the regime of total reflection, k_x is larger than $k_t = n'\,\omega/c$ and $\mathbf{k_t} \cdot \mathbf{e_z}$ has no real part and is purely imaginary. In this case the transmitted wave in z direction $e^{-i\mathbf{k_t}\cdot\mathbf{e_z}}$ is no longer transmitted into n'. Instead, an evanescent field leaks into the region with n' without energy transport in z direction. In contrast to classical ray optics, the wave picture yields information about the reflected and transmitted intensities with respect to the intensity of the incident plane wave. Consider an incident linearly polarized plane wave with a complex amplitude A and $|A| = 1$. The polarization of the incident wave is given in terms of the direction of the electric field with respect to the plane of incidence. The wave is called s-polarized, if the electric field is perpendicular to the plane of incidence, and p-polarized, if the electric field is parallel to the plane of incidence. In section 2.3, we will discuss the microdisk acting as a coplanar waveguide. In the waveguide terminology, a mode is transverse electric (TE) polarized, if the electric field is perpendicular to both the plane of incidence and the propagation direction, which relates to the s-polarization. If the magnetic field is perpendicular to both the plane of incidence and the propagation direction, i.e. the wave is p-polarized, a mode is transverse magnetic (TM) polarized. We will henceforth use the waveguide notation for the polarization states. Applying Maxwell's equation (see

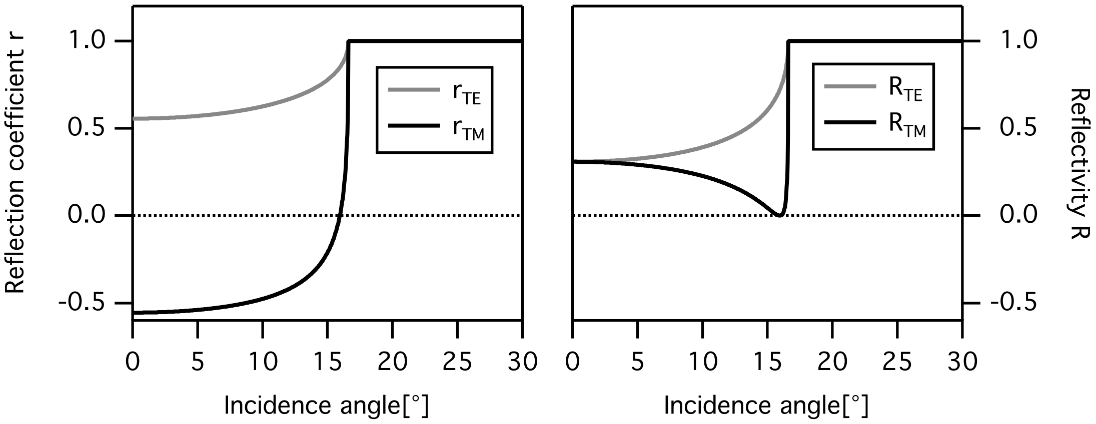

Figure 2.3: Reflection coefficient r and reflectivity R for of the $GaAs$-Air interface calculated with the Fresnel Formulae. At $\theta \approx 16.6°$ total reflection occurs.

e.g. Born and Wolf [13]) yields for the reflection coefficients r_{TE} and r_{TM}:

$$r_{TE} = \frac{n\cos\theta - n'\cos\theta'}{n\cos\theta + n'\cos\theta'} \tag{2.2a}$$

$$r_{TM} = \frac{n'\cos\theta - n\cos\theta'}{n'\cos\theta + n\cos\theta'}. \tag{2.2b}$$

These are the well known Fresnel formulae. Since

$$k_z = k\cos\theta = n\frac{\omega}{c_0}\cos\theta \tag{2.3}$$

$$k'_z = k'\cos\theta' = n'\frac{\omega}{c_0}\cos\theta', \tag{2.4}$$

we can write the Fresnel Formulae in a more convenient form

$$r_{TE} = \frac{k_z - k'_z}{k_z + k'_z} \tag{2.5a}$$

$$r_{TM} = \frac{n'^2 k_z - n^2 k'_z}{n'^2 k_z + n^2 k'_z}. \tag{2.5b}$$

with the corresponding reflected intensities R_{TE} and R_{TM}:

$$R_{TE} = |r_{TE}|^2 \tag{2.6a}$$

$$R_{TM} = |r_{TM}|^2. \tag{2.6b}$$

Note that we substituted wave vector of the transmitted wave $\mathbf{k_t}$ with $\mathbf{k}'$ in this calculation in order to consistently distinguish all variables as inside or outside the microdisk. We will stick with this notation from now on.

Figure 2.3 shows the reflection coefficient r and the reflectivity R for a $GaAs$/vacuum surface. In this figure, the refractive index of $GaAs$ is assumed to be $n(GaAs) = 3.5$

and the refractive index of vacuum is $n'(vacuum) = 1$. Usually, the refractive index of a material is dispersive $n(\omega)$. Since that does not affect further calculations we use the notation n for simplicity instead of the notation $n(\omega)$.

The critical angle for the $GaAs$/vacuum interface is $\theta_c \approx 16.6°$. At the so-called Brewster angle the reflected light is completely TE polarized (perpendicular to the plane of incidence). For the refractive indices $n(GaAs)$ and $n'(vacuum)$ this is the case at $\theta_B = 16.0°$.

2.3 Whispering-Gallery Modes

We now want to calculate the energetic position of whispering-gallery modes and the corresponding field distributions in a given microdisk. It is possible to solve Maxwell's equation with appropriate boundary conditions for a two-dimensional microdisk. In order to calculate the resonances of a three-dimensional microdisk, we treat the microdisk with a certain height H as a coplanar resonator in z direction. We introduce a new quantity n_{eff} analogous to an approach proposed by Slusher et al. [14] which represents the coplanar resonator properties of a microdisk. This way we basically separate the microdisk into a coplanar resonator and a two-dimensional ring resonator. The new quantity n_{eff} can be incorporated into the calculation of the ring resonator which then yields solutions for a quasi-three dimensional model of the microdisk modes.

2.3.1 Modes in a coplanar waveguide

In this section, we investigate resonance properties of a microdisk in z direction. The microdisk slab can be interpreted as a coplanar resonator. Figure 2.4 (a) depicts the microdisk slab and illustrates two opposing electromagnetic waves, which are reflected at the top and bottom boundary of the slab. Usually, the wave motion in a cylindrically shaped system like the microdisk is expressed in cylindrical coordinates with the wave vectors $\mathbf{k}_\rho$, $\mathbf{k}_\varphi$ and $\mathbf{k_z}$. Since we are now only interested in the resonances in z direction, we use cartesian coordinates and treat the microdisk as a waveguide of infinite x and y dimension and a limited height H as illustrated in figure 2.4 (b). Assuming $\mathbf{k_y} = 0$, the total $\mathbf{k}$ vector of a propagating wave front in a whispering-gallery mode is composed of $\mathbf{k} = \mathbf{k_x} + \mathbf{k_z}$. A propagating wave front is composed of two waves with equal $\mathbf{k_x}$, and opposed $\mathbf{k_z}$ wave vectors. These two waves advance in a zigzag movement with a velocity c_0/n in $\mathbf{k}$ direction, where c_0 is the speed of light in vacuum and n is the refractive index of the microdisk's material.

The resonance conditions for coplanar resonators are well known [13]. They are dependent on the reflection coefficient of the resonator, its thickness, the wavelength and the incidence angle of the wave. The wavelength and incidence angle can be expressed through k_z. For a given complex reflection coefficient r we find the following resonance condition:

$$1 - r^2\, e^{i2Hk_z} = 0. \tag{2.7}$$

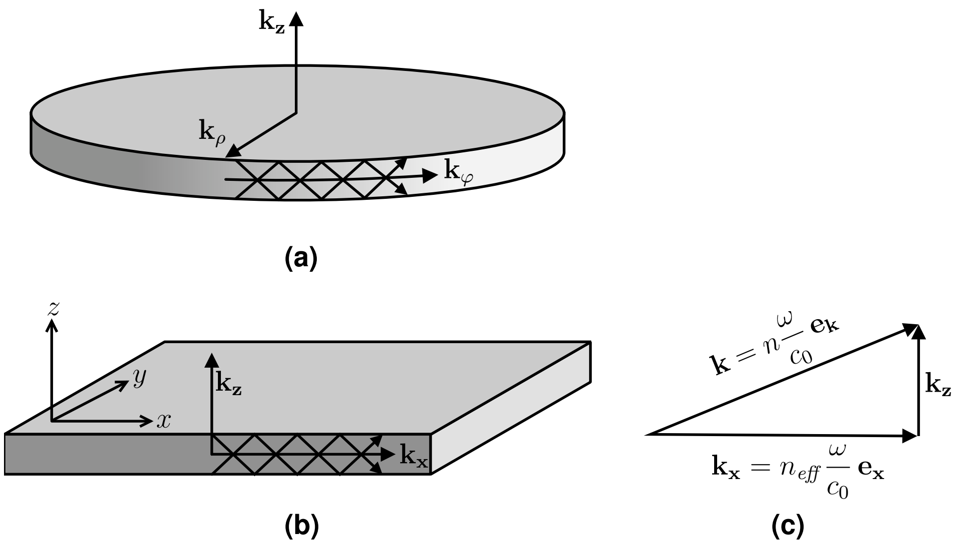

Figure 2.4: Microdisk as a planar waveguide. (a) A whispering-gallery mode is composed of two waves with equal $\mathbf{k}_\varphi$ and opposed $\mathbf{k_z}$. (b) The calculation is simplified by looking at an infinitely stretched slab, using in cartesian coordinates. The goal is to express the resonances in terms of an expression for the wave front motion in $\mathbf{k_x}$ direction only. This new quantity is the effective refractive index n_{eff} (c).

We define a vertical mode number p for each k_z that solves equation 2.7. The mode number $p-1$ then gives the number of nodes in z direction. Thus, odd p describe a symmetric field distribution in z direction and even p an anti-symmetric field distribution in z direction. We can obtain the reflectivity r for TE and TM polarization by applying the Fresnel Formulae (2.2b) and (2.2a). For incidence angles below θ_c, $\Re(r) < 1$ and $\Re(k_z) \neq 0$ hold and transmission of refracted light occurs. We call these modes *leaky* modes, since the waves transmit to the outside of the resonator. For incidence angles larger than θ_c, $\Re(r) = 1$ and $\Re(k_z) = 0$ hold and the waves are confined due to total reflection. These are the *guided* modes. In this regime, a wave front composed of the two opposed waves travels along the x direction. Our goal is to describe this wave motion of resonant waves in x direction. We therefore introduce an *effective refractive index* n_{eff}, which describes a wave with the wave vector $\mathbf{k_x}$ in the waveguide. As shown in Figure 2.4 (c) $\mathbf{k_x}$ can be written as

$$\mathbf{k_x}^2 = \mathbf{k}^2 - \mathbf{k_z}^2, \tag{2.8}$$

or, since $\mathbf{k}^2 = |\mathbf{k}|^2 = k^2$, we can write:

$$\begin{aligned} n^2 k'^2_x &= n^2 k'^2 - n^2 {k'_z}^2 \\ n^2 k'^2_x &= n^2 k'^2 \left(1 - \frac{{k'_z}^2}{k'^2}\right). \end{aligned} \tag{2.9}$$

We now introduce the effective refractive index as

$$n_{\mathit{eff}}^2(k') := n^2\left(1-\frac{{k'_z}^2}{k'^2}\right). \tag{2.10}$$

We can see from this equation that the effective refractive index n_{eff} is composed of the refractive index of the microdisk's material and the ratio of k'_z to k'. We can now write equation (2.9) as follows:

$$n^2 {k'}_x^2 = n_{\mathit{eff}}^2(k')\, k'^2. \tag{2.11}$$

An electromagnetic wave in x direction can therefore be written as

$$\mathbf{A}(\mathbf{x},t) = A_0\, e^{n_{\mathit{eff}}(k')\mathbf{k}'\cdot\mathbf{x}\pm i\omega t}, \tag{2.12}$$

where $\mathbf{A}$ stands for either the electric field $\mathbf{E}$ or the magnetic field $\mathbf{B}$. Note that this expression contains no explicit dependence on z. The z dependence is contained in the expression n_{eff}.

We now want to find an expression for only the resonant waveguide modes in dependence of the effective refractive index n_{eff}. From equation (2.10) we may write

$$k'_z = \frac{k'}{n}\sqrt{n^2-n_{\mathit{eff}}^2} = \frac{n'}{n}\frac{\omega}{c_0}\sqrt{n^2-n_{\mathit{eff}}^2}, \tag{2.13}$$

We apply the Fresnel formulae (2.5) and equation (2.13) to the resonance condition in equation (2.7). Depending on the polarization of the incident wave, we have to solve the following equations:

$$e^{-i2Hk_z} = r_{TE}^2 = \left(\frac{k_z-k'_z}{k_z+k'_z}\right)^2 \tag{2.14a}$$

$$e^{-i2Hk_z} = r_{TM}^2 = \left(\frac{k_z-n^2k'_z}{k_z+n^2k'_z}\right)^2. \tag{2.14b}$$

By applying n_{eff} to these equations, k_z and k'_z can be eliminated. The detailed derivation is shown in appendix A. Due to the quadratic terms in equations (2.14), we obtain two transcendent equations for each polarization

$$\text{TE symmetric:}\qquad \tan\left(\frac{H\omega}{2c_0}\sqrt{n^2-n_{\mathit{eff}}^2}\right) = \sqrt{\frac{n_{\mathit{eff}}^2-1}{n^2-n_{\mathit{eff}}^2}} \tag{2.15a}$$

$$\text{TE antisymmetric:}\qquad \cot\left(\frac{H\omega}{2c_0}\sqrt{n^2-n_{\mathit{eff}}^2}\right) = -\sqrt{\frac{n_{\mathit{eff}}^2-1}{n^2-n_{\mathit{eff}}^2}} \tag{2.15b}$$

$$\text{TM symmetric:}\qquad \tan\left(\frac{H\omega}{2c_0}\sqrt{n^2-n_{\mathit{eff}}^2}\right) = n^2\sqrt{\frac{n_{\mathit{eff}}^2-1}{n^2-n_{\mathit{eff}}^2}} \tag{2.15c}$$

$$\text{TM antisymmetric:}\qquad \cot\left(\frac{H\omega}{2c_0}\sqrt{n^2-n_{\mathit{eff}}^2}\right) = -n^2\sqrt{\frac{n_{\mathit{eff}}^2-1}{n^2-n_{\mathit{eff}}^2}}. \tag{2.15d}$$

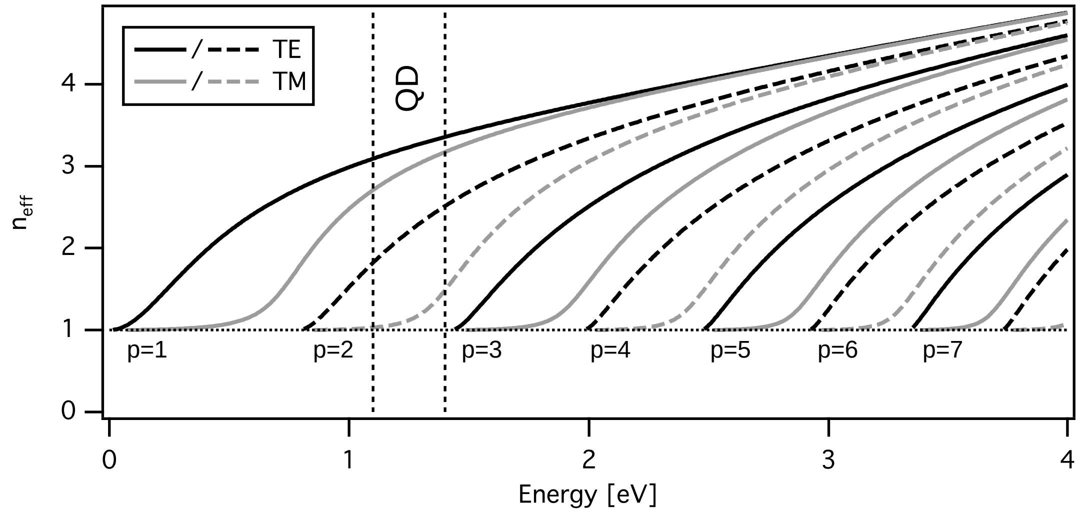

Figure 2.5: Effective refractive index for a coplanar resonator with a height $H = 250\,\text{nm}$. The color indicates the polarization of the incident wave (black: TE, gray: TM). Solid lines belong to the symmetric, dashed lines to the antisymmetric solution of equation 2.15. The emission range of the quantum dots used in the experiments for mode excitation is indicated by the vertical dashed lines.

The two equations for each polarization yield the solutions for the resonant symmetric and antisymmetric modes of the waveguide. Due to their transcendent nature, equations (2.15) have to be solved numerically. Figure 2.5 shows n_{eff} for the resonances of a coplanar *GaAs* resonator with a thickness of $H = 250\,\text{nm}$. The polarization of the incident wave is color coded: black curves show n_{eff} for resonant modes in TE polarization, gray curves the TM polarization. Symmetric and antisymmetric solutions are illustrated by solid (symmetric) and dashed (antisymmetric) lines. The displayed energetic range by far exceeds the energetic range of the modes that we are able to excite in an experiment. The observable energetic range is limited by the emission range of the quantum dots inside the microdisks. In figure 2.5, the emission range of the quantum dots is indicated by two vertical dashed lines. Thus, in our experiments the symmetric and antisymmetric vertical modes $p = 1$ and $p = 2$ in both polarizations are the only ones that can be excited. The calculations shown here take the dispersion of the refractive index n into account. We used a linear adaptation of the dispersion measured by A. N. Pikhtin and A. D. Yas'kov [15]:

$$n(E) = 3.46 + \frac{E(\text{eV}) - 1.1}{2}. \tag{2.16}$$

The effective refractive index n_{eff} starts for each branch at $n_{\mathit{eff}} = 1$ and approaches $n(E)$ at higher energies. For each mode number p, the TM modes have a lower n_{eff} at the same energy compared to the TE modes.

2.3.2 Ring contribution to the resonator modes

So far, we have calculated the resonant modes of a coplanar resonator. By introducing an effective refractive index n_{eff} which implicitly takes the z dependence into account, we can express the wave motion for resonant modes in x direction. Now, we want to find the resonant modes for a circularly shaped boundary, the so-called whispering-gallery modes. We therefore make a new ansatz in two dimensions and use n_{eff} to describe the wave motion in the plane. The rotational symmetry of the problem suggests the use of cylindrical coordinates. With the introduction of two new mode numbers, an azimuthal mode number m and a radial mode number n, the modes of a closed circular resonator can be expressed by Bessel functions. This description yields the solution for the energetic mode positions and the electric and magnetic field distributions inside the resonator. In order to obtain information about the fields outside the resonator we take a slightly different approach which also allows for the determination of quality factors due to tunneling processes.

The approach is analogous to the one described by M. Hentschel [16]. First we will derive an expression for the electric field, which leads to equations similar to quantum mechanical potential problems. In this analogy, the boundaries of a microdisk can be described as a potential barrier.

We assume a harmonic time dependence $e^{-i\omega t}$ with the vacuum dispersion relation $\omega_0 = k_0 c_0$. We look for a solution of Maxwell's equations, which read in SI units

$$\nabla \times \mathbf{E} + \dot{\mathbf{B}} = 0 \tag{2.17a}$$
$$\nabla \times \mathbf{H} - \dot{\mathbf{D}} = \mathbf{j}. \tag{2.17b}$$

In the absence of an electric current $\mathbf{j} = 0$, and with $\mathbf{D} = \epsilon\mathbf{E}$ and $\mathbf{B} = \mu\mathbf{H}$, we can write the derivatives $\dot{\mathbf{B}}$ and $\dot{\mathbf{D}}$ for the harmonic time dependence $e^{-i\omega t}$ as

$$\nabla \times \mathbf{E} = ik\mu\mathbf{H} \tag{2.18a}$$
$$\nabla \times \mathbf{H} = -ik\epsilon\mathbf{E}. \tag{2.18b}$$

To obtain equations with $\mathbf{E}$ and $\mathbf{H}$ only, we apply equation (2.18a) to equation (2.18b) and vice versa. With $n = \sqrt{\epsilon\mu}$ we derive

$$\nabla \times \nabla \times \mathbf{E} = n^2k^2\mathbf{E} \tag{2.19a}$$
$$\nabla \times \nabla \times \mathbf{H} = n^2k^2\mathbf{H}. \tag{2.19b}$$

In a dielectric, charge densities can only appear on its surface. Thus, no sources of the electro-static field exist in each domain with constant $n(\mathbf{r})$, which means that in these regions Gauss's law for the electric field simplifies to $\nabla \cdot \mathbf{E} = 0$. Gauss's law for the magnetic field states $\nabla \cdot \mathbf{B} = 0$. Now, we can rewrite equations (2.19) with the help of the rule $\nabla \times \nabla \times \mathbf{A} = \nabla(\nabla \cdot \mathbf{A}) - \nabla^2\mathbf{A}$ as

$$-\nabla^2\mathbf{E} = n^2k^2\mathbf{E} \tag{2.20a}$$
$$-\nabla^2\mathbf{B} = n^2k^2\mathbf{B}. \tag{2.20b}$$

These wave equations can easily be written in a form similar to the Schrödinger equation:

$$-\nabla^2\mathbf{E} + k^2(1-n^2)\mathbf{E} = k^2\mathbf{E} \tag{2.21a}$$

$$-\nabla^2\mathbf{B} + k^2(1-n^2)\mathbf{B} = k^2\mathbf{B}. \tag{2.21b}$$

One important difference to the quantum mechanical Schrödinger equation is that $\mathbf{E}$ or $\mathbf{B}$ are vector fields instead of scalar wave functions. This implies a polarization dependence of the boundary conditions. Analogous to the Schrödinger equation, an energy eigenvalue k^2 appears on the right-hand side of the equations 2.21. Furthermore, the term $k^2(1-n^2)$ appears in the equations (2.21) correlating to the potential term in Schrödinger equation. Different to most potentials in quantum mechanics, this quasi-potential is dependent on the eigenvalue k^2 and thus makes the potential itself energy dependent.

We can solve equations (2.21) component-wise ($i = \rho, \varphi, z$) by using a variable-separation ansatz. We assume an angular dependence $e^{im\varphi}$ and a z dependence $e^{ik_z z}$ and write the following separation ansatz

$$E_i(\mathbf{r}) = E_i(\rho)e^{im\varphi}e^{ik_z z} \tag{2.22a}$$

$$B_i(\mathbf{r}) = B_i(\rho)e^{im\varphi}e^{ik_z z}. \tag{2.22b}$$

Applying the ansatz (2.22) to the equations (2.21) we obtain after some straightforward calculations the radial equations

$$-\left(\frac{\partial}{\partial\rho^2} + \frac{1}{\rho}\frac{\partial}{\partial\rho}\right)E_i(\rho) + V_{\mathit{eff}}E_i(\rho) = k^2E_i(\rho) \tag{2.23a}$$

$$-\left(\frac{\partial}{\partial\rho^2} + \frac{1}{\rho}\frac{\partial}{\partial\rho}\right)B_i(\rho) + V_{\mathit{eff}}B_i(\rho) = k^2B_i(\rho), \tag{2.23b}$$

where we used with the Laplace operator in cylindrical coordinates:

$$\nabla^2 = \frac{1}{\rho}\frac{\partial}{\partial\rho}\left(\rho\frac{\partial}{\partial\rho}\right) + \frac{1}{\rho^2}\frac{\partial^2}{\partial\varphi^2} + \frac{\partial^2}{\partial z^2}, \tag{2.24}$$

and introduced the effective potential

$$V_{\mathit{eff}} := \frac{m^2}{\rho^2} + k^2\left(1 - n^2(\rho)\right) + k_z^2. \tag{2.25}$$

Compared to the equations (2.21), the effective potential in equation (2.25) has two additional terms. The term m^2/ρ^2 can be seen as the centrifugal potential, which is due to the conservation of the z component of the angular momentum in a rotational invariant system characterized by the quantum number m. The term $k^2\left(1 - n(\rho)^2\right)$ constitutes a potential barrier at the boundary for a system with $n > 1$, with an attractive well inside the material. The third term k_z^2 expresses the conservation of liner momentum in z direction and acts as an offset in energy. In the two dimensional microdisk we consider

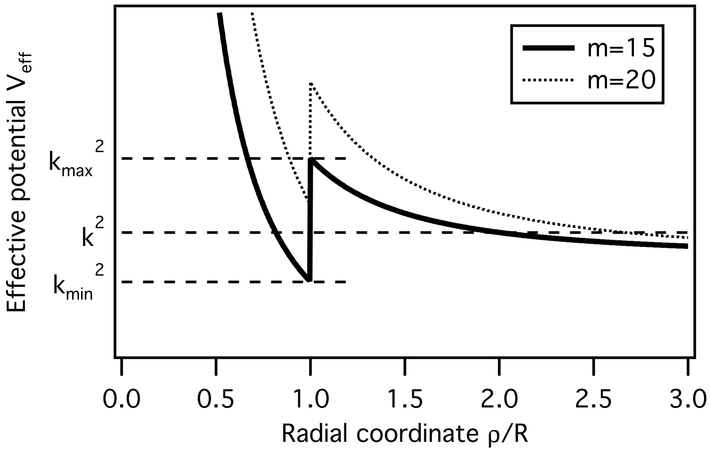

Figure 2.6: Effective potential for a dielectric disk. The shape of the effective potential suggests an interpretation analogous to the quantum mechanical well. Bound states are expected between k^2_{min} and k^2_{max}, broadened by the tunneling probability. The effective potential is energy dependent: The solid curve illustrates the potential for $m = 15$ and the dotted curve for $m = 20$.

k_z^2 to be zero. Nonetheless, the microdisk has a considerable height, which must not be neglected. This is where the effective refractive index n_{eff} comes into play. The k_z dependence is expressed in n_{eff} as shown in equation (2.10). We numerically calculate the solutions for the TM and TE polarization and substitute k_z^2 with the effective refractive index in equation (2.25) as follows:

$$V_{\mathit{eff}} := \frac{m^2}{\rho^2} + k^2\left(1 - n^2(\rho)\right), \qquad \text{with} \qquad n(\rho) = \begin{cases} n_{\mathit{eff}}(k) & \text{if} \quad \rho < R \\ n' & \text{if} \quad \rho > R \end{cases}. \tag{2.26}$$

Figure 2.6 shows the effective potential V_{eff} versus ρ/R schematically, where R is the radius of a microdisk as depicted in figure 2.1. The overall effective potential is determined by the centrifugal term m^2/ρ^2. For ρ approaching R from infinity m^2/ρ^2 acts as a repulsive barrier. At $\rho = R$ the discontinuity of the refractive index causes a jump in the potential, leading to a potential well inside the microdisk. The absolute energy difference at $\rho = R$ is energy dependent and can be calculated to [16]

$$k_{min} = \frac{m}{nR} \qquad \text{and} \qquad k_{max} = \frac{m}{R}. \tag{2.27}$$

The shape of the effective potential suggests an interpretation analogous to the problem of the quantum mechanical well. Thus, we expect to observe a discrete bound state for each angular momentum m in the energy region

$$\frac{m}{nR} \le k \le \frac{m}{R} \tag{2.28}$$

broadened by the tunneling probability through the barrier.

Eigenvalues of the open microdisk

Now, we want to solve the equations (2.23). Formally, equations (2.23) can be transformed into Bessel differential equations and can thus be solved by linear combinations of the Bessel functions of the first kind $J_m(nkr)$ and of the second kind $Y_m(nkr)$, with $n = n(r)$. The Bessel functions on their own define a standing wave along the radial axis. Complex linear combination of the orthogonal Bessel functions yields the solution for an incoming and an outgoing wave. These functions are called Hankel functions of the first and second kind

$$H_m^{(1)}(nk\rho) = J_m(nk\rho) + i\,Y_m(nk\rho) \qquad \text{outgeigeoing} \tag{2.29}$$

$$H_m^{(2)}(nk\rho) = J_m(nk\rho) - i\,Y_m(nk\rho) \qquad \text{incoming.} \tag{2.30}$$

This way, we interpret the complex linear combination of the Bessel functions similarly as the orthogonal sine and cosine functions in plane waves with $e^{\pm ik\rho} = \cos(k\rho) \pm i\,\sin(k\rho)$.

Bessel functions of the second kind diverge for $\rho \to 0$. The absence of free charge carriers in the microdisk on the other hand demands a finite solution for the fields at $\rho = 0$. Thus, inside the microdisk only Bessel functions of the first kind can contribute to the solution resulting in the following ansatz:

$$F(\mathbf{r}) = \begin{cases} A_m J_m(n_{\mathit{eff}} k\rho) & \text{if} \quad \rho < R \\ B_m H_m^{(1)}(n' k\rho) & \text{if} \quad \rho > R \end{cases}, \tag{2.31}$$

where $F(\mathbf{r})$ stands for either $E(\mathbf{r})$ or $B(\mathbf{r})$. Without loss of generality, we can set $B_m = 1$ in equation (2.31).

We can now solve the eigenvalue problem with the help of the matching conditions at the dielectric boundary for Maxwell's equations:

- The tangential components of the electric field $\mathbf{E}$ and the magnetic field $\mathbf{B}$ have to be continuous at the interface boundaries.
- The normal components of the dielectric displacement $\mathbf{D}$ and the magnetic induction $\mathbf{H}$ have to be continuous at the interface boundaries.

Since we treat the microdisk through the effective refractive index n_{eff} as a quasi two dimensional system, we mean by boundary the outer, circular shaped side walls of the interface. We use the following boundary conditions for further calculation: For the TM polarization there is no z component of the magnetic field $H_z = 0$. The electric field has a z component $E_z \neq 0$ which is parallel to the boundary. Furthermore, the electric and magnetic fields are related via Maxwell's equations (2.18). Especially, equation (2.18a) yields that H_φ is proportional to the radial derivative of E_z. This leads us to the boundary conditions for the TM polarization:

$$E_z(R_<) = E_z(R_>) \tag{2.32}$$

$$\frac{\partial}{\partial\rho} E_z(R_<) = \frac{\partial}{\partial\rho} E_z(R_>). \tag{2.33}$$

Equally for the TE polarization no z component of the electric field exists, i.e. $E_z = 0$. Now, the magnetic field has a persistent z component parallel to the boundary. This time, equation (2.18b) relates the radial derivative of H_z with $n^2 E_{\varphi,\rho<}$ and $n'^2 E_{\varphi,\rho>}$. The boundary conditions for TE polarization read:

$$H_z(R_<) = H_z(R_>) \tag{2.34}$$

$$n'^2 \frac{\partial}{\partial \rho} H_z(R_<) = n^2 \frac{\partial}{\partial \rho} H_z(R_>). \tag{2.35}$$

Applying the boundary conditions to the ansatz (2.31) yields:

$$A_m J_m(n_{\mathit{eff}} kR) = B_m H_m^{(1)}(n' kR) \tag{2.36a}$$

$$A_m \frac{\partial}{\partial \rho} J_m(n_{\mathit{eff}} kR) = B_m \frac{\partial}{\partial \rho} H_m^{(1)}(n' kR) \qquad \text{for TM polarization} \tag{2.36b}$$

$$A_m J_m(n_{\mathit{eff}} kR) = B_m H_m^{(1)}(n' kR) \tag{2.36c}$$

$$n'^2 A_m \frac{\partial}{\partial \rho} J_m(n_{\mathit{eff}} kR) = n^2 B_m \frac{\partial}{\partial \rho} H_m^{(1)}(n' kR) \qquad \text{for TE polarization.} \tag{2.36d}$$

Due to the linear nature of systems, we can treat the problem as an eigenvalue problem and rewrite the system of equations in the form:

$$\mathcal{M} \cdot \begin{pmatrix} A_m \\ B_m \end{pmatrix} = 0, \tag{2.37}$$

where $\mathcal{M}$ is a (2×2) matrix with k dependent functions. The solution of this homogeneous vector equation is trivial $(A_m = 0, B_m = 0)$ for linearly independent column vectors of $\mathcal{M}$. We obtain nontrivial solutions for linearly dependent column vectors of $\mathcal{M}$, i.e. if the determinant of $\mathcal{M}$ vanishes:

$$\begin{vmatrix} J_m(n_{\mathit{eff}} kR) & -H_m^{(1)}(n' kR) \\ \frac{\partial}{\partial \rho} J_m(n_{\mathit{eff}} kR) & -\frac{\partial}{\partial \rho} H_m^{(1)}(n' kR) \end{vmatrix} = 0 \qquad \text{for TM polarization} \tag{2.38a}$$

$$\begin{vmatrix} J_m(n_{\mathit{eff}} kR) & -H_m^{(1)}(n' kR) \\ n'^2 \frac{\partial}{\partial \rho} J_m(n_{\mathit{eff}} kR) & -n^2 \frac{\partial}{\partial \rho} H_m^{(1)}(n' kR) \end{vmatrix} = 0 \qquad \text{for TE polarization.} \tag{2.38b}$$

We thus have to determine the complex k for which the determinant (2.38a) or (2.38b) vanishes to find the eigenmodes of the microdisk. The resonant k values are determined numerically. Once a resonant k is found, we can easily determine A_m and B_m and calculate the field distribution in the microdisk. This is demonstrated in figure 2.7 for a microdisk with a 2.5 µm radius and a thickness of 250 nm. The plot shows the calculation for two different azimuthal mode numbers $m = 18$ and $m = 40$ in each case for the radial mode numbers $l = 1$, $l = 2$ and $l = 3$. The corresponding energies obtained from to the real part of the wave vectors k for these whispering-gallery modes are listed in table 2.1. Figure 2.7 shows the radial field distributions for each whispering-gallery

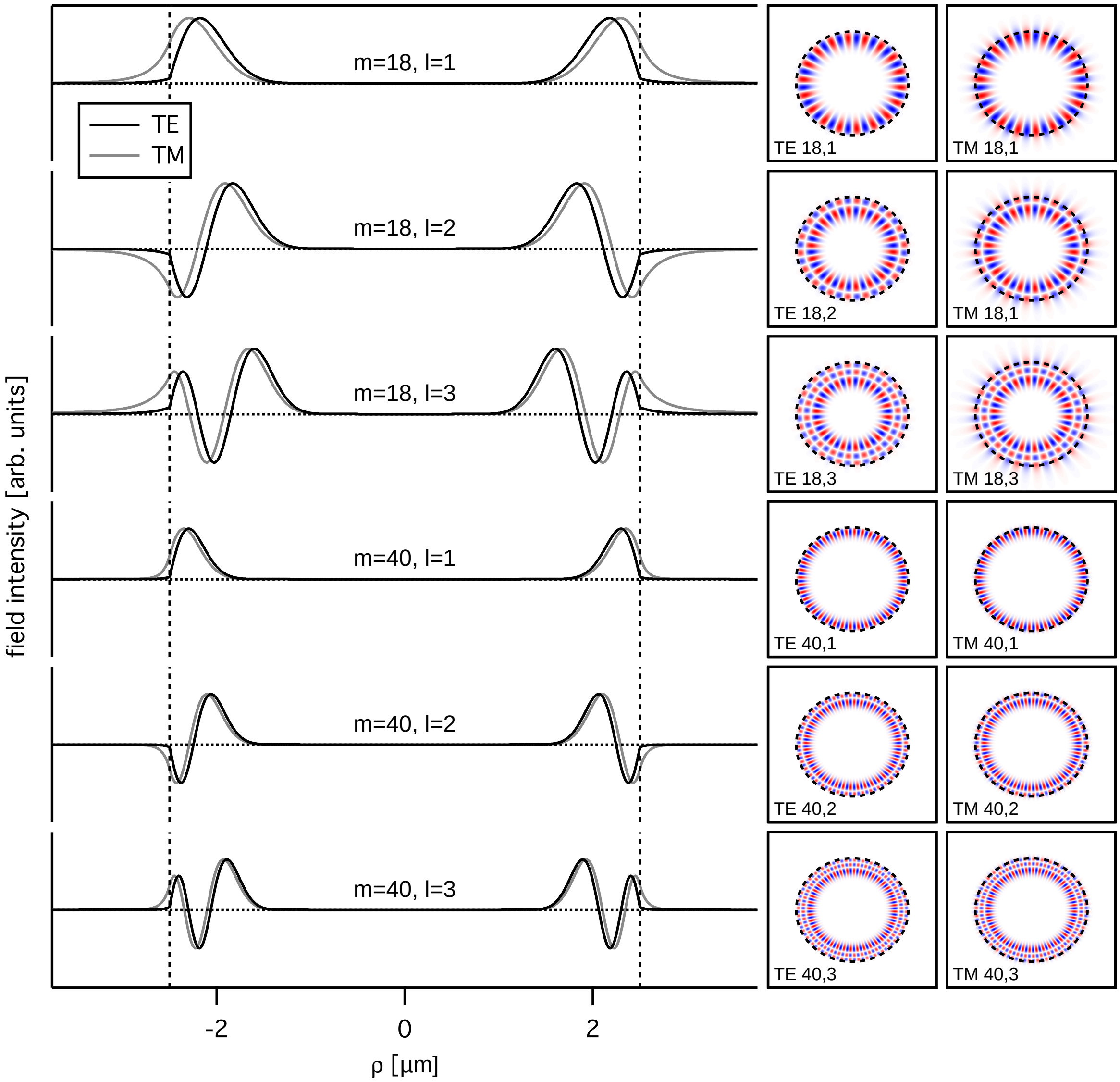

Figure 2.7: Radial and planar field distributions for a microdisk with a radius of $R = 2.5\,\mu m$ and 250 nm thickness. According to the conventions given in equation 2.32 and 2.34, the TM case depicts the electric field distribution and the TE case the magnetic field distribution. The field distributions with the azimuthal mode numbers $m = 18$ and $m = 40$ are shown in each case for the radial mode numbers $l = 1$, $l = 2$ and $l = 3$. The microdisk's boundary is indicated by a dashed line in each plot. We can observe two trends in these plots: with rising azimuthal mode numbers the field intensity shifts towards the boundary of the microdisk and with rising radial mode numbers the field intensity shifts towards the center of the microdisk.

m	pol.	l	energy
$m = 18$	TE	$l = 1$	$E = 0.703\,\mathrm{eV}$
		$l = 2$	$E = 0.795\,\mathrm{eV}$
		$l = 3$	$E = 0.874\,\mathrm{eV}$
	TM	$l = 1$	$E = 0.855\,\mathrm{eV}$
		$l = 2$	$E = 0.922\,\mathrm{eV}$
		$l = 3$	$E = 0.982\,\mathrm{eV}$
$m = 40$	TE	$l = 1$	$E = 1.165\,\mathrm{eV}$
		$l = 2$	$E = 1.263\,\mathrm{eV}$
		$l = 3$	$E = 1.347\,\mathrm{eV}$
	TM	$l = 1$	$E = 1.225\,\mathrm{eV}$
		$l = 2$	$E = 1.312\,\mathrm{eV}$
		$l = 3$	$E = 1.387\,\mathrm{eV}$

Table 2.1: Numerical values for the energetic position of the whispering-gallery mode shown in figure 2.7.

mode. The corresponding planar field distribution in both polarizations is plotted on the right side next to the plots. In each plot dashed lines illustrate the boundary of the microdisk. In these plots we can see two important general trends of whispering-gallery modes with respect to the spatial field distribution. First, we note that for higher radial mode numbers l the field radially advances closer towards the center of the microdisk. This can be observed for each mode number individually. Second, for higher azimuthal mode numbers m the field concentrates more at the boundary of a microdisk. This can be best observed in the planar plots in figure 2.7.

In figure 2.7 we have only considered the whispering-gallery modes for the vertical mode number $p = 1$. In the energetic range of the quantum-dot photoluminescence-emission we can theoretically observe whispering-gallery modes with $p = 2$ as well. Whispering-gallery modes with $p = 2$ in the observable energy range have quite low azimuthal mode numbers.

2.3.3 Theoretical quality factors

The complex k values for a whispering-gallery mode found by solving equation (2.38) yield besides the real part an imaginary part which allows for determination of the theoretical loss. In the previous section we assumed a harmonic time dependence $e^{-i\omega t}$ with real angular frequency ω for the electric and magnetic field. The found k vectors of the resonant modes on the other hand are complex. The complex k vector $k = k_{re} + i\,k_{im}$ can be converted to a complex angular frequency via the dispersion relation $\omega = ck$ to:

$$\omega_0 + i\,\Gamma = ck_{re} + i\,ck_{im}, \qquad \text{where} \qquad \omega_0 := ck_{re}, \quad \Gamma := ck_{im} \tag{2.39}$$

In this notation, the imaginary part of the angular frequency Γ denotes the damping of the wave with the angular frequency ω_0:

$$e^{-i\omega t} = e^{-\Gamma t} e^{i\omega_0 t}. \tag{2.40}$$

The damping is usually expressed in terms of the quality factor Q. The quality factor, or short Q factor, is defined as the ratio of stored energy to energy loss in a resonator multiplied with 2π [17]. This definition can be transformed and written as ratio of mode energy E and linewidth (FWHM) ΔE of a resonator:

$$Q = \frac{E}{\Delta E} = \frac{\omega_0}{\Gamma'}, \tag{2.41}$$

where $\Gamma' = 2\Gamma$. In equation (2.39) Γ denotes the damping of the field amplitude, while Γ' in equation (2.41) stands for the damping of the emission intensity. The emission intensity is proportional to the square of the field amplitude and decays with $e^{-2\Gamma t}$. We thus write for the Q factor:

$$Q = \frac{\omega_0}{2\Gamma} = \frac{k_{re}}{k_{im}}. \tag{2.42}$$

With the complex k vectors we can now calculate the theoretical Q factor for a given microdisk. The Q factor can be seen as a measure for the tunneling probability of the field inside the microdisk. Theoretically determined Q factors are usually very large, which means that k_{re} and k_{im} are orders of magnitude apart. The calculation of very high theoretical Q factors requires caution, since the processed numbers easily go beyond the usual (double) computer precision. E.g. the calculation of the field distribution in figure 2.7 yields Q factors of $Q = 1.4 \cdot 10^{17}$ for a TE $m = 40$, $l = 3$ mode and $Q = 4.0 \cdot 10^{15}$ for the corresponding TM mode. For higher m and lower l the Q factors increase, but are not calculated correctly by our program[2]. We observe that the TE modes have significantly higher Q factors than the TM modes with same mode numbers. Such high Q factors cannot be observed in real experiments, since other factors predominantly limit the Q factors. The most important ones are scattering due to surface roughness or lattice impurities and absorption. The absorption may have two causes: intrinsic absorption and excitonic absorption in the quantum dots. We expect the intrinsic absorption to be very small, since the resonant energies are well below the bandgap of the microdisk bulk material. While intrinsic absorption is a constant factor, the excitonic absorption is not. Excitonic absorption is a process that depends on the excitation intensity and is thus a non-linear effect. Due to the Pauli exclusion principle, a photon can only be absorbed into an unoccupied energetic state by a quantum dot. With increasing excitation intensity, however, the rate at which excitons are generated can exceed the recombination rate of the excitons. Now all energetic states of the quantum dots are permanently occupied and the material becomes transparent with respect to excitonic absorption. For low excitation intensities, we thus expect the intrinsic absorption effect to be much smaller than the

---

[2] We used the program IGOR Pro by Wavemetrics to carry out the calculations.

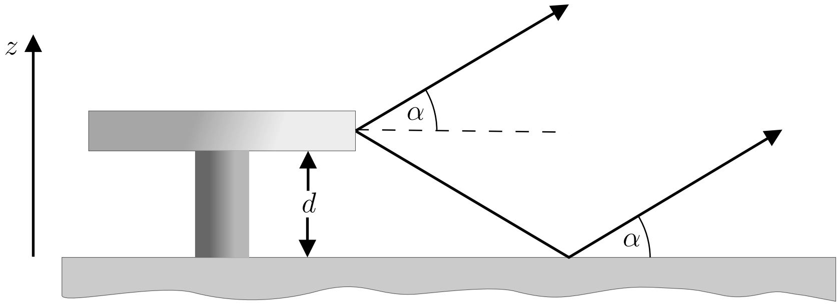

Figure 2.8: Schematic illustration of the emission in z direction. The microdisk emits light in an angle measured relative to the microdisks ρ-φ plane. For negative α, light can be reflected from the substrate and interfere with light which was emitted in a positive α range.

excitonic absorption effect. We assign for each damping process Γ a Q factor. Since the Q factors are reciprocally proportional to Γ, the total Q factor is [14]:

$$\frac{1}{Q_{tot}} = \frac{1}{Q_{tunnel}} + \frac{1}{Q_{abs}} + \frac{1}{Q_{scatter}}. \tag{2.43}$$

Since the total Q factor in equation 2.43 is intensity dependent, it is not per se a reliable way to measure for the quality of the cavity. Thus, the Q factor of the cavity should be measured at the point, where the excitonic absorption process begins to bleach. At this point, all contribution to the total Q factor depend on linear effects and thus deliver a comparable total Q factor for the microdisk cavity. Research on similar systems have shown that the biggest impact in the total Q factor has $Q_{scatter}$ [18, 19]. Thus, the best way to enhance the total Q factor is by minimizing the surface roughness.

2.4 Far-field emission characteristics

In the above sections we found a way to calculate the energetic position of whispering-gallery modes as well as the field distribution in a microdisk. This section analyzes the far-field emission characteristics of ordinary and pierced microdisks. We neglect the contribution to the photoluminescence emission caused by random scattering due to surface roughness. We would like to point out, that scattering plays nonetheless a vital role in the detection of whispering-gallery modes in our setup as we shall see later.

2.4.1 Ordinary microdisks

Due to the rotational symmetry, the far-field emission of ordinary microdisks in φ direction varies according to the near field distribution calculated in the previous section. Thus, in φ direction there is no preferential emission direction.

Let us analyze the emission distribution in z direction in terms of an emission angle α. Figure 2.8 illustrates a microdisk with a distance d from the substrate. For now, we

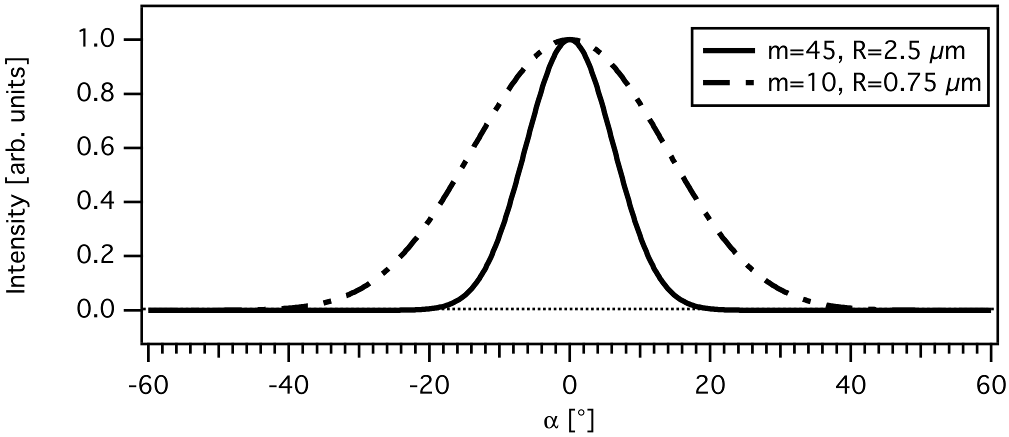

Figure 2.9: Far field intensity distribution along the z direction for an isolated microdisk with $R = 0.75$ µm with the whispering-gallery mode $m = 10$, $l = 1$ (black line) and for a microdisk with $R = 2.5$ µm with the whispering-gallery mode $m = 40$, $l = 1$ (gray line).

neglect the influence of the substrate on the far-field emission distribution and treat the microdisk as an isolated slab. In our experiments we observe spectra in the wavelength range from 850 nm to 1100 nm. The wavelength of a typical whispering-gallery mode is thus large compared to the height of the microdisk with $H = 250\,\text{nm}$. If we apply the classical Fraunhofer diffraction theory to this problem, the emission angle α spreads over almost $\pi/2$. In experiments this emission angle proves to be much smaller. The far-field emission distribution can be obtained by using a scalar diffraction theory developed by Lee et al. [20]. According to the scalar diffraction theory the angular intensity distribution is proportional to the absolute square of a Hankel function of the second kind:

$$I_{iso}(\alpha) \propto \left|H_m^{(2)}(kR\cos\alpha)\right|^{-2}, \tag{2.44}$$

with R being the radius of the microdisk and k the wave vector of a resonant whispering-gallery mode. We can easily calculate the angular field distribution in z direction. Figure 2.9 shows the whispering-gallery mode field distribution for two different microdisks. The dashed line depicts the field distribution for the mode numbers $m = 10$, $l = 1$ in a microdisk with a radius of $R = 0.75$ µm and the solid line for $m = 45$, $l = 1$ in a microdisk with a radius of $R = 2.5$ µm. Both disks were calculated for the same height of $H = 250\,\text{nm}$. The difference in the angular field distribution for TE and TM modes is so marginal that figure 2.9 does not allow for the distinction of the polarizations. Both emission distributions reside in a quite narrow angle $\alpha < 20°$.

Peter et al. report that the substrate alters this emission distribution [21]. They argue, that the substrate reflects the downwards directed part of the light, which then interferes with the upwards directed part of the light. Figure 2.8 illustrates this circumstance. The resulting angular field distribution is now determined by

$$I(\alpha) = I_{iso(\alpha)} \cdot \left|1 + r(\alpha)e^{i2kd\sin\alpha}\right|^2, \tag{2.45}$$

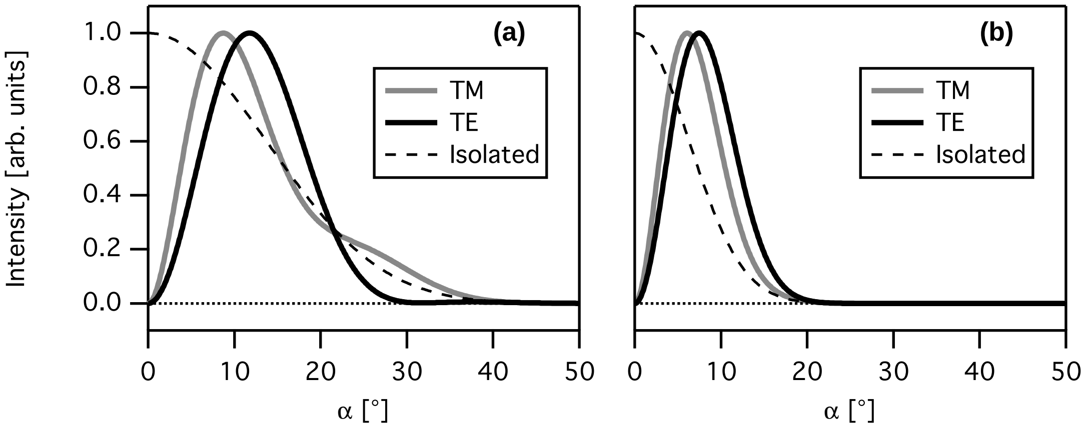

Figure 2.10: Angular far-field intensity along the z direction for a microdisk above a substrate with $R = 0.75\,\mu\mathrm{m}$ (a) and $R = 2.5\,\mu\mathrm{m}$ (b). The field distributions are calculated for a whispering-gallery mode with $m = 10$, $l = 1$ (a) and $m = 40$, $l = 1$ (b). Contrary to the case of an isolated microdisk (depicted as dashed line) the field distribution now vanishes for $\alpha \to 0$ due to reflection on the substrate and subsequent far-field interference.

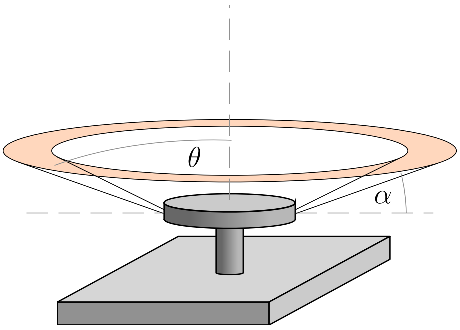

Figure 2.11: Spatial view of the far-field emission area of a microdisk on a substrate. Light is emitted in a narrow region in hollow cone with an opening angle of θ.

where $r(\alpha)$ is the reflection coefficient from the substrate, k the wave vector of a whispering-gallery mode and d the distance of the microdisk from its substrate (cf. figure 2.8). The reflection coefficient in dependence of the emission angle α can be derived from the Fresnel Formulae (2.2) and is thus different for TE and TM polarization. We calculated the angular far-field distribution with this method for the same whispering-gallery modes shown in figure 2.9. We assumed a distance of the microdisk to its substrate of $d = 1\,\mu\mathrm{m}$. The result is shown in figure 2.10. Contrary to microdisks isolated from its substrate, the angular far-field intensity vanishes for $\alpha = 0°$. In this model, the far-field emission takes place in an hollow-cone shaped volume as depicted in figure 2.11.

We conclude that the far-field intensity distribution for ordinary microdisks is uniformly distributed along the φ direction, and highly directional along the z direction. According to Peter et al. the far field vanishes in the microdisk's plane.

We emphasize that this intensity distribution is valid at larger distances from the microdisk. In the near field range we expect the emission intensity distribution to be more accurately described by equation 2.45. Since the light must be reflected on the substrate in order to interfere, the distance g from where this interference may occur can be estimated with $g > 2d/\tan(\alpha_{max})$. For an etching depth of $d = 500\,\mathrm{nm}$ and a maximum emission angle of $\alpha_{max} = 20°$ for a microdisk with $R = 2.5\,\mu\mathrm{m}$, we find roughly that $g > 2.75\,\mu\mathrm{m}$.

2.4.2 Pierced microdisks

As stated in the previous section, microdisks exhibit no preferential emission direction in the ρ-φ plane. For technical purposes a unidirectional emission behavior is often desired. Several methods have been investigated to achieve this goal. Maybe the most obvious way to obtain directional emission in φ direction is to introduce a discontinuity in the boundary of the microdisk where whispering-gallery modes can scatter out in a desired direction. This method is realized in spiral-shaped microdisks, first investigated by Chern et al. [4]. Their spiral-shaped microdisk contains a notch at the microdisks edge which leads to the desired unidirectional emission behavior within an angular range of roughly 30°. The whispering-gallery modes shown in their work are quite broad, resulting in quality factors of about $Q \approx 80$. These very low Q factors constitute the major drawback of this method. Another method is to continuously change the shape of the microresonator like the asymmetric resonant cavities. Most realizations of this method dealt with the problems that either the emission was not strictly unidirectional and had multiple output beams [7–9, 22, 23], or that again the Q factors suffered from the shape change [10].

A different approach was developed theoretically by Jan Wiersig and Martina Hentschel based on coupling a low-Q mode with unidirectional emission to a high-Q mode [11]. Let us assume two whispering-gallery modes energetically close together with a tunable energy of one of the whispering-gallery modes. When the whispering-gallery modes approach one another they do not cross each other, but can interchange mode properties in a process called avoided resonance crossing. Avoided resonance crossings occur in two regimes: a strong and a weak coupling regime. The strong coupling exhibits a frequency repulsion and linewidth crossing. In this regime, the resonant eigenstates interchange their identity and accordingly all the spatial characteristics switch their identity as well. The weak coupling is characterized by a linewidth repulsion and a frequency crossing. Here, the resonant eigenstates keep their identity and intermix at the crossing point. The idea is to hybridize a high-Q whispering-gallery mode and unidirectional low-Q mode to a mode with a high Q factor and the directed far-field emission of the low-Q mode. This is realized by piercing a geometrical hole into a microdisk. Figure 2.12 taken from their publication demonstrates this concept[3]. A whispering-gallery mode with the radial mode number $l = 3$ is affected by the hole and is emitted unidirectionally out of the microdisk as shown in figure 2.12 (a). Due to the emission, this whispering-gallery mode has a low

---

[3] Their calculations are based on a microdisk with a radius of $R = 1\,\mu\mathrm{m}$. They calculate an effective refractive index of $n_{eff} = 3.3$ for a $GaAs$ slab with a thickness of $H = 375\,\mathrm{nm}$ at a temperature of $4\,\mathrm{K}$ and a free space wavelength of $\lambda = 900\,\mathrm{nm}$.

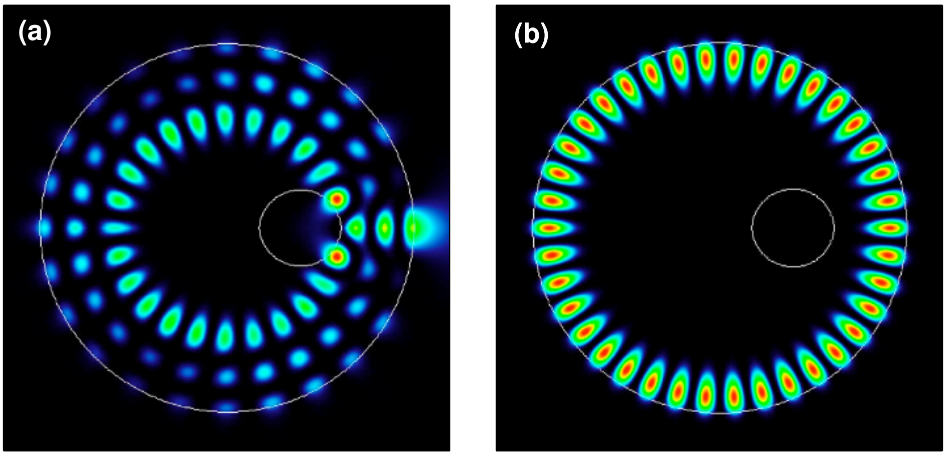

Figure 2.12: Illustration taken from Wiersig and Hentschel [11]. The images demonstrate the principle of mode hybridization in pierced microdisks. (a) A whispering-gallery mode with $l = 3$ is strongly influenced by an air hole and emits highly directed by refractive escape resulting in a low Q factor. (b) A whispering-gallery mode with $l = 1$ is almost unaffected by the hole and maintains a high Q factor. Hybridization of these two whispering-gallery modes near avoided resonance crossings can lead to a unidirectional high-Q whispering-gallery mode.

Q factor. A whispering-gallery mode with $l = 1$ on the other hand is almost unaffected by the hole and maintains a high Q factor. It is possible to tune the position of the hole in a way that both whispering-gallery modes hybridize at an avoided resonance crossing. Jan Wiersig and Martina Hentschel have simulated this phenomenon systematically for varying hole-positions and -sizes using a boundary element method [24].

3 Experimental setup

3.1 The micro-photoluminescence setup

All experiments except the characterization measurements were carried out in our micro-photoluminescence setup. The micro-photoluminescence setup employs a confocal microscope system for excitation and measurement. In a first step, a microscope objective focusses a laser beam on a sample for excitation. The photoluminescence emission of the sample is then collected by the same microscope objective and coupled into a spectrometer for spectral analysis. We will now explain the parts of micro-photoluminescence setup in the order of the incident light from excitation to spectral analysis.

Our micro-photoluminescence setup is illustrated in figure 3.1. We used two different lasers for photoluminescence excitation, depicted by the laser box in figure 3.1. These are a Helium-Neon ($HeNe$) laser emitting at 633 nm and a Titan:Sapphire ($Ti{:}Sa$) laser tunable in a wavelength range approximately from 690 nm to 810 nm. The $Ti{:}Sa$ laser is pumped by a high power solid state laser emitting at 532 nm. In rare occasion the latter was used as an excitation source as well. All three lasers emit polarized light.The excitation intensity can be attenuated with either a combination of neutral filters, or with a combination of a Fresnel rhombus and a Glan-Taylor prism. In the latter configuration, the excitation intensity can be attenuated smoothly by rotating the polarization plane with the Fresnel rhombus against the fixed Glan-Taylor prism which acts as a beam polarizer. Optionally, a hinged beamsplitter can be used to divide the attenuated excitation laser beam. This allows to measure and control the laser power during an experiment. Prism 1 diverts the excitation laser beam on to a beamsplitter which couples roughly 10% of the incident laser intensity into a microscope objective. The microscope setup provides three different objectives (20×, 50× and 100× magnification) mounted on a revolver, so that each objective can be quickly inserted into the beam line by rotating the revolver. The microscope objective focusses the excitation laser beam through a small window in a cryostat on a sample. Depending on the microscope objective, the spot has a minimal diameter between 1 µm and 3 µm. Sometimes, a nonfocussed, broad excitation beam is desired. In this case, the excitation laser beam needs to be widened with a concave lens between prism 1 and beamsplitter. The concave lens is mounted on a hinge. Once properly adjusted, it can be quickly inserted or removed from the beam line without further adjustment.

A cryostat[1] cools the sample with a continuous flow of liquid helium and is equipped with a resistor heater. In the cryostat, a sample can be brought to constant temperatures

---

[1] CryoVac Konti-Cryostat-Mikro

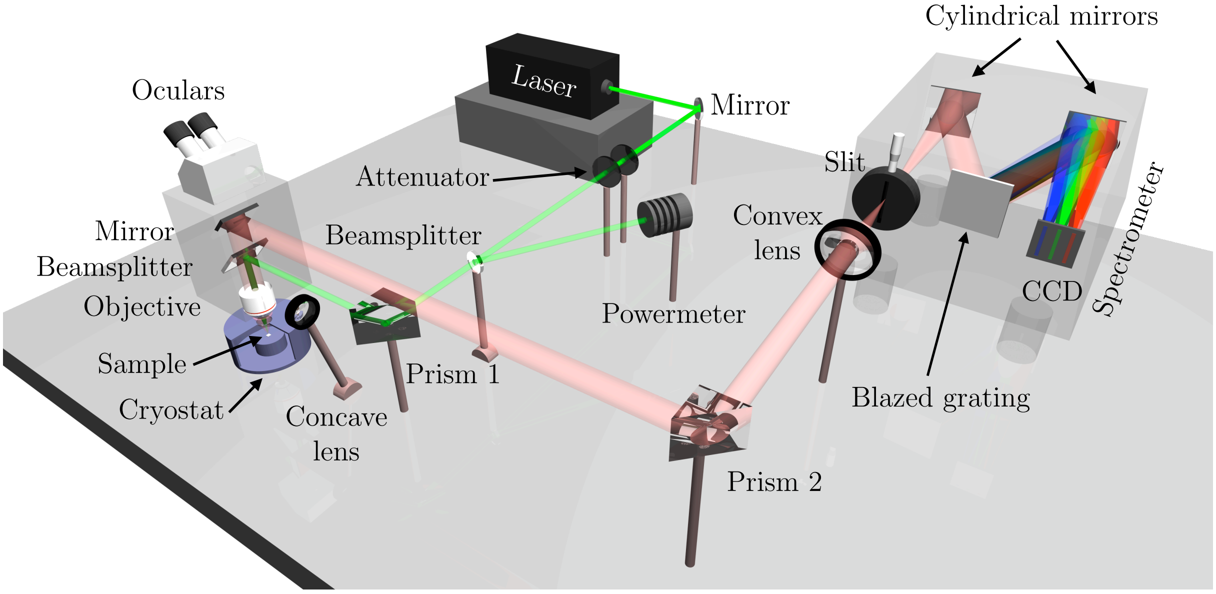

Figure 3.1: Schematic confocal micro-photoluminescence setup. One underlying feature of the setup is the coincidence of the sample surface with the focal plane of microscope objective. The light from each point on the sample is thus transformed into a parallel beam behind the microscope objective. To obtain an image of the sample a lens has to be placed in the beam line behind the microscope objective. The projection length of the lens is again the same as the focal length. An image is generated optionally in the oculars or on the slit and on the CCD chip. The spatial information of the image on the CCD camera is preserved only in the vertical direction.

between 3 K and room temperature. The sample itself is mounted on a x-y translation-stage. The stage is controlled by stepper motors and allows for adjustability in the x-y plane with a resolution of 10 nm. It is possible to control the stage with either a joystick or remotely through a computer which allows for automation of the stage motion.

The photoluminescence light emitted by the sample is collected by the same microscope objective that was used for excitation. A specific feature of the microscope setup is that the sample surface coincides with the focal plane of the microscope objective. As a result each point on the sample surface is widened to a parallel beam behind the objective. A second lens is necessary to obtain an image from the light beam behind the objective. The image distance behind this lens would then again coincide with the focal length of the lens. With the object length being identical to the focal length, we gain the advantage that we can focus the excitation laser beam on the sample and observe an image of the sample surface simultaneously.

Following the beam in our setup, 90% of the beam now passes the beamsplitter on to a hinged mirror. The mirror can be placed in two positions: either out of the beam line in order to allow the observation of an image in the oculars of the microscope or in the beam line to divert the photoluminescence signal to the spectrometer. In the latter position, the diverted photoluminescence signal then hits prism 2 and is focussed by a convex lens onto a vertically aligned slit in front of the spectrometer thus projecting an image of the sample on the slit. A part of the image passes through the slit. This light first hits a cylindrical mirror, which parallelizes the beam again and reflects it towards a grating. We used a blazed grating optimized for a wavelength of $\lambda = 750\,\mathrm{nm}$ and with 1200 lines per millimeter. The diffracted beam then is reflected by a second cylindrical mirror which finally focusses the now energetically resolved beam on a CCD chip. The grating can be rotated around its vertical center with a stepper motor to cover a large observable energetic range. If the grating is rotated to the zeroth order diffraction, it acts as a plain mirror. Furthermore, the focal lines of the cylindrical mirrors in the spectrometer coincide with the slit and the CCD camera. With the grating in zeroth order diffraction and a completely opened slit, we can take an image of the sample with the CCD camera. Note that in the first order diffraction the horizontal position information is lost due to the diffraction, but the vertical position information is still conserved. This imaging behavior can be utilized to create energy resolved images of the sample.

Consider a sample mounted on the stage of the cryostat. An image of the sample is projected on the slit in front of the spectrometer as shown in figure 3.2 (a). A part of the image passes the slit and is diffracted by the grating, which projects the image according to its wavelength in different positions on a CCD chip, as illustrated in the middle column in figure 3.2. In this projection the spatial information in x direction is generally lost, but the spatial information in y direction is conserved. Note that for each energy the part of image that passes the slit is still preserved in x direction. This means, that the slit width has a direct influence on the energetic resolution of the spectra. By repositioning the sample with the moveable stage of the cryostat, the image on the slit can be moved as illustrated in figure 3.2. The corresponding spectrum shown in the middle column exhibits the same energetic features as before, but with different y-position information.

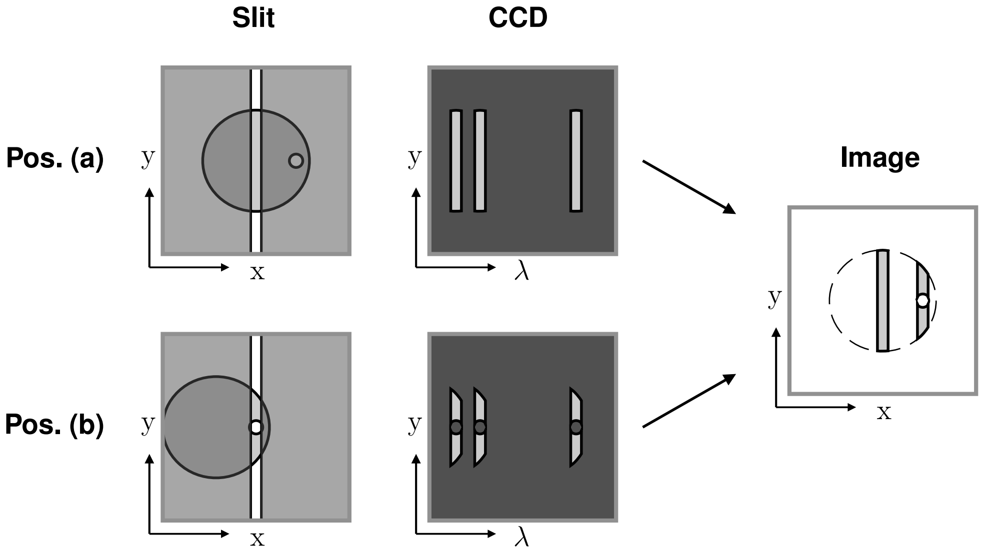

Figure 3.2: Image construction in the micro-photoluminescence setup. (a) projected sample image on the slit and diffracted image on the CCD camera. The x-position information is lost in the diffracted image whereas the y-position information is preserved. (b) same images, this time the sample image on the slit is moved. With the knowledge of the image positions, it is now possible to assemble the two lines spatially any wavelength λ. Applying this technique to many positions over a microdisk yields spectrally and spatially resolved images of the sample.

With the knowledge of the slit position over the sample it is now possible to assemble a spatially resolved image from the two spectra at any energetic position as demonstrated in the last column in figure 3.2. We apply this technique for up to 30 positions over a single microdisk. Compared to the resolution of the CCD camera, such images have a very low resolution in x direction, but by applying interpolation techniques on the resulting images we can achieve very good approximations to completely spatially and energetically resolved images of the sample.

One part of this work focusses on the emission behavior of the microdisks in the ρ-φ plane. The angular far-field emission distribution in z direction of a microdisk on a substrate is discussed in section 2.4.1 and illustrated in figure 2.11. We now look at the aperture θ of our microscope objectives in order to ascertain if the objectives can collect the far-field emission of a microdisk when their optical axis is aligned in z direction. Figure 3.3 schematically depicts a microscope lens above a sample. The numerical aperture NA of the microscope objectives is given by the manufacturer. From the numerical aperture we determine the angular aperture θ through:

$$NA = n \cdot \sin\theta, \tag{3.1}$$

where n is the refractive index of the material between lens and sample, thus $n = 1$ in our case. The minimal angle at which light may escape from a microdisk and be collected by the microscope objective is thus $\alpha_{min} = 90° - \theta$. We know the angular far-field emission distribution for a given microdisk on a substrate and can now compare it with α_{min}. The table below lists NA and the corresponding α_{min} for each microscope objective.

Magn.	NA	α_{min}
20×	0.40	66.4°
50×	0.50	60.0°
100×	0.80	36.9°

Compared to the typical angular distributions obtained in section 2.4.2, the values α_{min} are quite large. Since the microdisk's ρ-φ plane is perpendicular to the optical axis of the microscope in all our experiments, we might not be able to observe the far field whispering-gallery mode emission directly. Nontheless, all experimental spectra shown in the chapters 5 and 6 were taken with this setup and excellently show spectral features. We therefore suggest that the observed whispering-gallery modes in this setup are well detectable by scattered light due to surface roughness or intentionally introduced scattering objects. This method probably leads to decreased intensity detection compared to a tilted sample [18]. We gain on the other hand the ability to compile energetically resolved emission images using the technique described above and are still able to observe spectral features.

3.2 The macro-photoluminescence setup

We conclude this chapter by giving a brief introduction into the macro-photoluminescence setup. This setup was used to perform characterization experiments of our samples.

Figure 3.3: Angular aperture θ of a microscope objective. Light emission in an angle below α_{min} cannot be detected directly, if the optical axis of the microscope objective is aligned in z direction. Typical emission angles of our microdisks are below α_{min}.

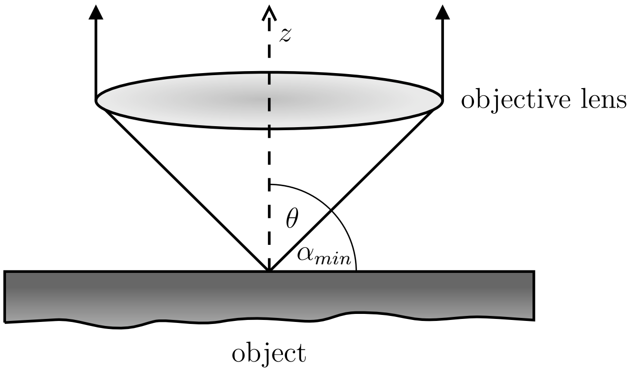

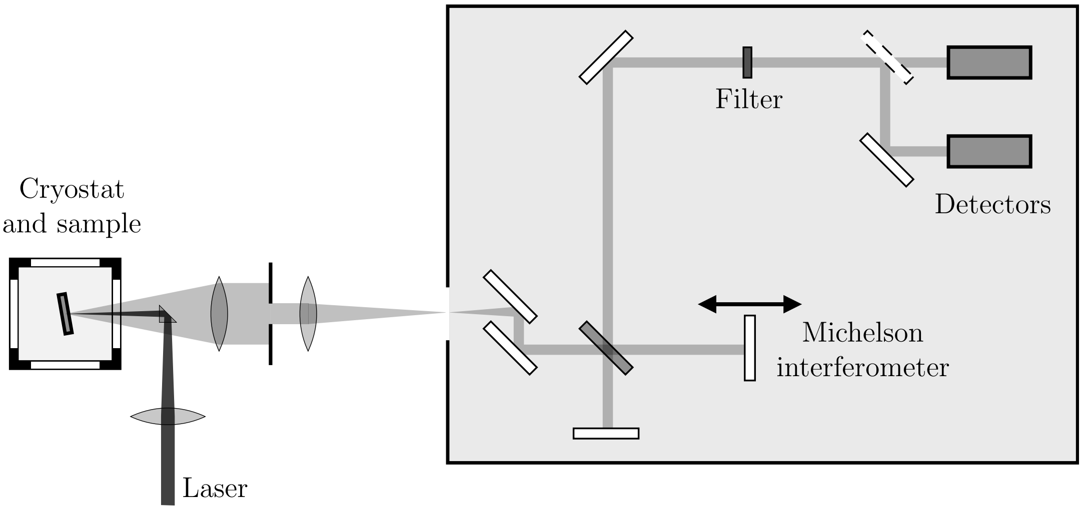

Figure 3.4: Illustration of the macro-photoluminescence setup. The Fourier transform spectrometer (gray box) consists of a Michelson Interferometer which decomposes the photoluminescence signal by constantly moving one mirror of the interferometer back and forth. This results in an interferogram which can be transformed into a spectrogram via Fourier transformation.

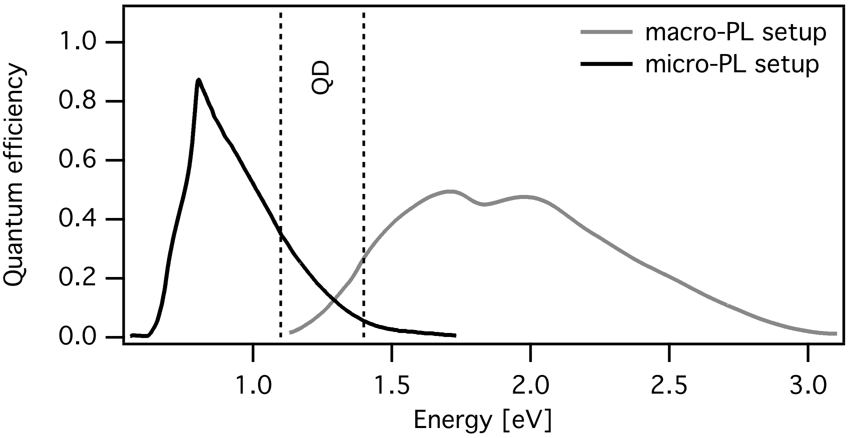

Figure 3.5: Quantum efficiencies of the *Ge* detector in the macro-photoluminescence setup and the *Si* Detector in the micro-photoluminescence setup. The typical emission range of the quantum dots used in our experiments is indicated by the dashed lines.

Figure 3.4 illustrates the macro-photoluminescence setup. In this setup an Ar^{+}-laser beam is focussed through a lens and a small prism on the sample. The minimal spot diameter in this setup is roughly 120 µm. The sample is mounted in a continuous flow cryostat and can be cooled down to temperatures around 3.5 K. The photoluminescence emission is collected by a lens and coupled into the spectrometer by a second lens. The signal is spectrally dissected by a Fourier transform spectrometer before it is detected. The interferogram is analyzed by a computer and transformed into a spectrum. A filter in the beam line prevents the detector from being exposed to the laser light. Two detectors can be used in this setup without manual interaction, but for our purposes a *Ge* detector was mainly used. Its sensitivity ranges from 0.6 eV to 1.7 eV with a maximum quantum efficiency at 0.8 eV as depicted in figure 3.5. For comparison the quantum efficiency of the *Si* detector in the micro-photoluminescence setup is shown as gray line in figure 3.5. The sensitivity maximum in the micro-photoluminescence setup is around 1.8 eV.

These sensitivities have an impact on the measurements, since the energetic quantum-dot photoluminescence-emission range lies in a region where the sensitivity of both detectors depletes. With the data of both detectors we can gather information about the quantum-dot photoluminescence-emission.

4 Preparation

The fundamental optical properties of a semiconductor microdisk are determined in the fabrication process. Apart from obvious microdisk properties which affect the optical characteristics, like material and shape of a microdisk, the smoothness of a microdisk's surface has a significant effect on the quality factor of the optical cavity. Our fabrication process was thus designed with the goal to be flexible with respect to the microdisk's shape and to deliver very smooth microdisk surfaces. The basic fabrication principle is the same for ordinary and pierced microdisks. The difference between the two is merely the lateral sample structure and layout. In this chapter, we therefore only discuss this basic fabrication principle and explain the lateral sample structure and layout in the appropriate analysis chapters. Since the introduction of an air hole has certain implications on the etching process, we explain the whole process on the example of the slightly less intuitive pierced microdisks. During this explanation, the fabrication process of ordinary microdisks becomes implicitly evident.

4.1 Vertical sample structure

Our microdisks are fabricated in a two step wet etching process on a sample taken from a multi-layered wafer. Each wafer layer has a certain purpose in either the fabrication process or in the experiments with the microdisks. Our wafers are grown in the molecular beam epitaxy system of the research group of Prof. Hansen at the University of Hamburg. Three wafers were used for this work, which carry the numbers #1624, #1625 and #1855. These wafers basically have all the same layer structure and differ in the characteristics of the buried $InAs$ quantum dots. Figure 4.1 illustrates this layer system. We will briefly describe each layer with respect to its function in a microdisk.

The wave guiding part of the microdisk consists of the upper seven layers. Located in the middle of these layers is a thin $InAs$ layer which contains self-assembled quantum dots grown in Stranski-Krastanov growth mode. This quantum dot layer nominally has a thickness of 2.5 atomic monolayers. The quantum dots are used as an internal light source for whispering-gallery mode excitation. The buried $InAs$ quantum dot layer is sandwiched in layer system of a 248 nm thickness, similar to the sample layout used by Gayral et al. [19]. This layer system constitutes the actual waveguide. The waveguide consists mainly of $GaAs$. Two $AlGaAs$ layers of 20 nm thickness are grown near the top and bottom surfaces of the disk. Since $AlGaAs$ has a larger band gap than $GaAs$, these layers act as a repulsive potential barrier for excitons in the microdisk. Due to this barrier the exciton density near the $InAs$ quantum dots is supposed to rise. The 4 nm

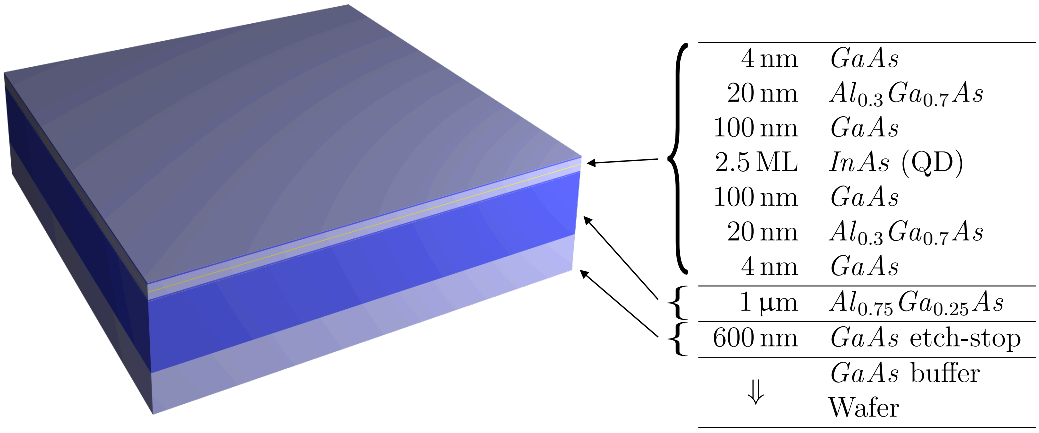

4 nm	$GaAs$
20 nm	$Al_{0.3}Ga_{0.7}As$
100 nm	$GaAs$
2.5 ML	$InAs$ (QD)
100 nm	$GaAs$
20 nm	$Al_{0.3}Ga_{0.7}As$
4 nm	$GaAs$
1 µm	$Al_{0.75}Ga_{0.25}As$
600 nm	$GaAs$ etch-stop
⇓	$GaAs$ buffer Wafer

Figure 4.1: The wafer structure predefines the vertical dimensions of a microdisk. The disk consists of the seven upper layers with a height of 248 nm. The pedestal is formed out of the 1 µm $AlGaAs$ below, which can be selectively etched. A 600 nm $GaAs$ layer acts as etch stop.

$GaAs$ cap layers prevent corrosion of the $AlGaAs$ layer below.

The layer below the wave guiding part is a 1 µm thick $Al_{0.75}Ga_{0.25}As$ layer. The pedestals of the microdisks are etched out of this layer. Due to the high aluminum concentration this layer can be selectively etched with hydrofluoric acid [25]. Generally, a higher aluminum concentration in $Al_xGa_{1-x}As$ makes the material more susceptible to corrosion in normal conditions. The chosen aluminum concentration is a compromise between good etching characteristics and stability.

An etch-stop below the pedestal layer consists of 600 nm $GaAs$. This layer prevents deep etching below 1 µm by the hydrofluoric acid.

4.2 Sample fabrication

The fabrication process of microdisks is illustrated in figure 4.2. The first step is to prepare an etching mask as illustrated in figure 4.2 (a). To achieve high accuracy and flexibility we use electron-beam lithography to structure our etching mask. First, a $4 \times 4\,\mathrm{mm}^2$ piece of the wafer is spin coated with electron-beam resist. Two different types of resist are used for different purposes: negative Allresist AR-N7520 is used for ordinary microdisks and positive Allresist PMMA 50K for pierced microdisks. Our etching masks are designed to contain hundreds of microdisks on one sample piece. Each single microdisk can later be unambiguously identified. The sample layout will be discussed in chapter 5 and chapter 6 for the according sample in more detail.

Once the etching mask is applied, we deep etch the sample with a hydrogen bromide based wet-etching solution as illustrated in figure 4.2 (b). The mixing ratio of the solution is 5 HBr : 2 H_2O_2 : 100 H_2O. Generally, an etching process can be reaction-rate limited or diffusion limited. In a reaction-rate limited etching processes the reaction is slow compared to the diffusion process. The etching rate of this process is predominantly controlled by the temperature of the reagent. Higher temperatures generally enhance the reaction speed. In diffusion limited etching processes the reaction is fast compared to the diffusion process. The etching rate in this process is enhanced by stirring the etchant. Hydrogen bromide is a strongly diffusion controlled acid. It is difficult to achieve reproducible results, since the diffusion is not easy to control reliably. We tried to keep the same conditions by constantly stirring the etching solution at 300 rpm. Furthermore, we rotated the sample while holding it in the tweezers continuously during the etching process to avoid anisotropic etching due to laminar streaming. With this method we achieved etching rates of between $5.5\,\mu\mathrm{m\,s^{-1}}$ and $15.6\,\mu\mathrm{m\,s^{-1}}$. This extreme variation in the etching rates reflects the difficulty in reproducing the exact same process parameters. Fortunately, we can perform the etching process step by step and control the progress of each step with an optical microscope. This etching step leaves behind residue material on the sample which can be effectively removed with developer.

In this first etching step, it is crucial to produce very smooth surfaces with an isotropic etching behavior. The surface smoothness has a strong influence on the quality factors of whispering-gallery modes [26]. Since surface roughness diminishes the quality factors, good surface smoothness leads to high quality factors of a microdisk. The isotropic etching behavior was investigated on pierced microdisks with the help of SEM images. Detailed results of investigations on the quality factors and the SEM images are presented in chapter 6. Here, we only state that our microdisks have whispering-gallery modes with very high quality factors and we can treat our etching solution as isotropic within reasonable limits.

The second etching step defines the pedestal of the microdisk by selectively etching the $AlGaAs$ layer with hydrofluoric acid as illustrated in figure 4.2 (c). We use a 0.5 % diluted HF solution. Hydrofluoric acid is a reaction-rate controlled process which gives us a good control over the etching rate.

We now turn to the special case of wet etching pierced microdisks. The disk parameters given by Wiersig and Hentschel [11] are too small to be realized with our preparation method. Due to the isotropic etching behavior of HBr, the microdisks have a minimal radius ultimately limited by the thickness of the microdisk slab. Isotropic etching implies an etching rate that is independent of the crystal axis. Thus the etching rate is the same in all directions. The effect of an isotropic etching solution brought on one point on a planar surface is semi spherical hole in this surface. Thus, the HBr etching step not only deep etches the sample, but diminishes the radius of each microdisk and increases the radius of the hole as illustrated in figure 4.3 (a). The radius decrease as compared to the etching mask is a direct measure for the etching depth. In order to fabricate steep boundary walls in the microdisk the etching depth needs to be considerably higher than the thickness of the microdisk slab.

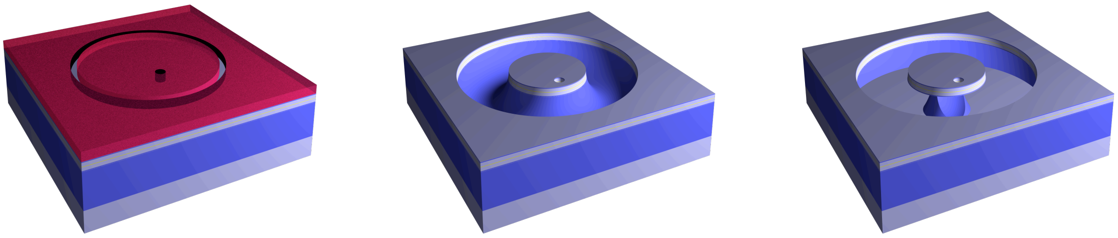

(a) Etching mask **(b)** HBr wet etch step **(c)** HF wet etch step

Figure 4.2: Illustration of the microdisk fabrication process. (a) shows a detail of a sample with the etching mask. (b) depicts the sample after the HBr wet etching step was applied. This step is crucial for the quality factor of the cavity. The use of hydrogen bromide as etchant leads to very smoothly etched surfaces. The selective HF wet etching step is illustrated in (c). In this etching step the pedestals of the microdisks are defined.

While the outer radius of a microdisk is decreased, the radius of an air hole is increased in the same etching step. The desire for steep boundary walls and deep etching is thus opposed by an increasingly large air hole. Since the microdisk slab has a thickness of 250 nm, we have aimed at an etching depth of roughly 500 nm as a compromise between steeply etched boundary walls and a small hole radius.

Due to the fact that HBr is strongly diffusion controlled and the hole in the etching mask is very small, the etching rate for the air hole is lower than for the edge. While the average microdisk radius is diminished by roughly 450 nm, the average radius of the hole increases only by 340 nm. This circumstance can be used to fabricate a steep microdisk edge and a comparably small hole. The hole itself does not have steep side walls, but rather the shape of an imprinted sphere. This wall in the hole is steeper for larger hole radii.

The HF etching step is illustrated in figure 4.3 (b). The acid selectively etches the $AlGaAs$ beneath the $GaAs$ wave guide. Now, the etching process is reaction-rate controlled and the pedestal is formed by hydrofluoric acid that comes from the side and through the hole. This leads to a peculiar sickle shaped pedestal, as illustrated by the dark area in figure 4.3 (b).

Due to the minimal hole size and a desired distance between the air hole and the outer boundary, the smallest microdisk radius is roughly $R_{disk} = 2.5\,\mu\text{m}$. Smaller microdisks would eventually lead to the disappearance of the pedestal. Our microdisks have an average radius of 2.8 µm as a compromise between a stable pedestal and a small microdisk radius.

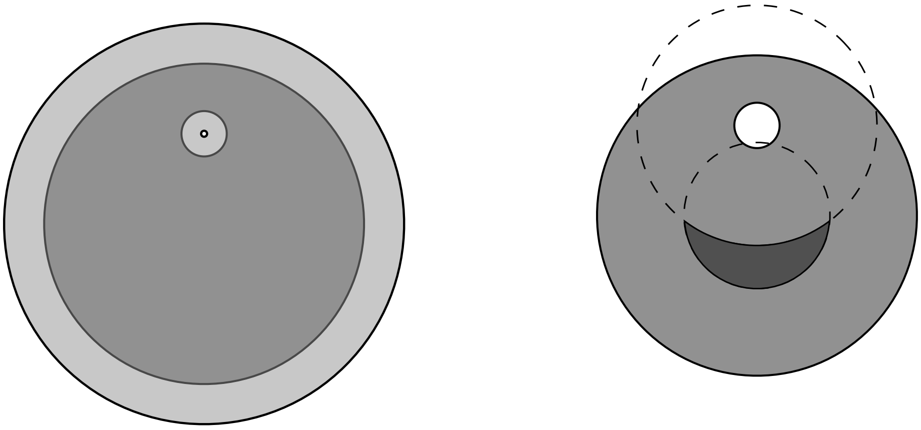

(a) HBr wet etching step

(b) HF wet etching step

Figure 4.3: Geometrical implication of the wet etching process. Both etching steps are isotropic. This leads to a reduction of the microdisk radius and a larger hole in the HBr etching step, as depicted in (a), where the light gray area depicts the etching mask and the darker gray area is the material beneath the mask. In the HF wet etching step, hydrofluoric acid can circulate through the hole and from the sides. As a result, the pedestal has a peculiar sickle shape depicted as the darker area in (b).

5 Ordinary microdisks

The following chapter covers the measurement of ordinary microdisks. We introduced the term *ordinary microdisks* to distinguish these microdisks from the later investigated pierced microdisks. This chapter is subdivided into four sections, all dealing with experiments on the same sample. The first section presents the photoluminescence spectra of an unstructured region on the sample. These spectra provide information about the energetic photoluminescence range of the embedded quantum dots. The second section discusses a micro-photoluminescence spectrum of a single microdisk. Here, we compare the experimentally obtained spectrum with a calculated mode spectrum for the investigated microdisk. This section focusses on the principle of mode allocation. The third section deals with nominally equally sized microdisks. The comparison of microdisks with nominally the same size reveals information about the accuracy of the preparation process. This information can be useful to find a sensible interpretation of the mode spectra. The last section of this chapter shows experiments performed on microdisks with different sizes. We compare a subset of microdisks with evenly increasing radius to the theoretical model presented in chapter 2 and interpret the observed spectra. This interpretation takes the results of the previous sections into consideration.

5.1 The sample

All investigated microdisks in this chapter are located on the same sample, which we shall refer to as sample A[1]. The fabrication principle and vertical structure of the sample is described in the previous chapter. In this section we investigate the photoluminescence of the embedded $InAs$ quantum dots and present the lateral sample layout.

In order to excite optical whispering-gallery modes, the investigated microdisks contain buried InAs quantum dots as an internal light source. The quantum-dot photoluminescence spectrum together with the physical dimensions of a microdisk determine which whispering-gallery modes can be observed. In this section, we investigate the photoluminescence spectrum of the sample without the influence of a cavity in order to gain knowledge about the light emitters inside the microdisks. The quantum dots are grown in self assembled Stranski-Krastanov growth mode using a Molecular Beam Epitaxy system run by the research group of Prof. Hansen of the University of Hamburg.

The quantum dot density on the wafer center is about $5.4 \times 10^{-9}\,\mathrm{cm}^{-2}$ and decreases towards the wafer edge. The confinement of excitons in a quantum dot leads to quantized

---

[1] The sample A is a $4\,\mathrm{mm}^2$ piece taken from near the center of the wafer #1625 with the internal name 1625-25.

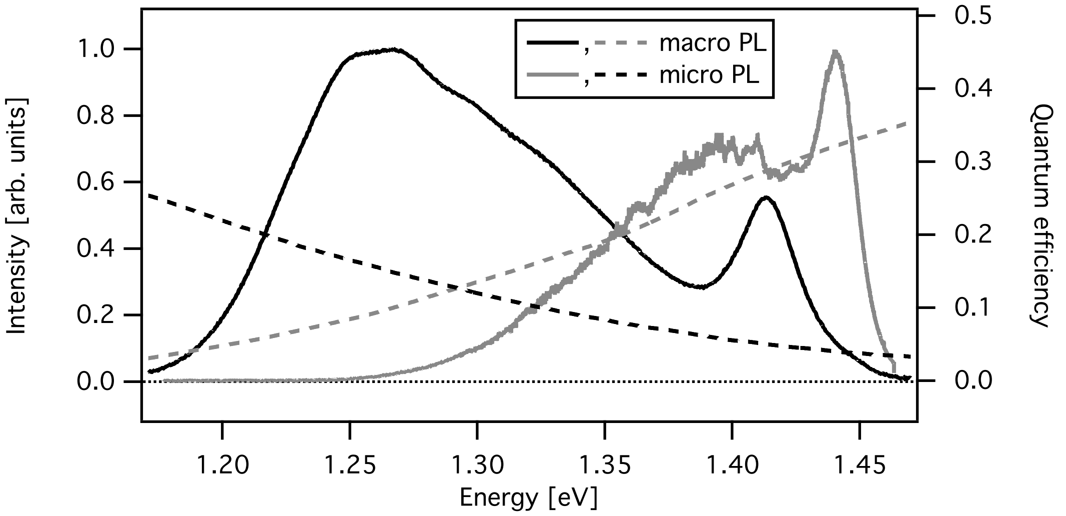

Figure 5.1: Photoluminescence spectra of an unstructured region of the sample A. The black curve is a spectrum taken with the macro-photoluminescence setup, the gray curve is a spectrum taken with the micro-photoluminescence setup (cf. chapter 3). Both spectra are normalized with respect to their highest intensity. The peaks near 1.43 eV in both spectra originate from the wetting layer. The dashed lines correspond to the right axis and illustrate the detector sensitivities of the two setups.

photoluminescence emission. The discrete energy levels are determined mainly by the size of a quantum dot. The lateral size of the quantum dots varies with a gaussian distribution. Thus, the photoluminescence emission spectrum is energetically broadened with a gaussian profile.

Figure 5.1 depicts two photoluminescence spectra of sample A. These spectra were taken in a region on the sample where the vertical wafer structure is intact but without microdisks. Here, photoluminescence light is not altered by microdisks and we can investigate the emission from the quantum dots without the influence of a cavity. The two spectra were taken with two different measurement setups. The black curve shows a spectrum taken with the macro-photoluminescence setup (cf. section 3.2) with a *Ge* detector at a temperature of $T = 3.6\,\mathrm{K}$. The gray curve shows a spectrum taken with the micro-photoluminescence setup (cf. section 3.1) with a *Si* detector at $T = 36.0\,\mathrm{K}$. Usually we expect the photoluminescence of the quantum dots to be the same, no matter what setup we use to observe it. The obvious differences in the two spectra basically mirrors the different characteristics of the two measuring methods. The *Ge* detector of the macro-photoluminescence setup has a higher sensitivity in the lower energy region compared to the *Si* detector of the micro-photoluminescence setup. The detector sensitivities are illustrated as the dashed curves in figure 5.1. In the investigated energy range, the sensitivity of the *Si* detector in the micro-photoluminescence setup increases strongly with increasing energy, while the sensitivity for the *Ge* detector decreases.

Accordingly, the micro-photoluminescence spectrum is strongly diminished on the low-energy side and the macro-photoluminescence spectrum is diminished on the high-energy side. In both setups other components, like mirrors, lenses or the blazed grating in the micro-photoluminescence have an energy dependent effect on the spectra.

Both spectra display a pronounced peak near 1.43 eV. We assign this peak to the photoluminescence of the wetting layer. The difference of 26 meV in the energetic positions of the two peaks is again due to the different characteristics of each measuring setup. The micro-photoluminescence spectrum was taken with a relatively low exciting power density of roughly estimated $30\,\mathrm{W\,cm^{-2}}$. The macro-photoluminescence spectrum on the other hand was taken with a comparatively high power density of approximately $13\,\mathrm{kW\,cm^{-2}}$ due to an overall lower sensitivity of the detector. The excitation energy is well capable of locally heating the sample against the cryostat cooling. Thus, we observe a thermally induced redshift of the $InAs$ band gap for the macro-photoluminescence setup. We can calculate the local temperature of the sample under the laser spot applying the observed red shift according to Varshni's empirical formula [27]. The red shift of $\Delta E \approx 23\,\mathrm{meV}$ corresponds to a local temperature of about $T \approx 150\,\mathrm{K}$ in the spot region. This seems to be a very high temperature even for the relatively high laser excitation power. We do not know the exact cause for the huge energy shift between the spectra, but we can nonetheless draw some important conclusions.

The photoluminescence energy of the quantum dots lies roughly between 1.15 eV and 1.42 eV. At about 1.44 eV we observe the photoluminescence signal of the wetting layer. The highest intensity of the quantum-dot photoluminescence-emission is roughly at 1.26 eV. The spectra of the micro-photoluminescence setup, which we use for all further investigations, are strongly suppressed for lower energies. We will henceforth concentrate on the peak positions and on the width of the peaks instead of the measured intensity, since the intensity is strongly influenced by the setup and the real photoluminescence intensity cannot be easily reconstructed. Even the comparison of relative intensities in a single spectrum must be dealt with care without the knowledge of the spectral behavior of all optical components in a setup.

We will now briefly present the lateral layout of the sample A. Sample A contains three fields with 320 microdisks per field. The three fields were fabricated with the same preparation parameters for redundancy reasons. Only one of the three fields was investigated. Figure 5.2 (a) is a microscope image of this investigated field. Each microdisk on the sample can be unambiguously identified. In figure 5.2 (a) 20 subsets with 16 microdisks per subset are visible. These subsets are numbered with a chessboard-like system. The radius of the microdisks gradually increases from subset to subset in the order from a1, b1, …, e4. Each subset contains 16 microdisks with nominally the same radius. To identify a microdisk within a subset we again use the chessboard naming convention and append the name to the subset's name. This means, e.g. the lowermost left microdisk in figure 5.2 (a) is named a1a1 and the uppermost right microdisk is named e4d4. The encircled microdisks display a sequence of 20 microdisks with uniformly increasing radii. These microdisks are investigated in section 5.4. The arrows in figure 5.2 (a) indicate the order of microdisks from small to large radii. The cross in the lower left corner between

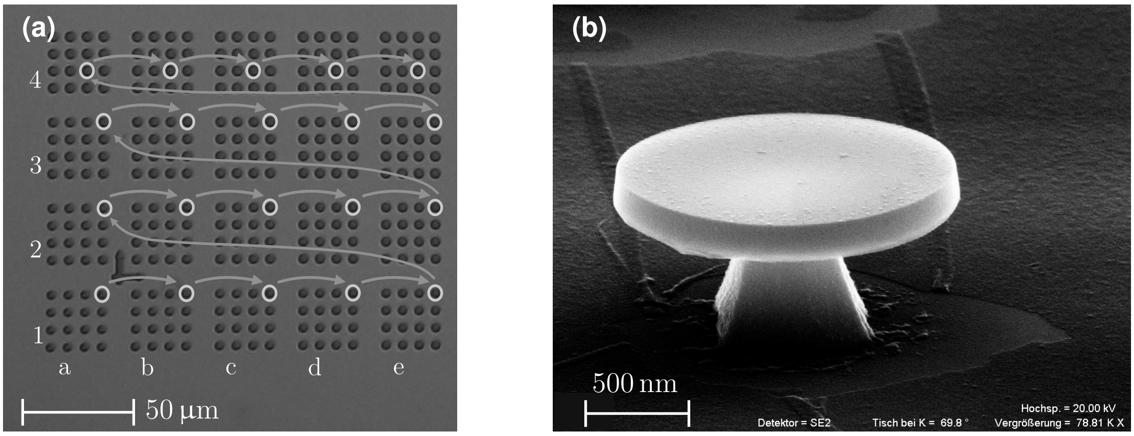

Figure 5.2: (a) Microscope image of the sample structure. The microdisks are arranged in 20 subsets. Each subset contains 16 microdisk with nominally the same size. The encircled microdisks indicate the measured microdisks with increasing radius for the experiment presented in section 5.4. The arrows indicate the order of the microdisks with increasing radius. (b) SEM image of a microdisk on the sample A.

the subsets of microdisks is used to find the correct orientation of the sample.

Figure 5.2 (b) is a SEM image of the microdisk b2a1. The image shows examplarily the characteristics of the microdisks investigated in this chapter. These are the steep, very smooth side walls and small pedestal as a result of the wet-etching fabrication technique.

5.2 Single microdisk spectra

Before we turn to the methodical investigation and comparison of multiple microdisks, let us analyze a photoluminescence spectrum of a single microdisk and explain the approach for whispering-gallery mode identification in this spectrum.

We investigate a spectrum of the microdisk b2d4. In order to calculate the whispering-gallery mode distribution, we need to know the exact dimensions of the microdisk. The thickness is predefined in the growth process to be 250 nm, which we assume to be quite accurate. Unfortunately, we cannot determine the radius of the microdisk b2d4 directly, since this sample is lost. We can, however, estimate the radius of the microdisk b2a1 with nominally the same radius as b2d4. From the SEM image 5.2 (b) the radius of the microdisk b2a1 can be determined to $R = 1.047\,\mu\text{m} \pm 0.030\,\mu\text{m}$. Since the microdisks b2d4 and b2a1 were fabricated with the nominally same radius, we take the radius of the microdisk b2d4 to be $R = 1.047\,\mu\text{m} \pm 0.030\,\mu\text{m}$ as well. The reason for the comparatively large error in the size determination is the very short length scale in the SEM image. Note that the ordinary microdisks have rather small radii compared to the pierced microdisks, since their minimal radius is not limited by an air hole as explained in chapter 4.

Figure 5.3 shows a micro-photoluminescence spectrum of the microdisk b2d4. The intensity is plotted on a logarithmic scale against the energy. The whispering-gallery modes are visible as sharp peaks on the broad background photoluminescence signal of the

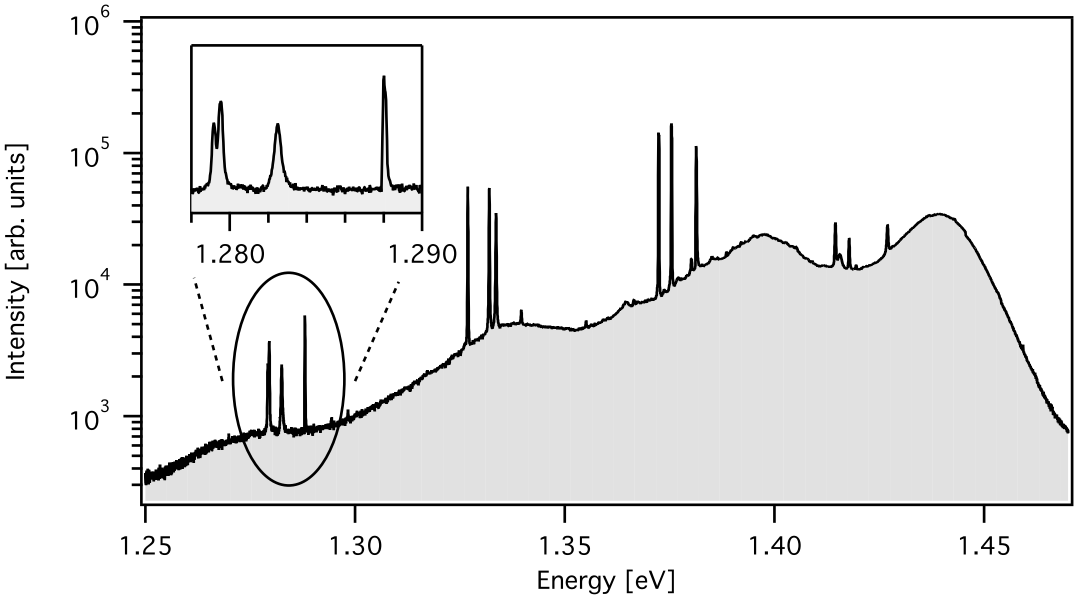

Figure 5.3: Micro-photoluminescence spectrum of a single microdisk. The photoluminescence intensity is plotted on a logarithmic scale against the emission energy. On top of a broad background signal of the quantum dots sharp peaks are visible. These are the whispering-gallery modes of the microdisk. The peaks are bunched into four groups. The inset shows a magnification of the first peak group.

non-resonant quantum dot emission. As explained in the previous section, the increasing background intensity has its origin in the characteristics of the micro-photoluminescence setup. In order to analyze the whispering-gallery modes, each peak in the spectrum was fitted with a Lorentz curves on a linear background. Although the line shapes of whispering-gallery modes are theoretically Lorentz curves, the fits do not match the peak shape very well in most cases. This effect may in some cases be due to whispering-gallery mode splitting. It occurs, when the splitting is so small that two peaks overlap and form a single peak with a peculiar shape. These peaks were better fitted with two Lorentz functions. But since the splitting is so small and we are now only interested in the energetic position of the whispering-gallery modes, we treated those double peaks as a single peak. In other cases, the whispering-gallery mode has a thin rectangular shape which could not be easily fitted with two Lorentz functions. Here, the width of a whispering-gallery mode might be smaller than the image of the slit. In other words, the energetic resolution comes to its limits. All fits do, however, give the correct energetic position of the peaks which we are interested in for further investigation.

The peaks are bunched into four groups of peaks with four to six whispering-gallery modes in each group. We can take advantage of the grouping to identify the whispering-gallery modes and to determine the radius of the investigated microdisk by matching the group pattern with the calculated whispering-gallery modes. A whispering-gallery mode calculation is shown in figure 5.4. Here, the energetic whispering-gallery mode positions are plotted against the radius of a microdisk. The plot shows the calculated energetic whispering-gallery mode position for the radial mode numbers $l = 1$ and $l = 2$, each in TE and TM polarization. The radius variation for the calculated whispering-gallery modes ranges from $R = 0.75\,\mu\mathrm{m}$ to $R = 1.5\,\mu\mathrm{m}$ in 200 steps. The calculation covers azimuthal mode numbers from $m = 4$ to $m = 39$. By taking a cross section in the plot for a given radius, one obtains the calculated energetic whispering-gallery mode positions for a specific microdisk. This is shown exemplarily for the microdisk b2d4 as a black horizontal line in figure 5.4. The two parallel, dotted lines indicate the $\pm 30\,\mathrm{nm}$ error of the radius determination. Naturally, the energetic position of whispering-gallery modes increases with the azimuthal mode number m. For each whispering-gallery mode with a certain m, the energetic position decreases with increasing radius. The gradient of a line with a small m is high and decreases with higher m. These general tendencies can be observed in each mode group. Lines within one mode group do not cross each other. Lines of different mode groups do cross due to their different gradients. This leads to a Moiré-like mode pattern observable in figure 5.4. There are darker regions in the image, where the mode line spacing is almost equally distributed and there are lighter regions where the mode lines bunch together. If the calculated mode positions match measured mode positions, it might be possible to use this patterns as an identification criterium. The advantage of this determination method is that spectra may be matched regardless of their exact energetic positions. As we shall see later, an energetic shift of the spectra occurs quite easily, while the relative mode position remains comparably constant.

Figure 5.5 is a comparison between a calculated and measured spectrum of the microdisk b2d4. Figure 5.5 (a) shows a plot of Lorentz curves compiled using the fit results.

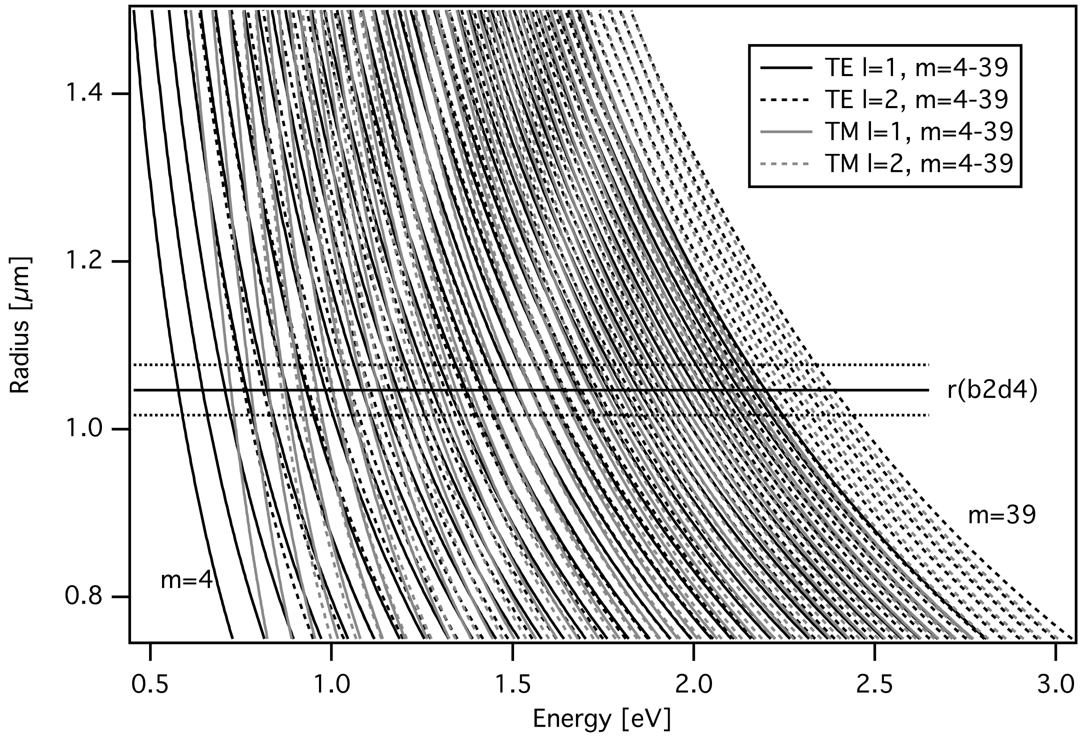

Figure 5.4: Calculated energetic position of whispering-gallery modes for microdisks with varying radius. The mode groups with the radial mode numbers $l = 1$ and $l = 2$ for the two polarizations TM and TE are shown. For each mode group the lines of the azimuthal mode numbers $m = 4$ to $m = 39$ are displayed. The radius ranges from $R = 0.75\,\mu\text{m}$ to $R = 1.5\,\mu\text{m}$. The horizontal solid black lines mark the radius of the microdisk b2d4 obtained by evaluation of the SEM image in figure 5.2 (b). The horizontal dotted lines mark the error $\pm 30\,\text{nm}$ of the evaluated radius.

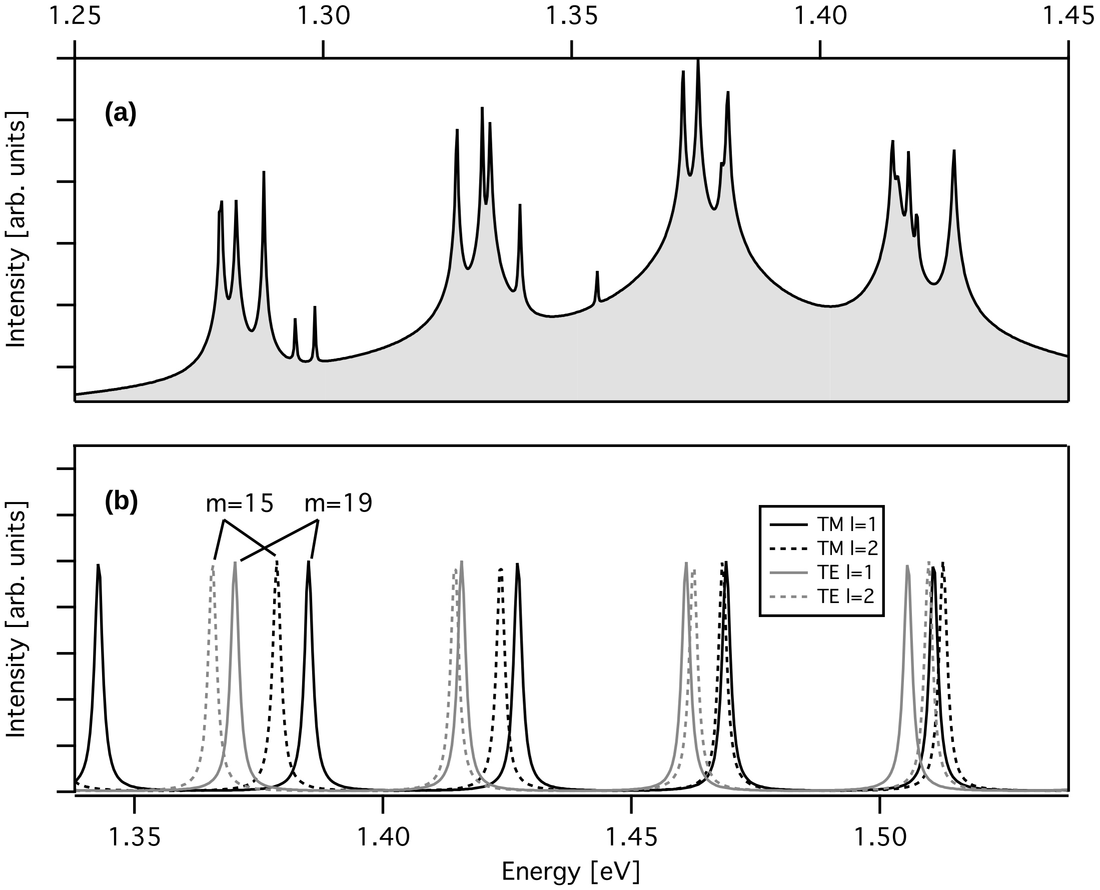

Figure 5.5: Comparison of an experimentally obtained spectrum and calculated whispering-gallery modes. (a) experimentally determined photoluminescence intensity plotted logarithmically versus energy. The graph shows fitted Lorentz curves from a spectrum of microdisk b2d4. The original spectrum is shown in figure 5.3. (b) calculated mode spectrum for a microdisk with a radius of $R = 1.047\,\mu\text{m}$. The width and height of the peaks are chosen arbitrarily to visualize the modes and do not contain physical information. The solid lines depict the whispering-gallery modes with $l = 1$, the dashed lines $l = 2$. Note that the calculated spectrum is shifted relative to the measured spectrum above. With this energetic shift, the spectra display similar mode patterns.

Figure 5.5 (b) is a plot of Lorentz curves at the positions obtained from the calculation for a microdisk with a radius of $R = 1.047\,\mu\text{m}$. Note that the energy axis of figure 5.5 (b) is shifted with respect to figure 5.5 (a) by 88 meV. With this shift the mode distribution of the calculated spectrum resembles the mode distribution in the measured mode spectrum with the bunched modes. In figure 5.5 (b), width and intensity of the peaks were chosen arbitrarily to resemble a peak shape and they do not reflect any calculated properties except in their positions.

According to the calculated spectrum, the experimentally observed modes in the group between 1.35 eV and 1.40 eV can be determined as $m = 19$ for the TE and TM modes with $l = 1$, and $m = 15$ for the TE and TM modes with $l = 2$. At each energetically subsequent group both azimuthal and radial mode numbers rise by one. The mode pattern in the spectrum and the calculation does generally fit quite well. However, looking at the exact mode positions and the number of modes in a mode group reveals significant deviations between the calculated and the measured spectra. We suppose that two factors might be crucial for these deviations. The calculated spectrum only accounts for the radial mode numbers $l = 1$ and $l = 2$ since their peak intensity should be dominant to higher mode numbers. This could of course easily lead to a different number of observed modes in the experiment compared to the calculation. Furthermore, the determination of the microdisks radius of the SEM image is quite vague. Thus, if the calculation was carried out for a different radius, the pattern, as well as the energy shift, would be different. We therefore shall now demonstrate the same allocation principle for different radii.

Figure 5.6 shows alternative mode allocations. The plot is basically a close-up of the calculated whispering-gallery modes shown in figure 5.4. The green box illustrates the energetic region of the measured spectrum in figure 5.5 (a), the blue box the energetic region of the calculated spectrum in figure 5.5 (b). The red triangles on the 1047 nm line mark the positions of the measured whispering-gallery modes. The lines with black diamonds denoted as a,b and c in figure 5.6, show the same measured spectrum shifted in energy and radius to match the underlying calculated spectra. Spectrum b at $R = 1.047\,\mu\text{m}$ is shifted only in energy by $\Delta E = 88\,\text{meV}$ with respect to the measured spectrum. This corresponds to the mode allocation example discussed above. There are two alternative mode allocations: spectrum a at $R = 1.020\,\mu\text{m}$ and spectrum c at $R = 1.070\,\mu\text{m}$. The spectrum a is shifted by $\Delta E = 70\,\text{meV}$ with respect to the measured spectrum and leads to smaller azimuthal mode numbers compared to spectrum b. Spectrum c is shifted by $\Delta E = 110\,\text{meV}$ and leads to higher azimuthal mode numbers compared to spectrum b. None of the spectra fits perfectly and all the spectra have to be shifted to higher energies to match the pattern of the calculated whispering-gallery modes which again shows the difficulty of an exact mode allocation.

We will briefly present the idea of another method to match the experimentally observed mode spectrum with the calculated mode spectrum. Instead of looking at the energetic positions of the whispering-gallery modes, the mode spacings for whispering-gallery modes with the same radial mode numbers can be examined. Figure 5.7 shows the calculated energetic difference between adjacent azimuthal mode numbers for the TE and TM polarization with the radial mode number $l = 1$ and $l = 2$. On the abscissa we find

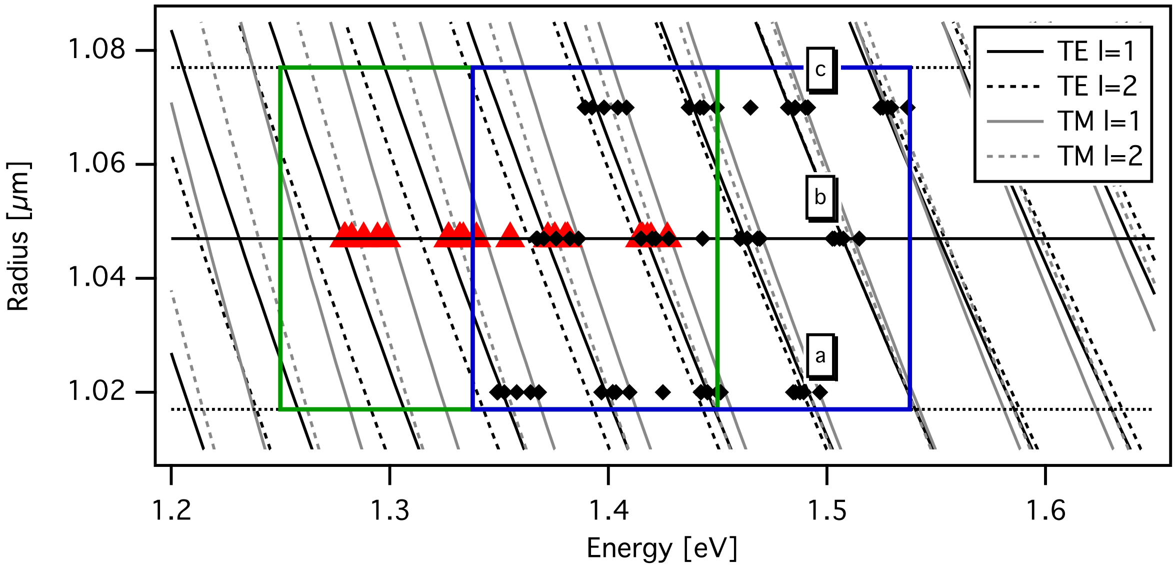

Figure 5.6: Whispering-gallery mode allocation. The underlying plot is basically a close-up of figure 5.4. The red triangles depict the original energetic position of the measured whispering-gallery modes. The green and blue boxes mark the energetic regions of figures 5.5 (a) and (b), respectively. The original spectrum is shifted in energy and radius to three different positions to match the underlying mode pattern. This is illustrated by black diamonds in the plot.

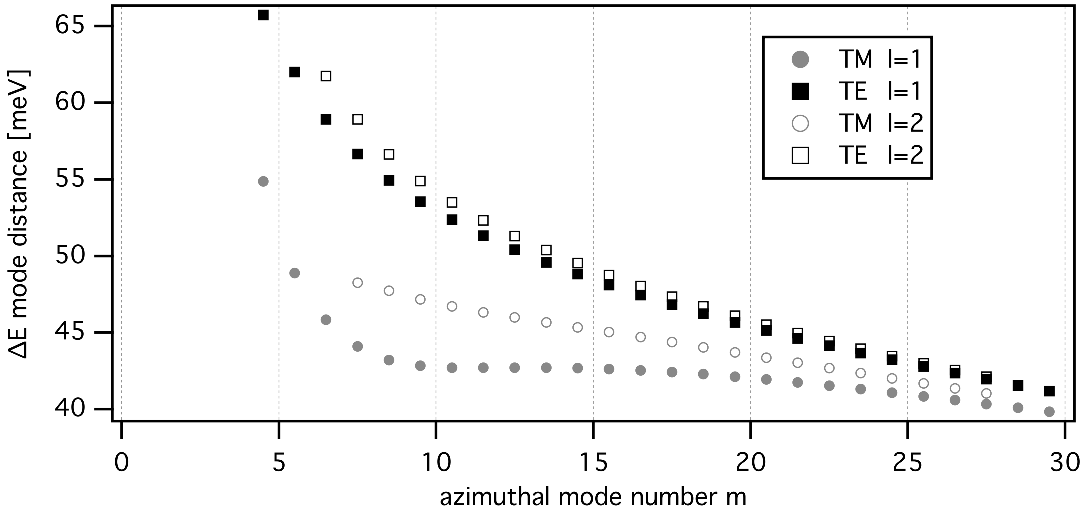

Figure 5.7: Calculated mode spacing for a microdisk with $R = 1.047\,\mu\text{m}$ in TE and TM polarization with the radial mode numbers $l = 1$ and $l = 2$. On the abscissa, the azimuthal mode number m is shown. The ordinate gives the mode spacing. The data points are situated between integer mode numbers to indicate which difference was determined. Each mode family has a distinctive mode spacing which could possibly be used to determine the mode numbers in an experiment.

the azimuthal mode numbers m. The ordinate gives the energetic difference. The data points are situated between integer mode numbers to indicate to which mode numbers the calculated difference belongs. Each mode family has a distinctive distance variation between adjacent azimuthal mode numbers. The calculations become erroneous for low azimuthal mode numbers and are hence not shown in figure 5.7. It should be possible to use this variation to pinpoint mode numbers in an experiment.

We conclude that these pattern matching methods should be seen as a new concept for whispering-gallery mode allocation. There are numerous difficulties with these methods which make the accurate allocation of whispering-gallery modes challenging. Maybe the most crucial part is finding the correct theoretical model for the mode calculation. As we shall see in the next chapter, the underlying optical dispersion of the semiconductor material has a great impact on both the absolute and relative energetic whispering-gallery mode position. In our specific case, the imprecise radius determination makes an allocation even more difficult. Nonetheless, if the optical dispersion is well known and the measured spectrum covers a broad energetic range, these methods might be helpful for mode allocation.

5.3 Microdisks of nominally the same size

As shown in figure 5.2 (a), each subset of microdisks contains 16 microdisks with nominally the same size. This means, that all microdisks in one subset are prepared with the identical process parameters. This section quantifies the irregularities that occur as a result of the wet etching process or the mask creation with the SEM. We investigated 15 microdisks in the subset c2 to quantify the tolerances of the fabrication process. Figure 5.8 shows the photoluminescence spectra of this experiment on a logarithmic scale. The spectra are normalized with respect the wetting layer peak at 1.44 eV. At a first glance, the similarity of the spectra stands out. This means, that the spectra are quite well reproduced in terms of number and position of the existing modes. The whispering-gallery modes again bunch together to four distinctive mode groups. We deduce from the analysis in the last section, that each group contains whispering-gallery modes with different radial mode numbers or polarizations. Each subsequent group contains the same modes with azimuthal mode number m raised by one. We can see furthermore that the spectra are shifted with respect to one another. In order to quantify the variances in the spectra each peak in each spectrum is fitted with a Lorentz curve. The hereby obtained mode positions are plotted in figure 5.9 (a) for each microdisk. In figure 5.9 (c) each spectrum is shifted by a certain amount plotted in figure 5.9 (b). The shift amount is chosen in such a way, that the first peak of the second group in each spectrum has the same energy. This enables us to compare the deviation of the mode spacing and the shift between the spectra directly. The spectral shift amount in figure 5.9 (b) varies randomly and lies within a 10 meV range. Figure 5.9 (c) shows that the mode spacings vary as well for each spectrum. From the energetically lowest peak of each group (except the second group) in figure 5.9 (c) we find that the peak position varies randomly within 1.6 meV. This

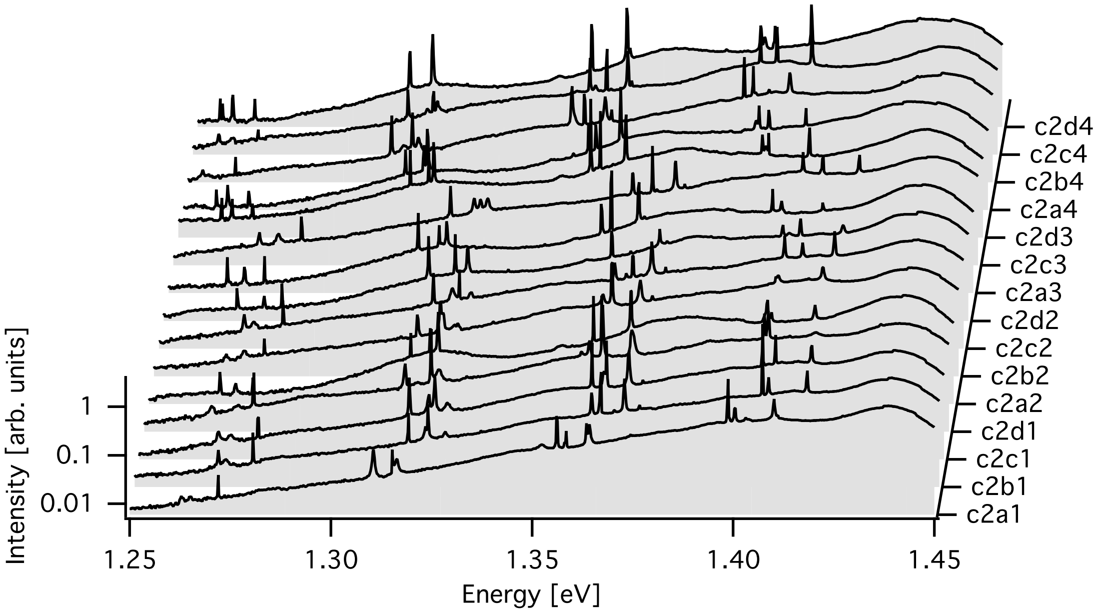

Figure 5.8: Waterfall plot of the experimentally measured spectra of microdisks with a nominally fixed radius. The intensity is plotted on a logarithmic scale.

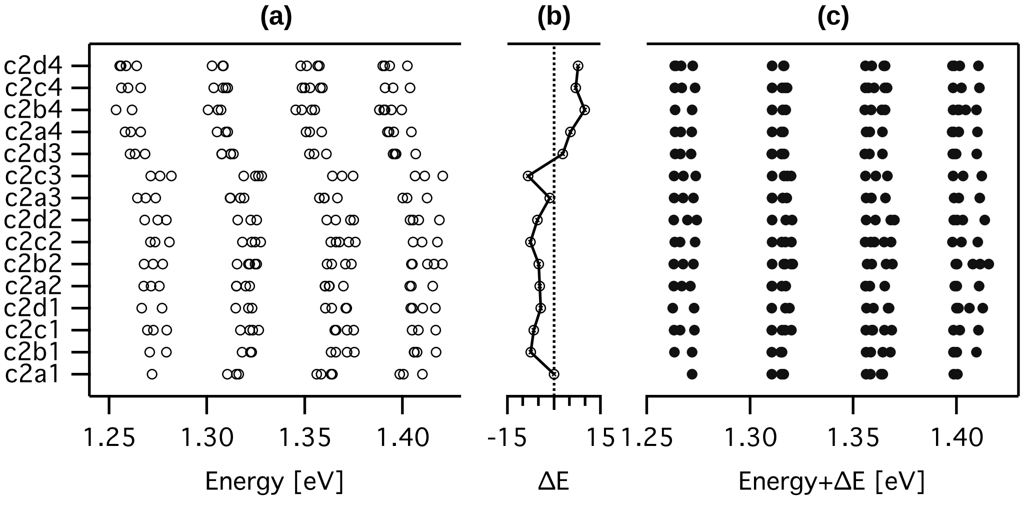

Figure 5.9: (a) Photoluminescence spectra of microdisks with nominally the same size. A mode bunching is clearly observable. Shifting each microdisk spectrum by a certain amount depicted in (b) leads to the plot (c). The shift amount is chosen to energetically match the first whispering-gallery mode of the second mode group of each microdisk.

is the variation within one group of radial mode numbers. The other peaks within one mode group vary randomly in a 5 meV range. This is the variation in between modes with different radial mode numbers or different polarizations. This directly shows the limits of the fabrication process. For microdisks with identical preparation parameters, we expect a variation in the energetic position of the whole spectrum up to 10 meV and a variation of the mode spacings up to 5 meV.

In the next chapter, we investigate the limits of the preparation process with different methods and in much more detail. Despite the different sample structure the same limits apply because of the same preparation technique.

5.4 Microdisks with different sizes

We now apply the pattern matching mode allocation method to microdisks with increasing radii. Basis for the mode identification is again the whispering-gallery mode calculation for varying radii shown in figure 5.4. With the knowledge about the limits of the fabrication process, we now have an error margin within which it is sensible to shift the spectra to make them fit to the underlying pattern.

The microdisks investigated in this experiment are the encircled ones in figure 5.2 (a). Gray arrows in figure 5.2 (a) illustrate the sorting order of the microdisks, starting from a1d4 with the smallest radius to e4c2 with the largest radius. The radii of the microdisks can be deduced from the SEM image of microdisk b2a1 and the predetermined radius increment of $\Delta R = 20\,\mathrm{nm}$ per subset in the wet etching mask. We thus deduce for the smallest microdisk a1d4 a radius of $R_{a1d4} = 0.948\,\mu\mathrm{m} \pm 0.030\,\mu\mathrm{m}$ and a radius of $R_{e4c2} = 1.328\,\mu\mathrm{m} \pm 0.030\,\mu\mathrm{m}$ for the largest microdisk e4c2.

The experimentally obtained spectra are depicted in figure 5.10 as a waterfall plot. The spectra are normalized with respect to the wetting layer peak. The intensity is plotted on a logarithmic scale and the spectra are sorted with respect to the microdisk size. In this plot, it is difficult to observe a mode distribution pattern.

In order to analyze the mode distribution and to compare the measurement with calculations, all peaks of each spectrum were fitted with Lorentz functions. As explained before, the shapes of the observed whispering-gallery modes differ from a Lorentz curve, but nonetheless we obtain valid positions for the whispering-gallery modes. Figure 5.11 shows the experimentally obtained mode positions as black dots on an energy axis. The left ordinate points to the according microdisk, again sorted by increasing size from bottom to top. The underlying lines are calculated energetic whispering-gallery mode positions for a certain radius range. These lines are a close-up section of figure 5.4 and show the radial mode number $l = 1$ and $l = 2$ for both TE and TM polarization. The according radius for the calculated spectra is given by the right ordinate.

In this graph, the experimentally obtained whispering-gallery modes do form an obviously visible pattern. Furthermore, this pattern resembles the underlying calculated whispering-gallery modes. In the lower left corner and the upper right corner of the plot the whispering-gallery modes seem to be more evenly distributed. In the middle

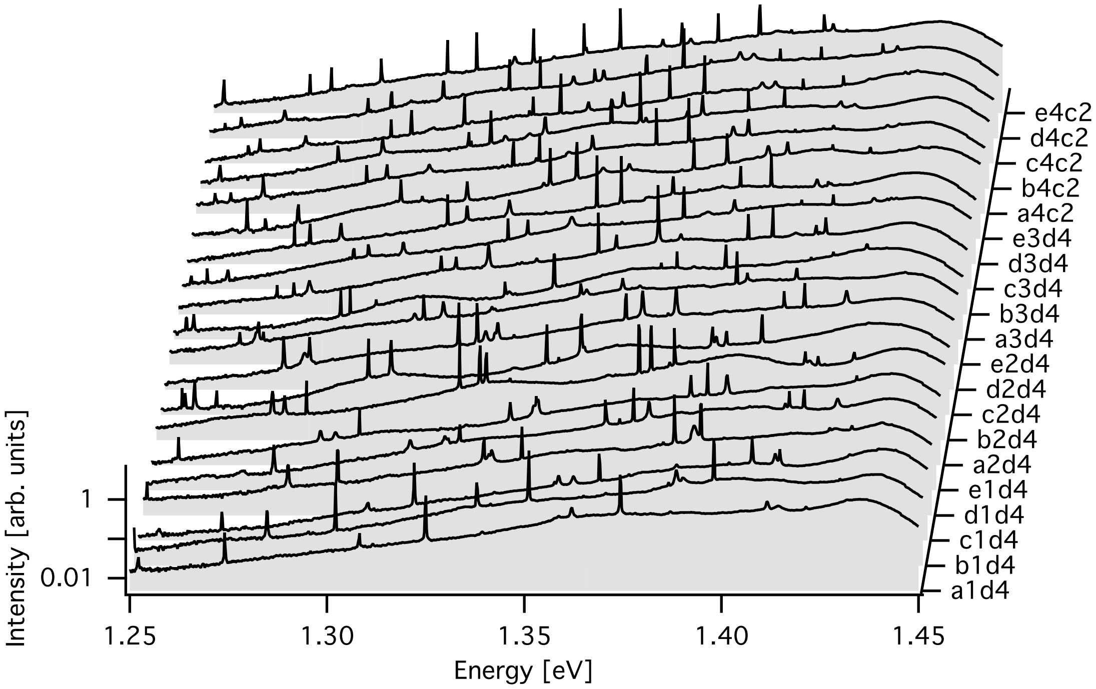

Figure 5.10: Waterfall plot of the experimentally measured spectra of microdisks with an increasing radius. The intensity is plotted on a logarithmic scale. The microdisk a1d4 has the smallest radius. The radius is increasing according to the order shown in figure 5.2 (a) to the microdisk e4c2.

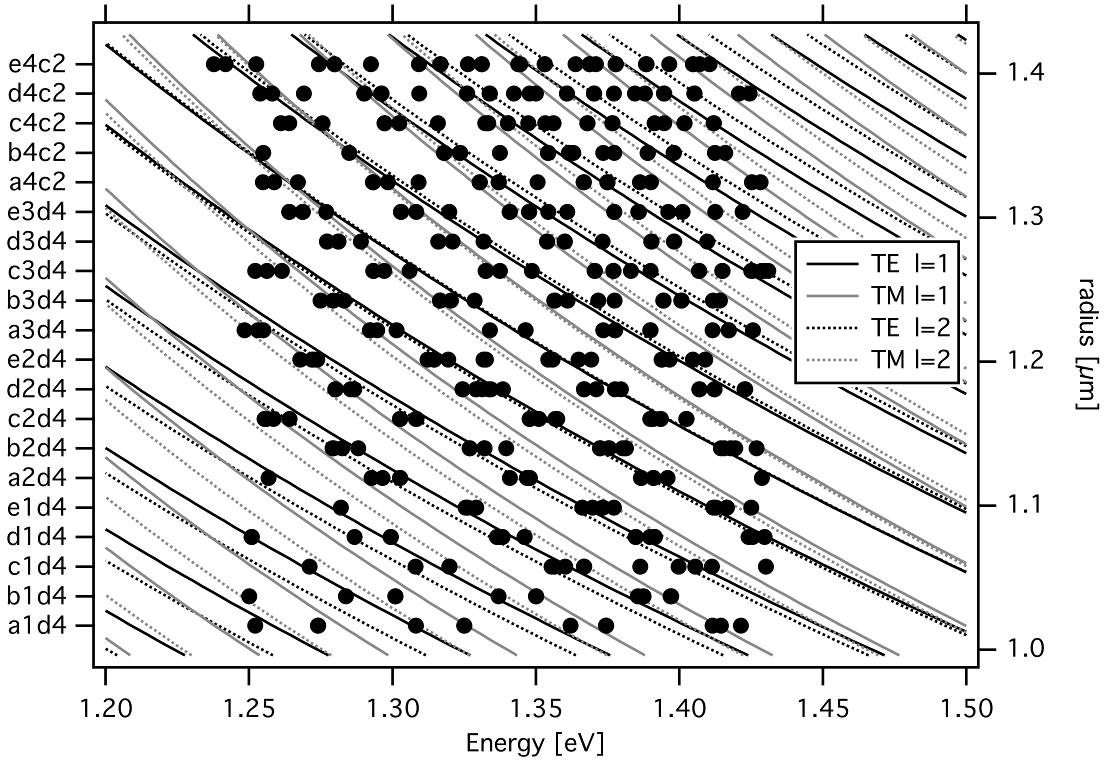

Figure 5.11: The black dots depict the mode positions of experimentally obtained whispering-gallery modes for microdisks with varying radii. The lines below the circles were obtained by calculation and are an extraction of figure 5.4. The experimentally obtained modes exhibit a similar Moiré-like pattern as the calculated mode lines.

part, on descending lines from the upper left to the lower right corner, the whispering-gallery modes bunch together. This is true for both the experimentally obtained and the calculated whispering-gallery modes. The slope of the calculated whispering-gallery mode lines tends to coincide with the experimentally obtained whispering-gallery modes for most parts of the plot. The latter phenomenon is due to an adjustment of the left and right ordinate. The predetermined radius increase per microdisk of $\Delta R = 20\,\text{nm}$ leads to a total radius difference from the smallest to the largest microdisk of 380 nm starting from the microdisk a1d4 with a radius of $R_{a1d4} = 0.948\,\mu\text{m} \pm 0.030\,\mu\text{m}$. The ordinate of the calculated whispering-gallery mode lines on the other hand spans over a total radius difference of 431 nm starting from the microdisk a1d4 with a radius of $R_{a1d4} = 0.996\,\mu\text{m}$ to the largest microdisk e4c2 with a radius of $R_{e4c2} = 1.427\,\mu\text{m}$. The radius increment per disk would thus be $\Delta R = 21.55\,\text{nm}$. With this adjustment, the slope of the calculated mode lines is altered to fit the experimentally obtained whispering-gallery mode positions. This adjustment would be justifiable for a small radius variation, but the huge total difference is not explicable with the above mentioned error of $\pm 30\,\text{nm}$. Unfortunately, without knowledge of the exact microdisk radii we are not able to decide, whether the calculation was based on incorrect parameters or the predetermined radius variation does not match the real radius variation. Due to this uncertainties we forgo the attempt to make the calculated and experimentally obtained spectra match by energetically shifting whispering-gallery modes. We rather point out that the similarity of the calculated and experimentally obtained spectra indicate the feasibility of this mode allocation method.

This experiment should again be viewed as a new concept for mode allocation based on mode pattern matching for microdisks with different radii. Together with the error margin measurement shown above, this method might be one way to identify whispering-gallery modes in larger arrays of microdisks with different radii.

6 Pierced microdisks

Due to the rotational symmetry, the photoluminescence light emitted by ordinary microdisks is isotropically distributed in the ρ-φ plane (cf. section 2.4.1). In a theoretical work Wiersig and Hentschel [11] showed that this emission behavior can partially be modified without destroying the high Q factor by piercing a microdisk (cf. section 2.4.2). We fabricated and investigated pierced microdisks in order to study the rich physics that is involved with such structures. This chapter presents the results of the experiments performed on these pierced microdisks. In the first section we will introduce the sample design and present the results of the fabrication process with respect to the geometrical parameters of the microdisk. The second section deals with the whispering-gallery mode allocation based on the theoretical model presented in chapter 2 and FDTD simulations. In the third section we investigate the spatial emission behavior of pierced microdisks with respect to the ρ-φ plane for the radial mode numbers $l = 1$ to $l = 4$. The last section of this chapter deals with the Q factor and the lasing capabilities of the pierced microdisks.

6.1 The sample design

Our sample design of pierced microdisks has generally two goals: (i) to generate and (ii) to detect unidirectional photoluminescence emission of the microdisks. The generation of unidirectional emission is realized by fabricating microdisks with a geometrical hole as described in section 2.4.2. The influence of the hole on the whispering-gallery modes and the subsequent generation of unidirectional emission will be the subject of later sections in this chapter. We will first describe the sample design with respect to the detection of unidirectional photoluminescence emission.

The far-field emission of a microdisk is observed within a hollow cone-shaped volume, which has a large opening angle θ and a small emission angle α with respect to the ρ-φ plane of the system (cf. section 2.4.2). To collect the highest emission intensity we would have to place the detector in the emission direction. Since our setup has one fixed detector, we would have to rotate the microdisk in order to detect the emission intensity in dependence of the rotation angle. This approach cannot be implemented in our experimental setup, since the microdisk is not rotatable in the cryostat. A different approach is to detect the near-field emission of the microdisk in the ρ-φ plane. Since we cannot place the detector in the near-field range of a microdisk we realized this approach by fabricating a surrounding semiconductor wall-like structure around each microdisk as shown in figure 6.1. The near-field photoluminescence light of the microdisk scatters

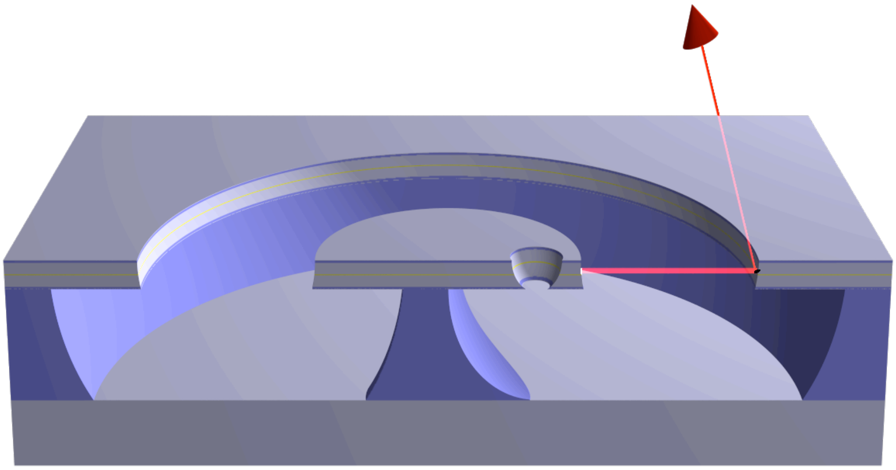

Figure 6.1: Cross-section of a microdisk with its surrounding wall. The photoluminescence light of the microdisk is scattered at the surrounding wall due to surface roughness. The light scattered in the direction of the microscope objective is detected.

at the surrounding wall in all directions due to surface roughness. thus, we can detect the light scattered into the direction of the microscope objective and compose a spatially and energetically resolved emission image of both the microdisk and its surrounding wall using the method explained in chapter 3. We are able to spatially analyze the spectrally resolved near field emission behavior of a microdisk in the ρ-φ plane. In comparison with a direct measurement of the far-field emission the photoluminescence signal is presumably very weak, but because of the very high emission intensities of our microdisks, we are able to gain sufficient intensities with this setup.

All investigated microdisks are located on one sample, which we will refer to as sample B[1]. The $4\,\text{mm} \times 4\,\text{mm}$ sample contains hundreds of pierced microdisks with different disk parameters. Before we describe the sample design we shall give an overview of these disk parameters. A SEM image of a pierced microdisk with its characterizing parameters is shown in figure 6.2. As will be explained in detail below, the pierced microdisks exhibit a slightly elliptical shape instead of being circular, as aimed for in the sample design. The semimajor axis a and the semiminor axis b of the ellipsis always point in the same direction on the sample. The average eccentricity $e = \sqrt{a^2 - b^2}/a$ of the ellipsis is[2] $e = 0.305 \pm 0.015$. As mentioned in chapter 4, the shape of the hole resembles an imprint of a sphere on the microdisk's surface as visible in figure 6.1. Thus, the edges of the hole are less steep compared to the outer edges of the microdisk. Due to this geometry we cannot easily specify the radius of the hole. We instead approximated a mean hole radius by measuring the outer R_{h_o} and the inner radius R_{h_i} of the hole with $R_h = (R_{h_o} + R_{h_i})/2$. The outer hole radius R_{h_o} is the radius of the hole on the upper side of the microdisk whereas R_{h_i} is the radius on the side which faces the substrate. The

---

[1] Sample B is taken from near the center of a wafer #1855. The sample has the internal number 1855-14

[2] The error is given by the standard deviation $\sigma = \sqrt{\frac{1}{N-1}\sum(x_i - \bar{x})^2}$

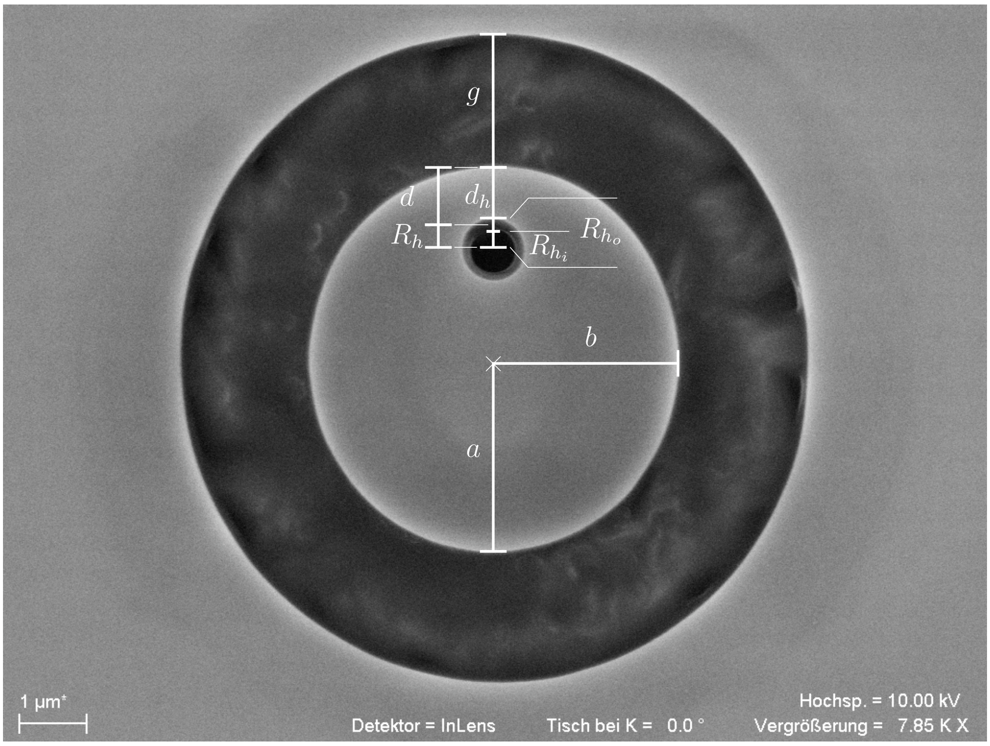

Figure 6.2: Example SEM image of a pierced microdisk together with its characterizing parameters. Similar SEM images were used to determine the geometry of all investigated microdisks. An analysis of these parameters provides information about the preparation process and guide values for the theoretical calculation of whispering-gallery modes.

mean radius R_h is thus approximately the radius in the center in z direction of the slab. We use this approximation because we only excite whispering-gallery modes with the vertical mode number $p = 1$ where the field maximum is centered in the z direction of the slab. For all further calculations and comparisons, we use the mean hole radius R_h. The parameter d_h denotes the distance from the microdisk edge to the outer diameter of the hole. We use $d = d_h + (R_{h_o} - R_{h_i})/2$ as distance of the hole to the outer microdisk edge according to the mean hole radius r_h. Finally, the parameter g denotes the gap between the microdisk and the surrounding wall.

Sample B contains two fields with the same layout for redundancy reasons. Only parts of one of the fields were investigated due to the large number of microdisks and limited time. A microscopic image of the investigated field is shown in figure 6.3. The field contains 146 microdisks divided into four sections a1, b1, c1 and d1. These sections differ in the orientation of the hole position, indicated by a white microdisk icon above each section, and in the hole radius R_h. Within each section, microdisks in a row nominally have the same disk parameters. The topmost row with the label '0' consists of microdisks without a geometrical hole. All other microdisks exhibit a hole and their parameter is decreasing row-wise from bottom to top. Nominally, the sections a1 and b1 have a certain hole radius R_{h_1} and the sections c1 and d1 have a slightly larger hole radius R_{h_2}. We

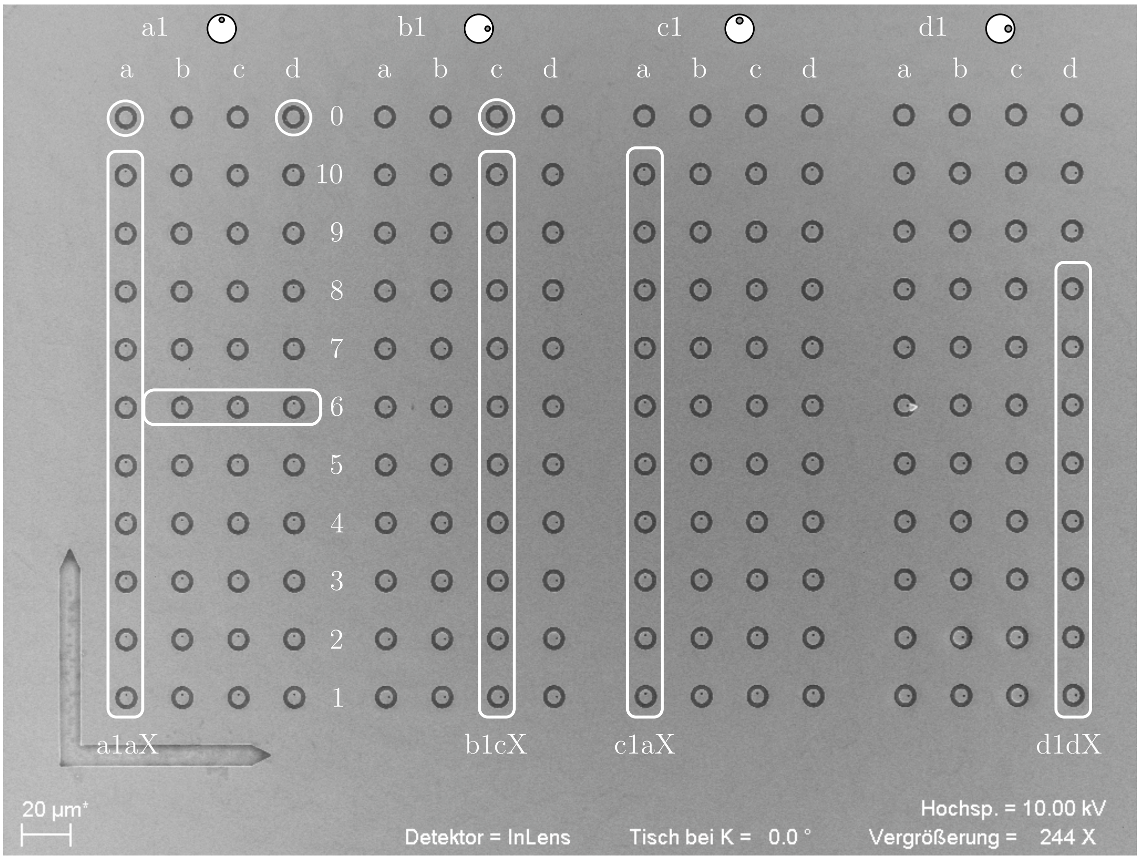

Figure 6.3: Microscopic image of the sample design for pierced microdisks. The encircled microdisks where investigated in this work. Generally, the sample is divided into four blocks. The blocks differ in the orientation of the hole and the hole size. The distance d from the hole to the microdisk edge varies vertically from microdisk to microdisk, whereas horizontally aligned microdisks within a block have the nominally same parameters. The top row with label '0' contains microdisks without a geometrical hole. The microdisk a1a7 is shown in figure 6.2.

parameter	etching mask	target value
R [nm]	3250	2750
R_{h_1} [nm]	105	605
R_{h_2} [nm]	132.5	632.5
d_{min} [nm]	1385	385
d_{max} [nm]	1935	935
Δd [nm]	61	61
d_{min}/R	0.426	**0.14**
d_{max}/R	0.595	**0.34**

Table 6.1: Etching mask parameters. Based on the by Jan Wiersig theoretically determined value $d/R = 0.24$ we designed the photoresist etching mask to vary around this parameter within ±0.1 after deep etching 500 nm. We wanted the microdisk to have a radius of $R = 2.75\,\mu\text{m}$ after etching as a compromise between stability and small size. All other parameters followed from these two assumptions.

will later analyze the actual hole sizes and compare them to the planned layout.

The encircled microdisks in figure 6.3 were investigated with a SEM. There are four columns of encircled microdisks with varying parameter d. We call these groups of microdisks according to their positions: a1aX, b1cX, c1aX and d1dX. Furthermore, there is one group of microdisks with the nominally same parameters (a1a6,. . . ,a1d6) and three microdisks without a geometrical hole.

Now we compare the intended microdisk parameters with those determined by analyzing the SEM images. The etching mask is designed to provide good microdisk parameters for an etching depth of 500 nm. Since the etching is in first approximation isotropic, deep etching results also in a lateral etching of the same amount. We thus calculated the parameters of the etching mask with a set of given target values. The initial parameters of the etching mask are given in table 6.1 together with the target values after the etching process we aimed at. We used the size independent parameter d/R from a calculation of Jan Wiersig to estimate our etching mask parameters. His calculations yield $d/R = 0.24$ for a microdisk with $R = 2.75\,\mu\text{m}$. We took these values as a basis and modeled the etching mask parameters to reproduce these values for an etching depth of 500 nm. We varied the hole distance to radius ratio d/R within ±0.1 around the target value. Note that we chose the distances d to be the same for both hole radii.

The actual results of the etching process are listed in table 6.2. There are some deviations from the predicted microdisk shape. First of all, we observe the aforementioned ellipticity for all microdisks. The mean value of the semiminor axis b is close to the targeted 2.75 µm, but the mean value of the semimajor axis a is ≈ 117 nm larger. Generally, this ellipticity could be caused by one or more of the three processes: (i) unequal x-y scaling of the SEM in the lithographic process, (ii) anisotropic acid flow during the HBr wet-etching step or (iii) unequal etching rates for different directions of the crystal lattice in the HBr wet etching step. We discard the first possibility, since a closer look at the values

parameter	a1aX	b1cX	c1aX	d1dX
$\bar{a}$ [nm]	2868 ± 13	2876 ± 14	2884 ± 9	2841 ± 9
$\bar{b}$ [nm]	2735 ± 14	2741 ± 10	2738 ± 9	2699 ± 8
$\overline{R_h}$ [nm]	381 ± 13	403 ± 10	452 ± 15	488 ± 12
$\Delta\bar{d}$ [nm]	67.6 ± 1.8	59.9 ± 1.4	63.7 ± 2.3	58.6 ± 3.2
$\bar{d}_{min}/\bar{a}$	**0.220**	0.203	**0.213**	0.206
$\bar{d}_{min}/\bar{b}$	0.231	**0.213**	0.224	**0.217**
$\bar{d}_{max}/\bar{a}$	**0.432**	0.387	**0.405**	–
$\bar{d}_{max}/\bar{b}$	0.453	**0.406**	0.427	–

Table 6.2: Mean microdisk parameters after etching. Most noticeable is the ellipticity of the microdisks. The hole radii are smaller than anticipated which results in higher d/a and d/b ratios. The d/a and d/b ratios are printed bold, if the hole is in line with the particular axis. Furthermore, the microdisks of the d1dX group are significantly smaller than the others in both a and b.

of the parameter d shows that d varies according to the orientation of the hole. The variation is of the same order of magnitude as the difference between the semimajor and semiminor axis. If the ellipticity was a result of the SEM lithographic process we would expect a smaller impact on the parameter d. We thus deduce that the HBr etching step is responsible for this deviation. We cannot rule out process (ii), but the direction of the axes being parallel to the (110) and $(1\bar{1}0)$ cleaved edges of the sample suggests that the HBr etching solution has one favored etching direction in which the etching rate is enhanced. We thus think that process (iii) is the main reason for the ellipticity of the microdisks.

We should mention that this ellipticity might as well occur in the ordinary microdisks of sample A. Unfortunately, the lack of SEM images for sampe A makes it impossible to verify or refute this finding for ordinary microdisks.

Furthermore, the etching rate in the hole is smaller than anticipated. This can be explained with reduced acid flow through the small hole in the etching mask as described in chapter 4. The reduced etching rate leads to generally smaller holes, which increases the d/R ratio. The ratios d/a and d/b in table 6.2 are printed bold, if the hole is located on the appropriate axis.

The measured disk parameters d, a, b, d/R and R_h are plotted in figure 6.4 against the vertical disk number. Solid symbols depict the groups a1aX and b1cX and the hollow symbols belong to the groups c1aX and d1dX. In plot (b), the black lines depict the values for a and b when the hole in line with the particular axis and gray lines depict the case when hole and axis are perpendicular. Note that we used a and b instead of R according to the hole position, since the microdisks have no explicit radius R.

From the average parameter values and the plots we can draw some conclusions: All microdisks are elliptical. The radius of the hole is smaller than anticipated. The hole radius increases from section a1 to section d1, although we anticipated the same radii

R_{h_1} for the section a1 and b1 and slightly larger radii R_{h_2} for c1 and d1. Nevertheless, we observe a gap between the radii R_{h_1} and R_{h_2} and the difference between these radii is much larger than expected. Overall, even the largest holes are smaller than originally planned. The microdisks in section d1 are significantly smaller than the others: both a and b are about 40 nm smaller compared to the microdisks in other sections. The envisaged ratio range d/R from 0.14 to 0.34 is exceeded by most microdisks and now lies between 0.2 and 0.4. The parameter variation within each group is low compared to the variation between the groups.

6.2 Mode allocation

The evaluation of the SEM images in the last section gave information about the disk parameters, which we can use as input parameters to our theoretical model for whispering-gallery mode calculation. In this and the following section we investigate the mode allocation and spatial emission behavior of the microdisks in the a1aX experiment.

We introduced a method for mode allocation in chapter 5, which is based on a pattern comparison between calculated and measured spectra for microdisks with increasing radii. We now have the situation that the outer microdisk geometry remains constant. Thus we try to find the parameters of one microdisk which calculate to a set of whispering-gallery modes that fit to the experimentally obtained spectra of all microdisks. We harness the fact that the different hole positions act in specific ways on the whispering-gallery mode distribution to confirm the calculated results. The influence of the hole on the whispering-gallery mode distribution will be discussed in detail in section 6.3. Here, we neglect this effect and calculate whispering-gallery modes that we will compare to the experimentally obtained photoluminescence spectra of the microdisks a1a5 and a1a7. These spectra are shown in figure 6.5 on a logarithmic scale. The SEM measurements reveal that the microdisks have an elliptical shape whereas the theoretical model assumes a circularly shaped microdisk with a radius R. We thus approximated the radius as follows: first, we calculated the circumference of an ellipsis with the axis a and b. We then deduced the radius R of a circle with the same circumference as the ellipsis. For the two microdisks a1a5 and a1a7 this method yields a radius of $R = 2.810\,\mu\text{m}$. We used this radius and a thickness of $H = 250\,\text{nm}$ to calculate whispering-gallery modes using the theoretical model presented in chapter 2. The calculation was performed with a customized $Al_xGa_{1-x}As$ dispersion:

$$n(E) = 3.436 + 0.33 \cdot (E(eV) - 1.1). \tag{6.1}$$

A discussion about the influence of the dispersion on the spectra can be found below in the subsection “$Al_xGa_{1-x}As$ dispersion”. The results of our calculations are plotted as dotted vertical lines in figure 6.1. We shifted the calculated whispering-gallery modes about 2.5 meV towards higher energies to match them with the underlying spectra. We now observe a very good agreement of the theoretically obtained TE whispering-gallery modes with the experimentally measured modes. Interestingly, the calculated TM modes

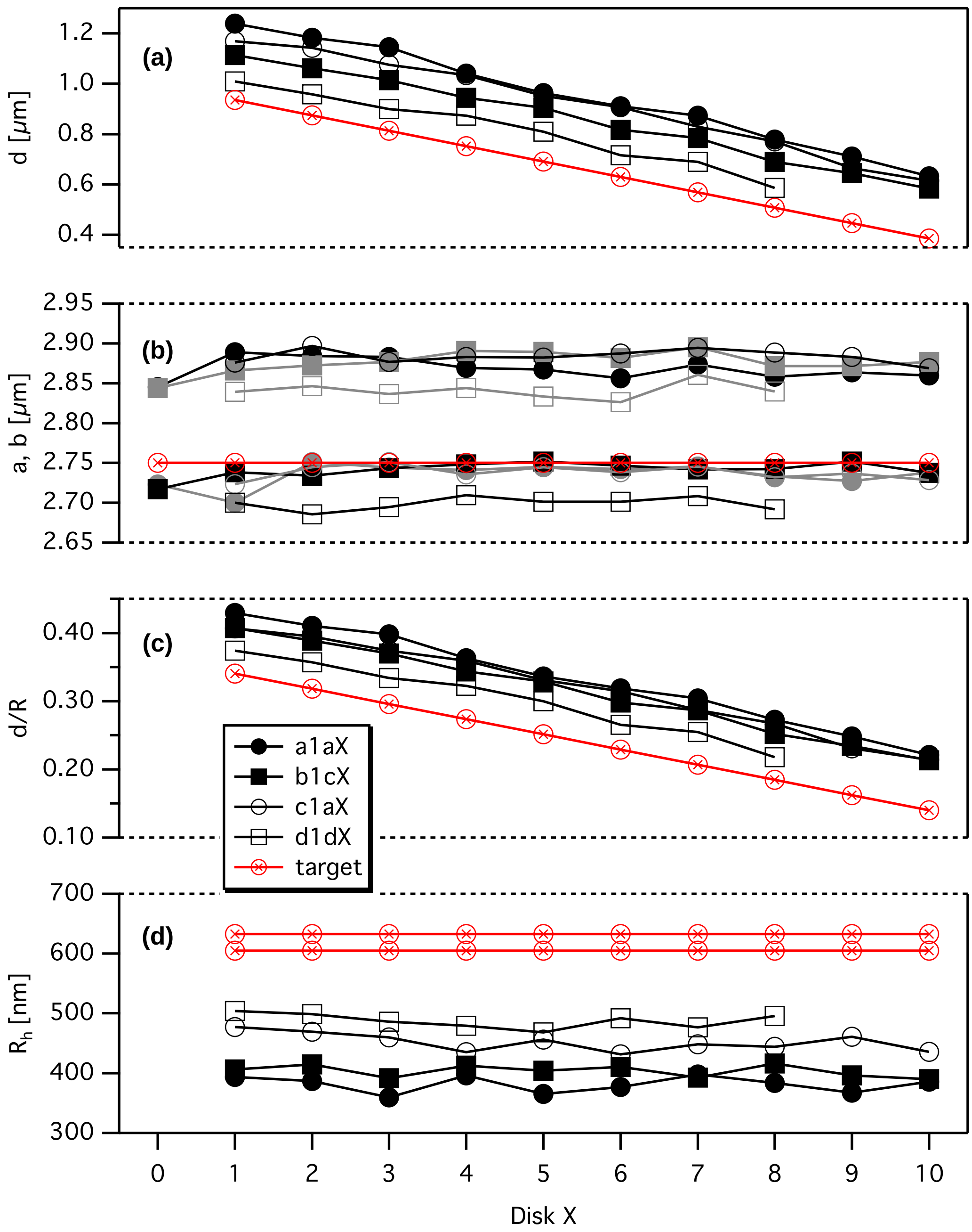

Figure 6.4: Pierced microdisk parameters versus disk number. Note that the experiment d1dX in (b) has overall smaller values compared to the other experiments. This, combined with the largest hole radius (d) affects the distance *d* in (a) and (c). The black lines in (b) correspond to the case when the axis is in line with the hole while the gray lines correspond to the case when hole position and axis are perpendicular.

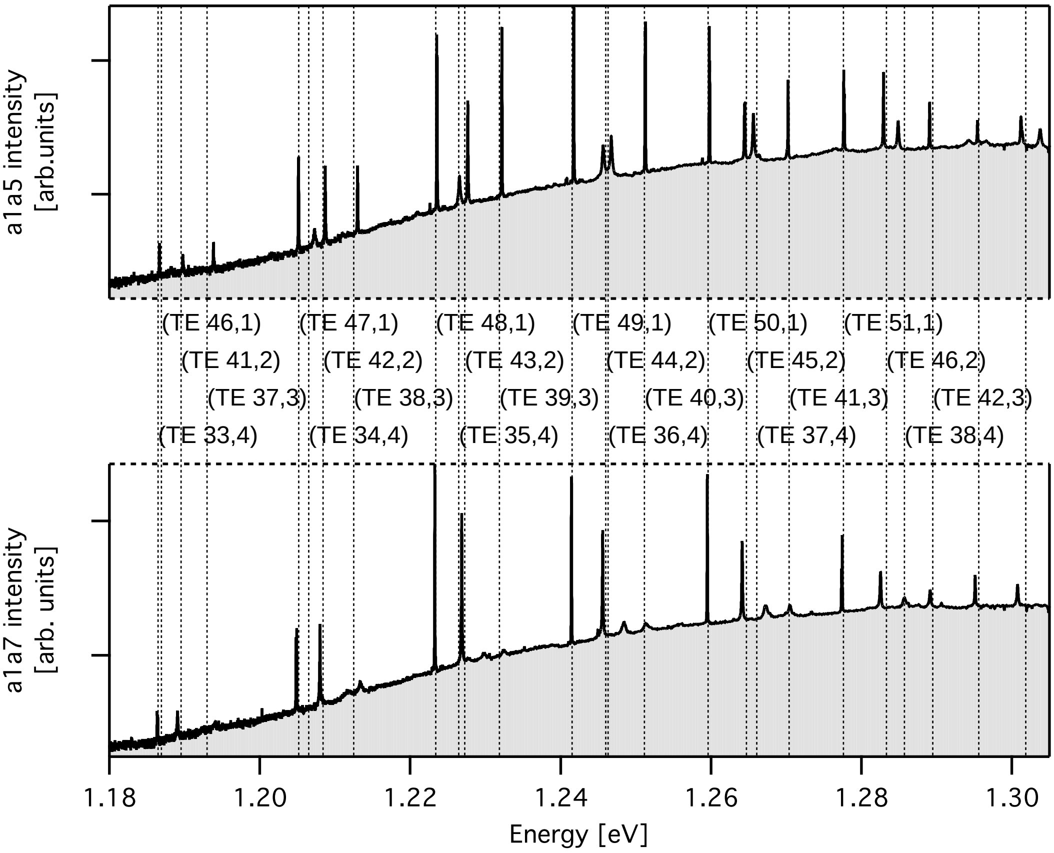

Figure 6.5: Exemplary photoluminescence intensity spectra of the microdisks a1a5 and a1a7. The vertical dotted lines depict the calculated TE whispering-gallery modes for a microdisk with $R = 2.810\,\mu\mathrm{m}$ and a thickness of $H = 250\,\mathrm{nm}$. The calculated whispering-gallery modes are shifted by 2.5 meV towards higher energies in order to match the spectra. The calculated TM modes failed to fit to the experimentally observed whispering-gallery modes. Obviously, their emission is much weaker in comparison to the TE modes and were thus left out of the plot.

do not fit in any of the experimentally obtained spectra. Their emission intensities seem to be much weaker compared to the TE modes. We therefore left the calculated TM modes out of the plot. The reason for the absence of TM modes is not quite known. The $l = 4$ whispering-gallery modes which are visible in the spectrum of the microdisk a1a5 do not occur in the spectrum of the microdisk a1a7 and the $l = 3$ whispering-gallery modes are strongly diminished. This effect can be explained by the influence of the hole on the whispering-gallery modes and will be discussed in detail below. We would like to point out that the mode allocation becomes increasingly vague for increasing radial mode numbers l. Small changes of the calculation parameters like the dispersion can lead to very different results regarding whispering-gallery mode distribution. The assignment of the radial mode numbers in these spectra is strongly supported by the discussion of the hole influence on the spectra in the following section.

$\mathbf{Al_xGa_{1-x}As}$ dispersion

The $Al_xGa_{1-x}As$ dispersion needs to be discussed in more detail. Once a theoretical model for the dispersion is found, it should ideally yield correct results for all microdisks with the same material parameters. On the other hand we observed that considerable differences in the whispering-gallery mode distribution can be induced by very small changes of the dispersion. We think that small local material changes on a wafer, like varying layer thicknesses, can be the source for changes of the refractive index. We thus took the approach to find a valid dispersion model for each sample by adapting appropriate parameters for the model. As a basis for the dispersion we always used the results of Pikhtin and Yas'kov [15] who measured the refractive index of $Al_xGa_{1-x}As$ for several x in an energy range of 0.5 eV and 2.5 eV. The dispersion curves are shown in figure 6.6. The influence of the dispersion on the whispering-gallery mode distribution can be approximated as follows: The gradient of the dispersion curve affects the distance of two neighboring whispering-gallery modes with the same radial mode number l. The offset of the dispersion curve basically shifts the hole whispering-gallery mode spectrum energetically. The effect of both parameters on the whispering-gallery mode spectrum is quite strong. In the comparably small energy range of the quantum-dot photoluminescence-emission we may assume a linear dependence of the dispersion

$$n(E) = A + B \cdot E(eV) \tag{6.2}$$

with the gradient B and the offset A. With these two parameters it is quite easy to match spectra of whispering-gallery modes with only one radial mode number l (e.g. $l = 1$). To model entire spectra with more than one mode number l on the other hand gets increasingly difficult for each additional radial mode number l. Our linear dispersion model, given in equation 6.1, beautifully coincides with the whispering-gallery modes observed in our spectra. Nonetheless, we tried to fit the data of Pikhtin and Yas'kov in a more complex way to our layer system by regarding each layer with its own refractive index. The result is a polynomial fit plotted as a black line in figure 6.6. Using this fit does not lead to satisfying results in the case of the experiment a1aX. The decision to use

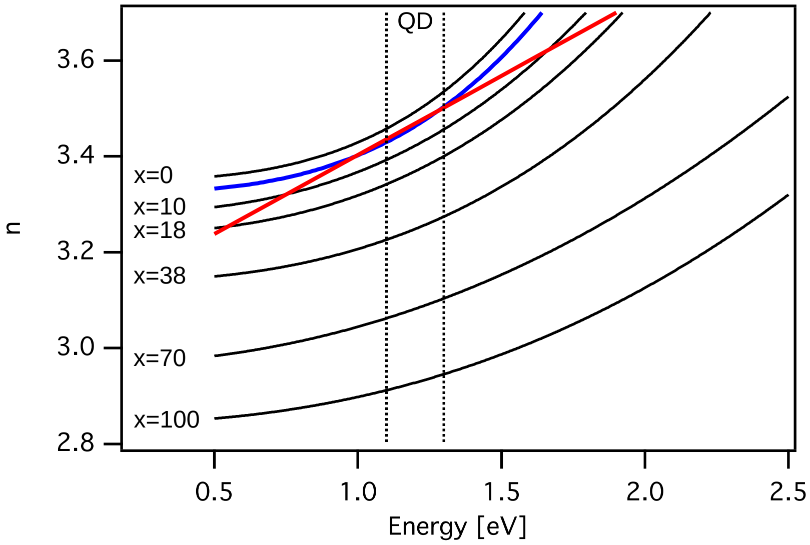

Figure 6.6: $Al_xGa_{1-x}As$ dispersion for several aluminum concentrations x according to Pikhtin and Yas'kov [15]. The black lines are polynomial fits to the data taken from their publication and converted to electronvolt. The blue curve is calculated from the fits with respect to the layer system of our microdisks. The red line depicts the linear dispersion approximation used in our calculations. The vertical dashed lines indicate the energetic range of the quantum-dot photoluminescence.

a linear dispersion was corroborated by the excellent coincidence of the whispering-gallery modes up to $l = 4$ and the support of the simulated spectra which will be presented in the next section. The linear dispersion used in the previous chapters was based on a similar approximation used by T. Kipp et al. [28]. The sensitivity of the whispering-gallery mode spectra to the dispersion makes the idea to allocate whispering-gallery modes solely on the theoretical model as introduced in chapter 5 look quite optimistic. The following sections show that the dispersion approximation we found for this sample yields results which are in good agreement to simulated spectra.

6.3 Influence of the hole position

In this section we analyze the influence of the distance d between the hole and the microdisk edge on the whispering-gallery mode spectrum. We shall first take a look at the theoretically determined field distributions. We calculated the field distributions of a microdisk with a radius of $R = 2.800\,\mu\text{m}$ and a thickness of $H = 250\,\text{nm}$ with the theoretical model presented in chapter 2. The radius R is again derived from elliptical microdisks with parameters a and b. Results of these calculations are plotted in figure 6.7. Here, the $\mathbf{H}$ and $\mathbf{E}$ field intensities for the TE and TM modes, respectively, are shown as gray scale plots against the radial position ρ and the azimuthal mode number m. Dark colors depict higher field intensities and light colors low field intensities. The vertical

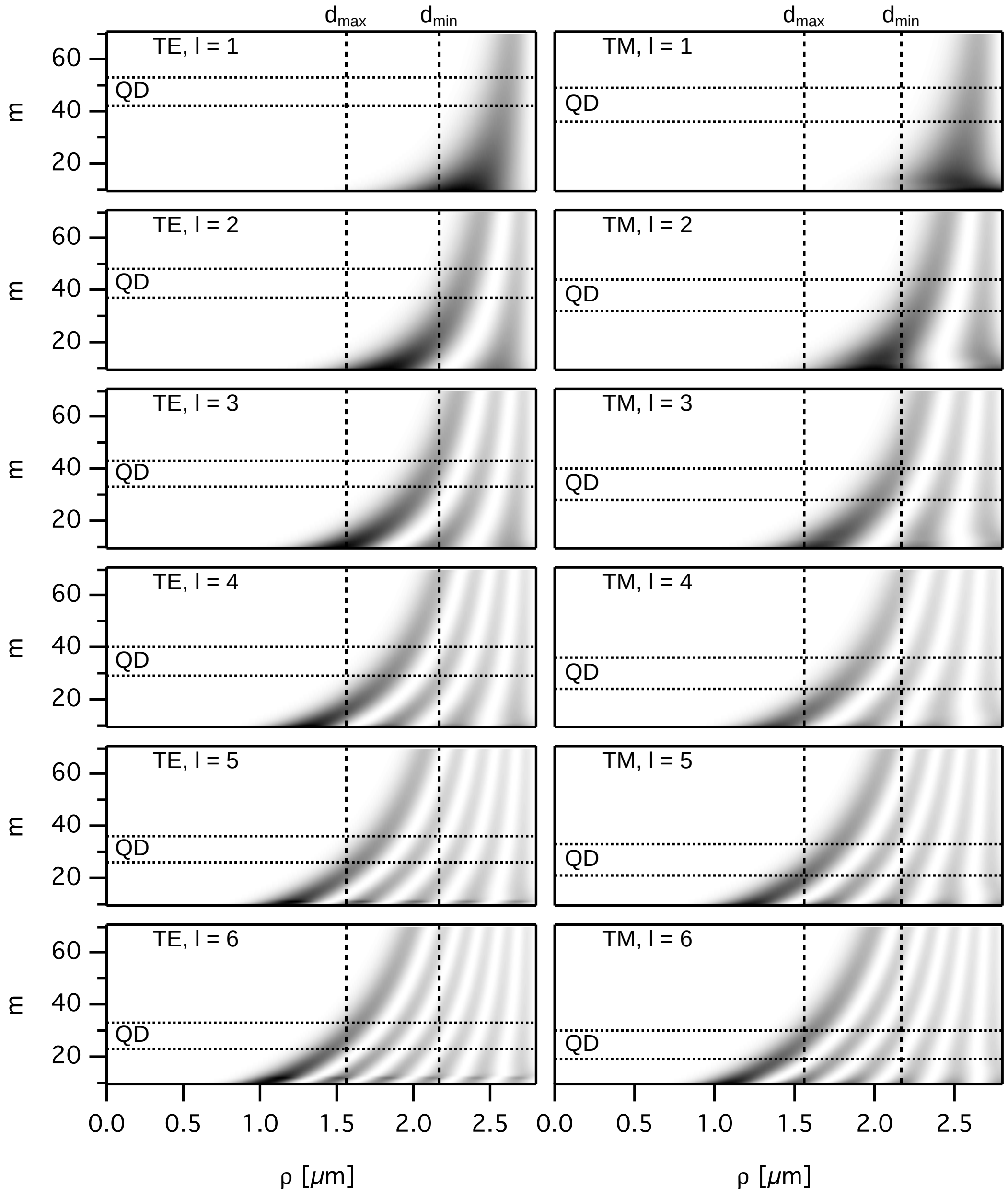

Figure 6.7: Calculated field distributions for a microdisk with a radius of $R = 2.800\,\mu\mathrm{m}$ and a thickness of $H = 250\,\mathrm{nm}$. Each plot shows the **H** field (TE) or **E** field (TM) distributions for azimuthal mode numbers from $m = 10$ to $m = 70$ and for one radial mode number l. The minimum and maximum hole distance d in the a1aX experiment are indicated as vertical dashed lines. The horizontal dotted lines indicate the energetic range of quantum-dot photoluminescence-emission. With increasing l the influence of the hole on a whispering-gallery mode gets stronger.

dashed lines indicate the minimum and maximum hole distance d_{min} and d_{max} taken from the experiment a1aX. We calculated the field distributions for azimuthal mode numbers m between 10 and 70 for radial mode numbers from $l = 1$ to $l = 6$. The embedded quantum dots emit in an energy range between $E = 1.1\,\text{eV}$ and $E = 1.3\,\text{eV}$. This energy range is indicated as horizontal dotted lines in each plot and is labelled with QD. We will call this energy range briefly QD range.

Figure 6.7 reveals that the differences in the field distribution between the whispering-gallery modes in TE and TM polarization are rather marginal. The main difference is that a TM mode with a given azimuthal mode number m has a higher energy than the TE mode of the same m. This difference is visible in the different positions of the QD range for TE and TM modes. We will thus make no distinction between the two polarizations in the discussion of the influence of the hole distance d on whispering-gallery modes. As stated in section 2.3.2, the higher the radial mode numbers l and the lower azimuthal mode numbers m are, the more will the field distributions be closer to the center of the microdisk. Whether or not a whispering-gallery mode is affected by the hole depends on both the field distribution and the hole position. Independent of the hole position, the $l = 1$ whispering-gallery modes are largely unaffected by the hole in the QD range. A noticeable influence of the $l = 2$ modes should only be visible for microdisks with the smallest hole distance d. For higher radial mode numbers l the distance d increases at which a whispering-gallery mode is unaffected by the hole. For $l = 6$ we expect all whispering-gallery modes to be strongly influenced by the hole.

In addition, we simulated the microdisk spectra of an experiment with varying parameter d with the finite-difference time-domain (FDTD) method. For this purpose we chose the outer microdisk parameters of an existing disk and varied the parameter d in very small steps over roughly the same range as d varies in the a1aX experiment. The results of these simulations provide a good overview of the effect that we expect to observe in our experiments and help us to identify the whispering-gallery modes. We simulated elliptical microdisks with $a = 5.747\,\mu\text{m}$ and $b = 5.491\,\mu\text{m}$ (eccentricity $e = 0.295$) and a thickness of $H = 250\,\text{nm}$, which are the disk dimensions of the microdisk a1a7. The simulations were carried out assuming two dimensions in a material with a constant refractive index n. This generally poses two problems: the 2d simulation does not account for the thickness of a microdisk and the refractive index n is dispersive in real experiments. The former problem can easily be solved by using the effective refractive index, but we cannot include the dispersion in the simulations. We chose the refractive indices according to the effective refractive index at $E = 1.28\,\text{eV}$ of the TE and TM polarization as $n_{TE} = 3.2$ and $n_{TM} = 2.95$. The parameter d was varied between $1.4\,\mu\text{m}$ and $0.4\,\mu\text{m}$ in 100 steps. The resulting spectra are shown as logarithmized grayscale plots in figure 6.8. Black means high emission intensity and white stands for no emission intensity. The dark vertical lines in the plots are thus the whispering-gallery modes. The horizontal white dotted lines indicate the range of the parameter d in the a1aX experiment. A horizontal cross-section in the image yields the photoluminescence spectrum of a microdisk with a certain parameter d. We can now easily distinguish the radial mode numbers of the whispering-gallery modes by analyzing the influence of the hole position. Some

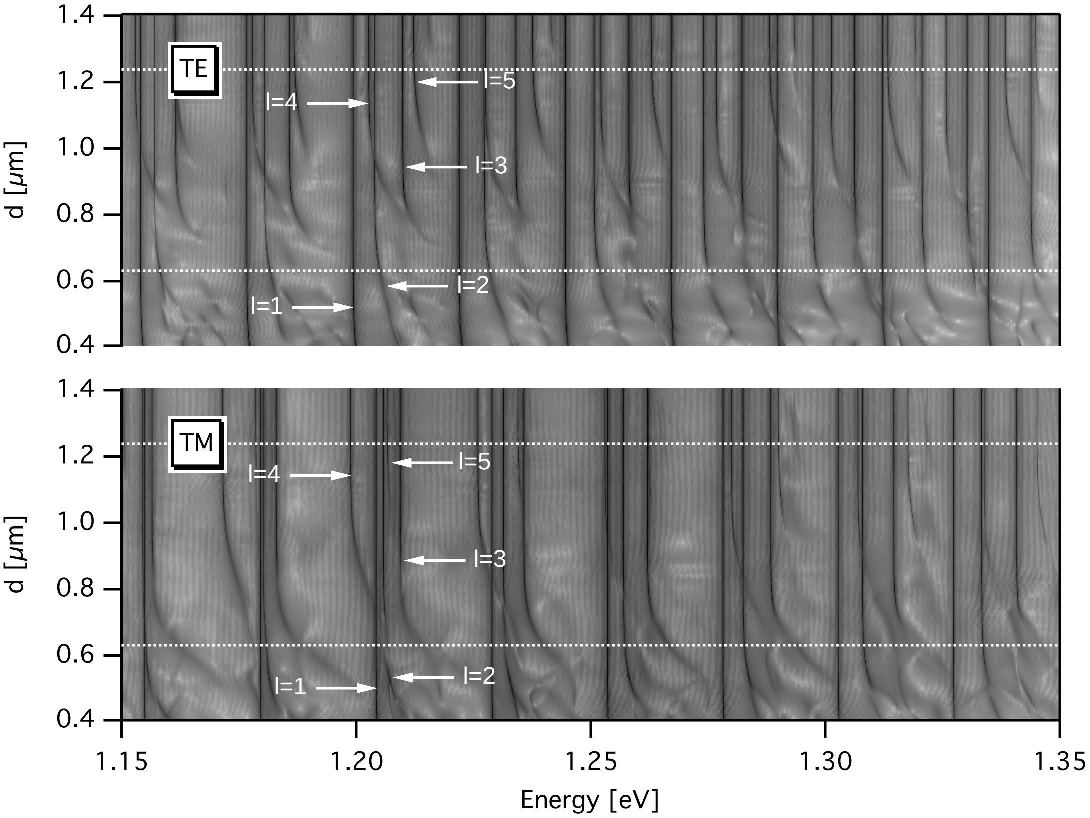

Figure 6.8: Finite-difference time-domain (FDTD) simulations of an experiment with varying hole distance d for TE and TM polarization. Black means high intensities and white zero intensity in this logarithmized plot. Each horizontal cross-section yields the whispering-gallery mode spectrum for a microdisk with a certain hole distance d. Whenever a hole interacts with a whispering-gallery mode, an energy shift to higher energies and the subsequent disappearance of the whispering-gallery mode occurs. This effect starts at different distances d for different radial mode numbers l. In this way, the radial mode numbers can easily be distinguished.

whispering-gallery modes are present over the whole range from $d = 1.4\,\mu\text{m}$ to $d = 0.4\,\mu\text{m}$. On the other hand, some whispering-gallery modes shift to higher energies and eventually vanish with decreasing d. This behavior may happen at different initial parameters d. This effect can easily be explained by the influence of the hole on whispering-gallery modes with different radial mode numbers l. The lines that are almost unaffected by the hole in the whole range of the parameter d are $l = 1$ modes. The $l = 2$ modes are affected by the hole and bend towards higher energies for small d. Modes with larger l are affected by the hole for larger d. A whispering-gallery mode may bend and cross a whispering-gallery mode with a lower l. These are the cases where avoided resonance crossings can occur. One arbitrarily chosen set of whispering-gallery modes with radial mode numbers from $l = 1$ to $l = 5$ are marked and labelled in figure 6.8 as an example for radial mode number identification.

We now compare these simulated results with our a1aX experiment in figures 6.9 and 6.10. Figure 6.9 (a) shows a waterfall plot of the spectra. In order to make the spectra comparable we subtracted the background from each spectrum and normalized the spectra to the whispering-gallery mode with the highest intensity. Note that the topmost spectrum in the figures originates from the microdisk a1a0, which has no hole. Figure 6.9 (b) shows the same spectra shifted by certain amounts to match the whispering-gallery modes with the highest intensity. The shift amount is plotted on right side of each spectrum. These shifts lie within an energy range of $\Delta E = 10\,\text{meV}$, which is in the same order as the shift determined for ordinary microdisks with the nominally same size in section 5.3. The shift is thus probably due to small size differences of the microdisks as a result of the fabrication process. After shifting the spectra, the TE $l = 1$ modes are all lined up well and now appear as vertical straight lines in the waterfall plot. The whispering-gallery modes next to the $l = 1$ modes on the high energy side are the $l = 2$ and $l = 4$ whispering-gallery modes close together, followed by a $l = 3$ whispering-gallery mode. This mode pattern repeats over the whole visible energy spectrum in the same way as shown in the simulations in figure 6.8. Some key features explained in the simulations are readily visible in this plot. The $l = 1$ modes appear in each spectrum and do not shift, broaden or vanish. The $l = 2$ whispering-gallery modes appear in each spectrum as well, but shift to higher energies and broaden for small hole distances d. The $l = 3$ modes can only be observed for the microdisks a1a1 to a1a6. The same effect can be seen for $l = 4$ modes, which can only be observed between the microdisks a1a1 and a1a5. In contrast to our expectations the microdisk without a hole a1a0 shows a quite different mode pattern than the ones with a hole.

Figure 6.10 shows both the experimentally obtained spectra and the simulated spectra as grayscale plot. The d parameter range is the same in both the experimental and simulated image. Note that the energy scale of the two spectra are slightly different and shifted with respect to each other. The distance between the $l = 1$ modes in the simulated plot is slightly larger than the measured ones which can be explained by the lack of dispersion in the simulations. Nonetheless we can observe the described features of the simulations in our experiment very clearly. The $l = 1$ whispering-gallery modes are not affected by the hole whereas the $l = 2$ whispering-gallery modes broaden and shift

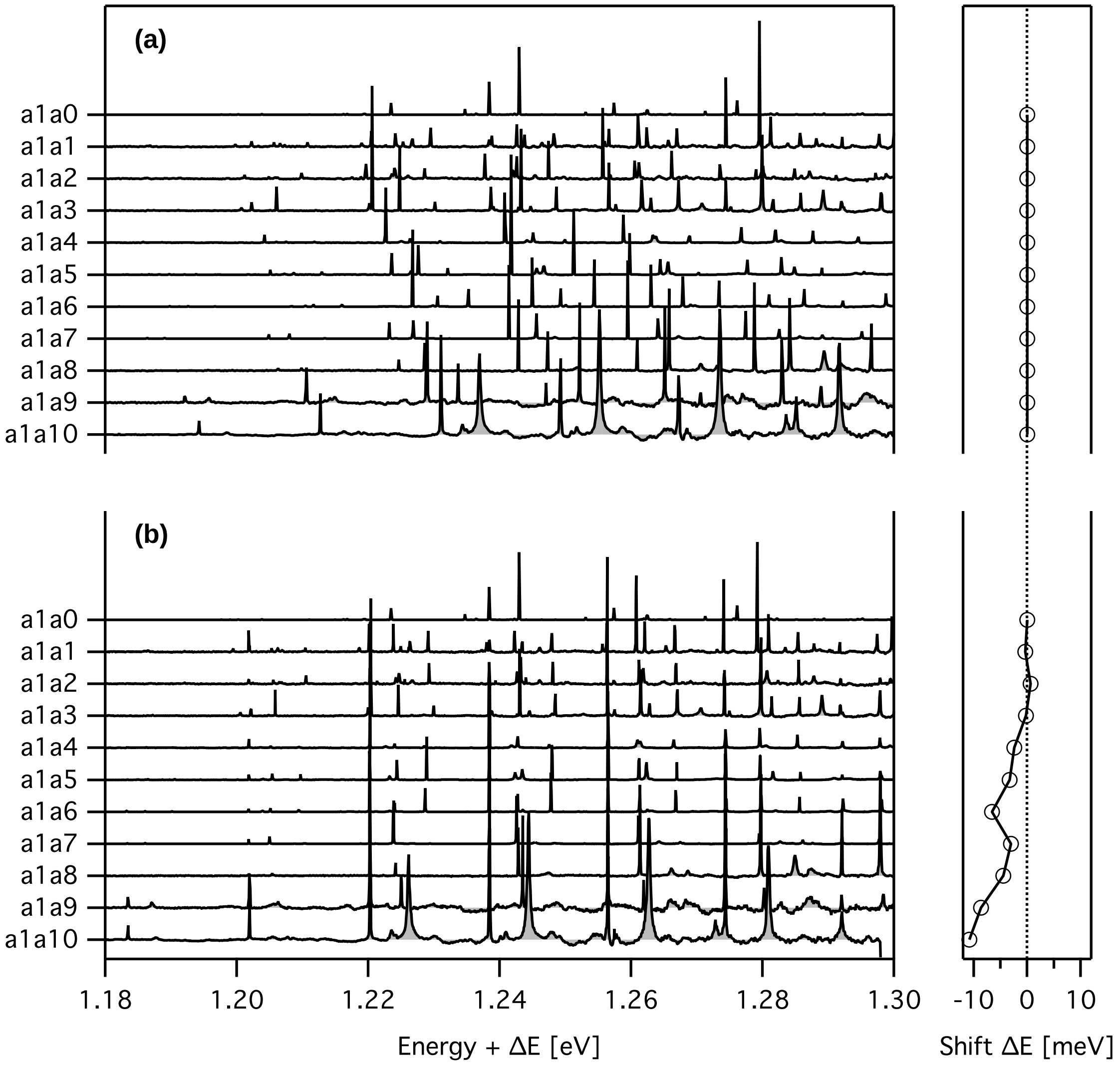

Figure 6.9: (a) Waterfall plot of the a1aX experiment. The background signal of spectra are subtracted and each spectrum is normalized with respect to its highest peak. (b) Same spectra as in (a) but shifted in energy. The shift is depicted on the right side of the graph. In (b) the $l = 1$ whispering-gallery modes appear as vertical lines in the plot. Modes with $l = 2$ are visible between two $l = 1$ modes for each microdisk. For disks with a larger parameter d, $l = 3$ and $l = 4$ whispering-gallery modes occur as well.

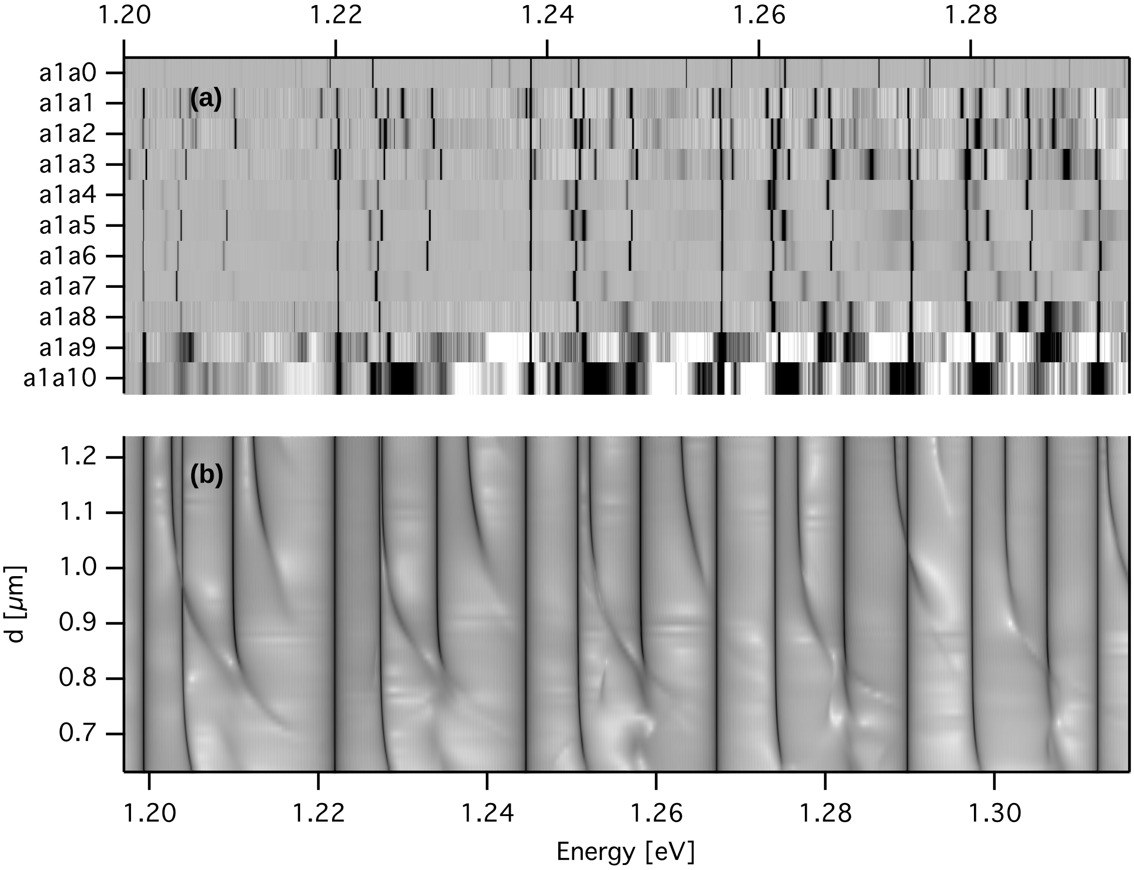

Figure 6.10: Grayscale plots of (a) the shifted experimental whispering-gallery modes and (b) the FDTD simulated whispering-gallery modes. The most prominent feature of the simulated spectra, such as shifting and disappearing of whispering-gallery modes with higher radial mode numbers l, can be observed in the experimentally obtained spectra as well. Note, that the energy scales on the two images are not the same due to the lack of dispersion in the FDTD simulations.

towards higher energies. The $l = 3$ modes vanish between the a1a6 and a1a7 microdisks. For larger d, where $l = 2$ and $l = 4$ whispering-gallery modes coexist. At $E \approx 1.288\,\text{eV}$ even a $l = 5$ whispering-gallery mode occurs in the experimentally obtained spectra. The exact position of whispering-gallery modes with higher radial mode numbers l may not coincide with the simulated ones, but all the key features of the FDTD simulations are perfectly observable.

Note that the experimentally obtained spectra were not taken all at the same time and with slightly different experimental settings, since the spatially resolved measurement of one microdisk may take between one and two hours. All experiments were conducted at temperatures between 4 K and 5 K, with a microscope objective of 100× magnification, a slit opening of 8 µm and with a broadened laser spot. Except for the microdisks a1a9 and a1a10 we used a tunable $Ti{:}Sa$ laser at 767.2 nm for excitation. The microdisks a1a9 and a1a10 were excited with a $HeNe$ laser at 632 nm. Comparative measurements have shown that the different excitation methods do not affect the whispering-gallery mode positions, but may have an effect on the relative intensities. Despite the different settings we can observe and simulate the effects described above quite well. An experiment under the same and perfectly stable conditions for all microdisks could deliver better information regarding the absolute photoluminescence intensity and width of the whispering-gallery modes.

6.4 Spatial emission behavior

This section investigates the spatial emission behavior of the pierced microdisks in the a1aX experiment. The investigation is performed on spatially resolved emission images of the microdisks at distinct energies. The first part of this section deals with the construction of emission images and considers the influence of the experimental setup on the resulting emission images. The second part presents and analyzes the emission images obtained in the a1aX experiment. We utilize the knowledge of the energetic whispering-gallery mode positions gained in the previous section to sort the emission images according to their mode numbers. This overview is crucial for an interpretation of the spatial emission behavior with respect to the mode number of a whispering-gallery mode.

6.4.1 Emission image construction

The general principle of the emission-image construction was described in chapter 3: basically, a number of spectra are taken at adjacent positions over a microdisk, which will later provide the x information of the emission image. Since the y information is preserved in the spectra, spatially and energetically resolved emission images can be compiled from the spectra (cf. figure 3.2). This technique has certain characteristics and limitations which we discuss in detail in this section.

We use the microdisk a1a6 in order to discuss the image construction and the implications with respect to our experimental setup. Figure 6.11 (a) shows a spectrum of the microdisk a1a6. Near $E = 1.237\,\mathrm{eV}$ two dashed lines are visible. These lines mark the energetic region that was used to generate the emission image shown in figure 6.11 (b). In this energetic region the emission intensity is integrated in each spectrum to a one-dimensional line, which yields the spatial y information. Width and position of the energetic region can be chosen as desired and is 1 meV wide in this case. Note that the energetic region in figure 6.11 (a) does not coincide with a whispering-gallery mode. The emission image in figure 6.11 (b) was compiled from 20 spectra taken at adjacent positions in x direction over a distance of 16 µm. Just as depicted in figure 3.2, the slit width determines the width of the image that is projected on the CCD chip. This width limits the energetic resolution of the spectra. For this experiment the slit was set to 8 µm width which results in very narrow images and a high energy resolution of the spectra. The 20 stripes are thus very narrow stripes in the whole 16 µm region and effectively map only a very small fraction of the examined area. These stripes, composed in x direction, form the emission image which initially has a resolution of 20 pixel in x direction and 512 pixel in y direction. In order to visualize the space in between the narrow stripes, the emission image is interpolated in x direction. The resulting image consists of the x and y spatial information where the intensity is depicted by a scaled pixel coloration. In the emission image 6.11 (b) blue stands for a low intensity, whereas yellow stands for a high intensity. Note that the color scale is normalized with respect to the highest emission intensity.

The emission image shows two concentric circularly shaped regions with higher emission intensity compared to the surrounding. These shapes are visible whenever the energetic region is chosen to be apart from the whispering-gallery modes. We attribute these shapes to the boundaries of the microdisk and the surrounding wall. This attribution is justified by comparison with images taken in the zeroth order of diffraction, where the spectrometer projects an image of the microdisk on the CCD camera. We appoint the microdisk and wall location on basis of these shapes, depicted in figure 6.11 as black circles. This location information is later needed for the investigation of the directional emission behavior. In the upper part of the microdisk a bright spot at about $y = 15\,\mu\mathrm{m}$ is visible. This is near the hole position of the microdisk.

After having the spatial position of the microdisk and wall localized in the emission image, we look at an emission image taken at the energetic position of a whispering-gallery mode. Exemplarily, an emission image of the same microdisk a1a6 is shown in figure 6.12 (a) for a whispering-gallery mode with $m = 48$ and $l = 1$. As in figure 6.11, the hole orientation points upwards in the image and the color scaling is again normalized with respect to the highest emission intensity. Here, the concentric circular intensity shapes have vanished and we now observe a beam-like emission pattern. The bright spot near the location of the hole is still visible and now much brighter compared to the rest of the image. The bright spot near the hole does not coincide with the boundary of the microdisk but lies somewhere in between the microdisk and the wall. Interestingly, the beam-like patterns are visible in regions beyond the wall. We do observe a somewhat higher intensity at the boundary of the surrounding wall compared to the region beyond

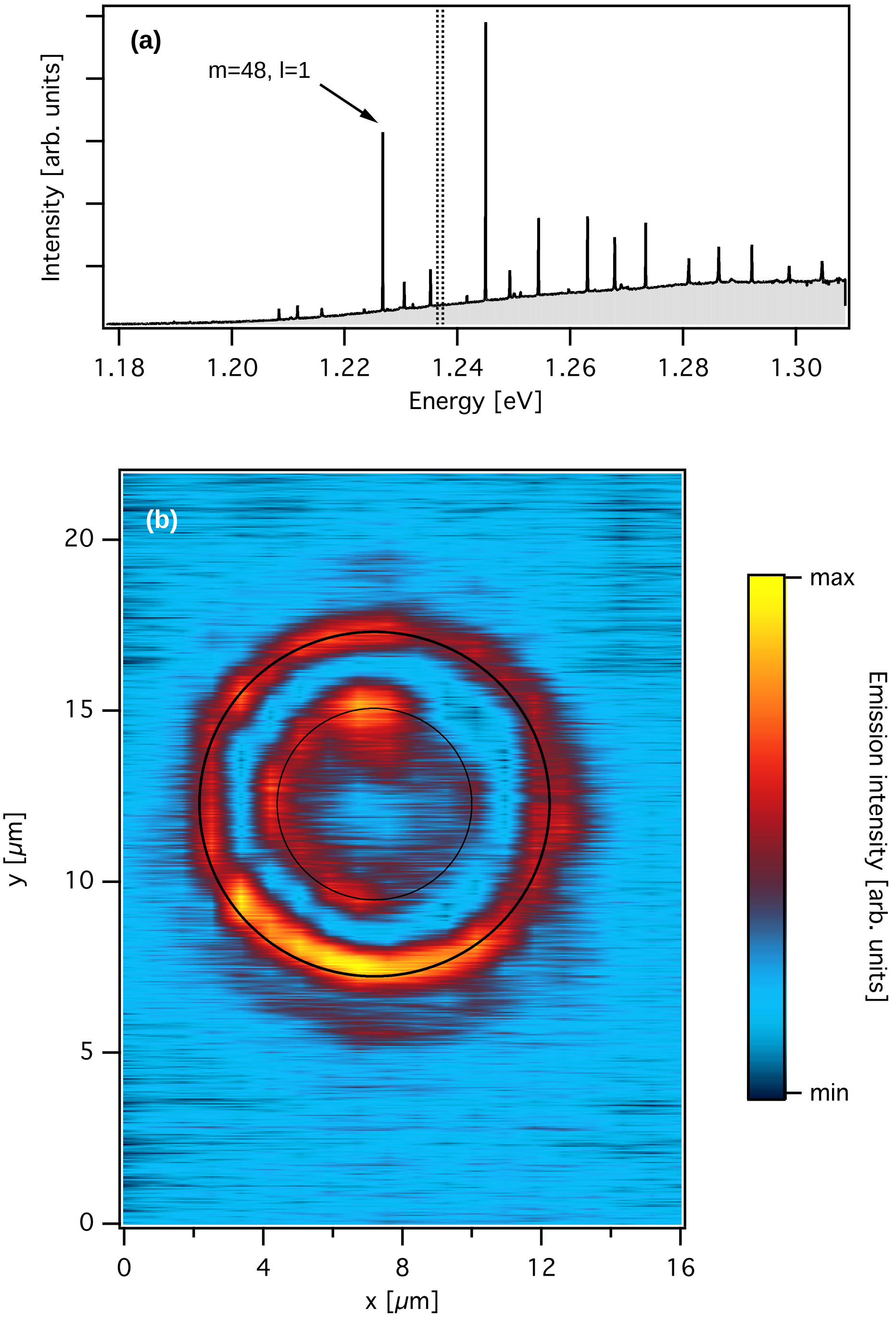

Figure 6.11: (a) Spectrum and (b) emission image of the microdisk a1a6. In (b), blue stands for low and yellow for high emission intensity. The image was assembled using 20 spectra taken at different positions on the microdisk. Every emission image is assembled for an energetic region, whose position and width can be arbitrarily chosen. For the emission image in (b), this energetic region is indicated by two dashed lines in spectrum (a). We chose a region between the visible whispering-gallery modes, because there the shape of the microdisk and the surrounding wall are clearly visible.

this boundary and there is clearly an intensity gap between the microdisk and the surrounding wall. Because of this gap we do not think that these beams are vectored directly toward the microscope objective, but are indeed emitted in the ρ-φ plane and scattered by surrounding material, as anticipated. The observed beam patterns beyond the boundary of the surrounding wall could be explained by a waveguide effect in the upper layer of the sample and scattering at impurities and surface roughness along the way.

In order to analyze the spatial emission behavior in the ρ-φ plane we take a profile of the emission intensity along the circumference of the surrounding wall, which we call ring profile. The spatial width range, in which the ring profile was integrated, is indicated by dashed lines in figure 6.12 (a). The ring profile is shown in figure 6.12 (c). This plot shows the intensity against the azimuthal position on the surrounding wall. The dashed line indicates the upward direction in the image and the left and right borders mark the downward direction in anti-clockwise and clockwise sense of rotation, respectively. The highest intensity was detected at about 4° and the width of this peak indicates a unidirectional emission of the pierced microdisk. We interpret an intensity peak measured at a certain position on the surrounding wall as a directional emission behavior. In this sense the profile in figure 6.12 (c) displays a distinct unidirectional emission behavior in the hole direction.

The experimental setup is not rotationally invariant due to the slit lying in y direction. We thus need to find out if the observed emission images are caused by the microdisks or if they occur due to the geometry of the system. For this purpose we took emission images of the same whispering-gallery mode on the same microdisk a1a6, this time the sample is rotated by 90°. The emission image is shown in figure 6.12 (b) and the corresponding ring profile in figure 6.12 (d). In both emission images the slit is lying parallel to the y axis. For the rotated emission image we now took 30 spectra over $16\,\mu\text{m}$ at adjacent positions to enhance the spatial resolution in x direction. In figure 6.12 (b) the bright spot is again visible, this time rotated by 90° as expected. The beam-like pattern is still observable, although much less pronounced than in figure 6.12 (a). The highest intensity peak in the ring profile now is detected at about 97°. This peak has almost the same width as the one observed in figure 6.12 (c) but is much less pronounced relative to the intensity at other angles. We explain this effect by the different measurement settings combined with the emission behavior of the microdisk. In the rotated emission image we decreased the slit width to $4\,\mu\text{m}$ in order to increase the energetic resolution. In both cases we used a *Ti*:*Sa* laser to excite the quantum dots, but the intensity was much higher in the measurement of the emission image in figure 6.12 (a) than in the rotated one. Unfortunately, it is not possible to exactly determine the excitation density by hindsight, due to the possibly differently widened laser spot on the sample. However, we can guess from the recorded laser intensities that the difference is in the order of one or two magnitudes. Due to this huge difference in excitation density, the exposure time was four times longer in the rotated case. Usually, we expect to observe the same emission pattern regardless of the excitation intensity, if the emission images consisted only of the signal coming from a whispering-gallery mode. Since the laser spot is widened, the

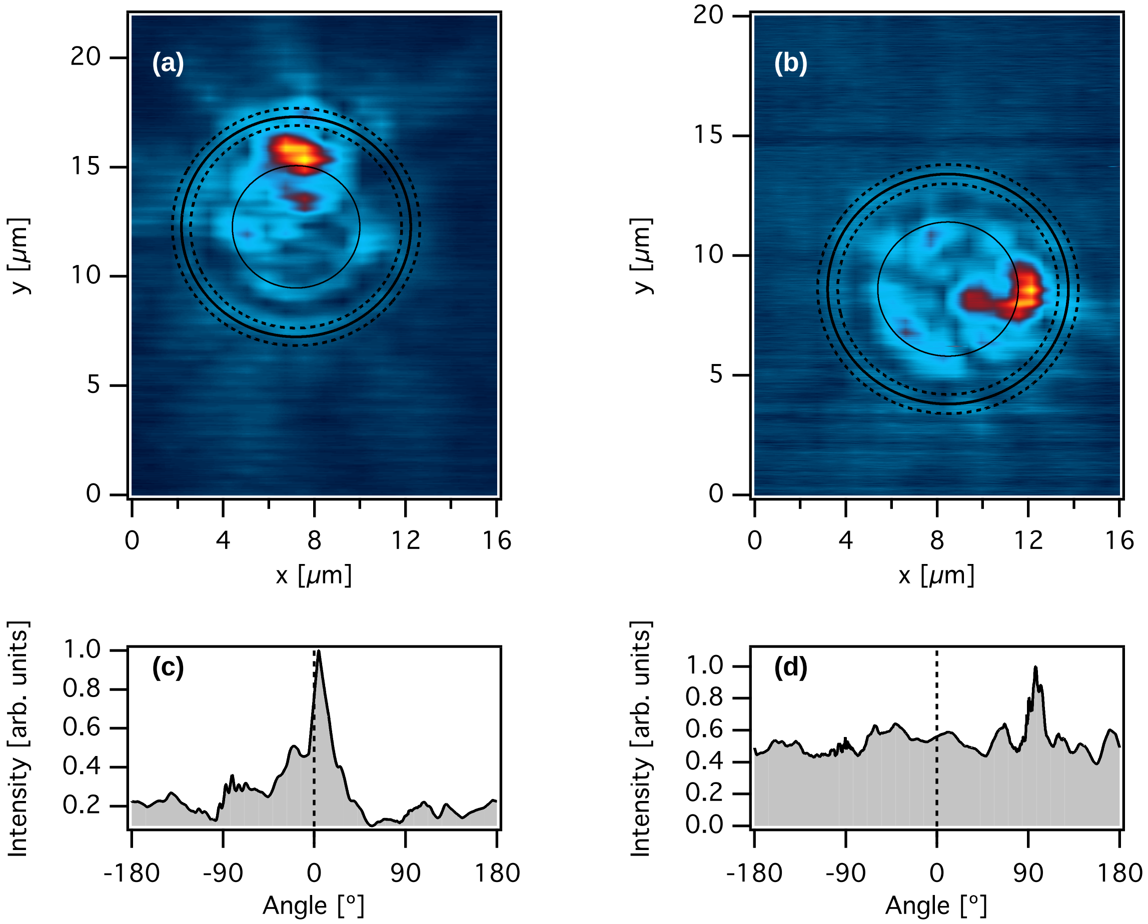

Figure 6.12: (a) Emission image of the microdisk a1a6 for a whispering-gallery mode with the mode number $m = 48$, $l = 1$. (b) Same experiment as in (a) with the microdisk rotated by 90° in the setup. (c) and (d) are ring profiles of the emission intensity along the circumference of the surrounding wall. The spatially integrated region used for the profiles is indicated as dashed lines in (a) and (b).

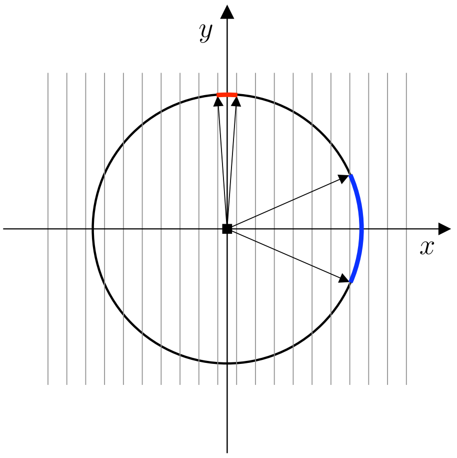

Figure 6.13: Illustration of the angular resolution of the system. The gray stripes depict the adjacent positions of the image stripes, where spectra were taken over the surrounding wall. The resolution of an emission image is limited by the distance of two neighboring points, where the lines intersect the circle.

light coming from the quantum dots in the surrounding material is detected as well. This light is not directional and uniformly distributed over the whole angular range. With increasing excitation intensities, this background signal increases linearly as does the signal coming from a whispering-gallery mode. If the excitation intensity is increased up to a certain point, the whispering-gallery modes start to lase, as will be shown in section 6.5. In this regime, the intensity of the whispering-gallery modes still increase linearly with the excitation intensity, but with a different gradient compared to the light coming from the quantum dots. An increment of the excitation intensity leads to a stronger whispering-gallery mode intensity compared to the background intensity. Thus, if the observed whispering-gallery mode emits unidirectionally, the emission peak should be more pronounced for higher excitation densities.

In conclusion, the rotating emission peak in the two emission images and ring profiles leads us to believe that the observed directional emission is not an effect of the setup, but does come from the microdisks themselves.

In the following analysis we focussed on measurements where we expect to observe the unidirectional emission along the y direction, i.e. the hole points upwards in the emission image. We neglect the emission images in rotated case because of the higher angular resolution in the upward direction. Figure 6.13 illustrates a set of 20 spectra taken over a surrounding wall. Each line depicts a narrow stripe of the whole image. The angular resolution is determined by neighboring points, where the lines intersect the circle: The closer two points on the circle are, the higher the angular resolution. It is obvious from figure 6.13 that the highest angular resolution is gained for emission in y direction.

6.4.2 Spatial emission comparison for different mode numbers

In the figures 6.14, 6.15, 6.16 and 6.17 the ring profiles of all the whispering-gallery modes observed in the a1aX experiment are shown. The associated emission images are difficult to interpret by direct observation and thus are shown in appendix B.

Each plot shows only the whispering-gallery modes for one radial mode number l. The plots are sorted from left to right according to their azimuthal mode number m.

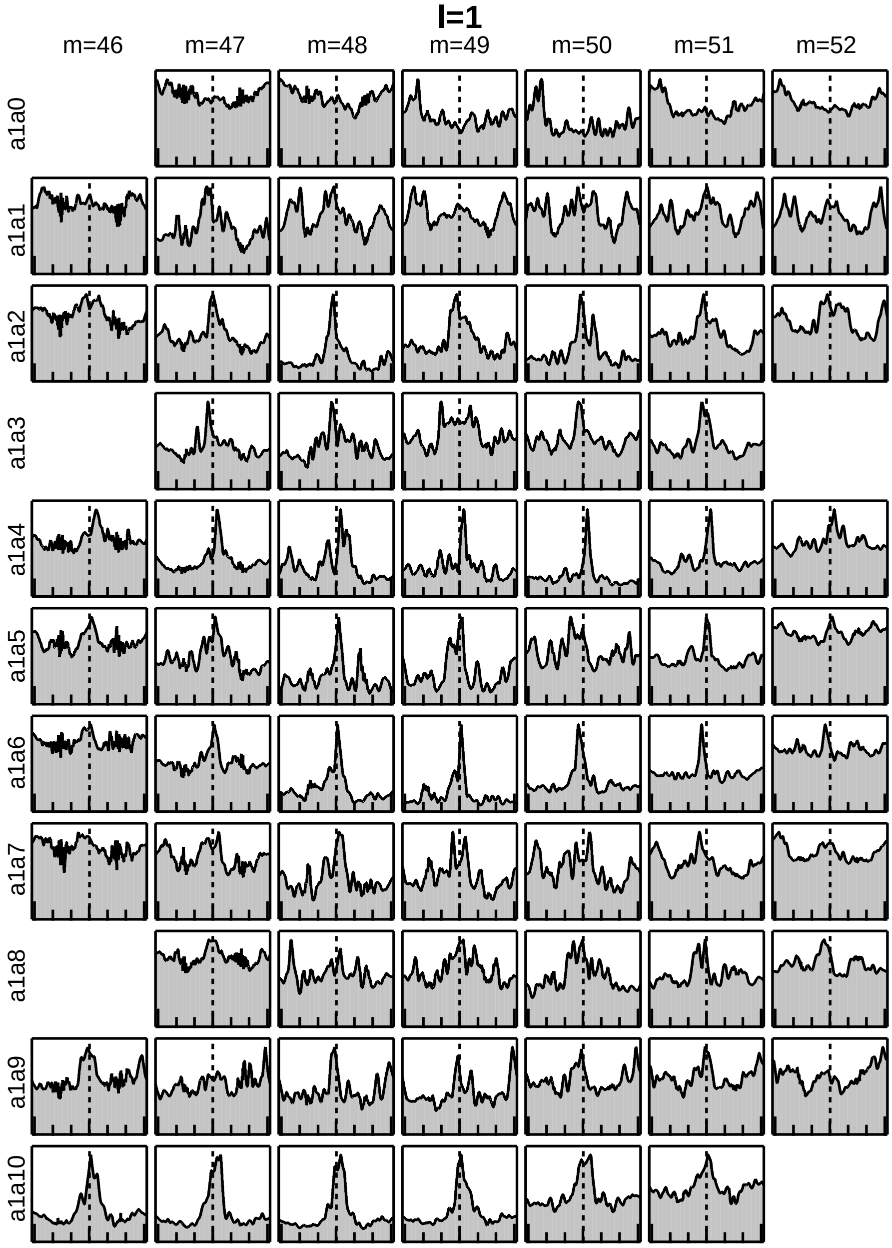

Figure 6.14: Profile plots for the a1aX experiment with $l = 1$. The plots show the intensity (ordinate) versus angular position (abscissa) of the circumferential intensity at the surrounding wall. The axes labels are omitted due to the lack of space. The y axis shows the photoluminescence intensities and the x axis shows the angle α from $-180°$ to $180°$ as in the figures 6.12 (c) and 6.12 (d). The topmost row shows profile plots of the microdisk a1a0 without a hole. The hole distance d is decreasing from microdisk a1a1 to a1a10.

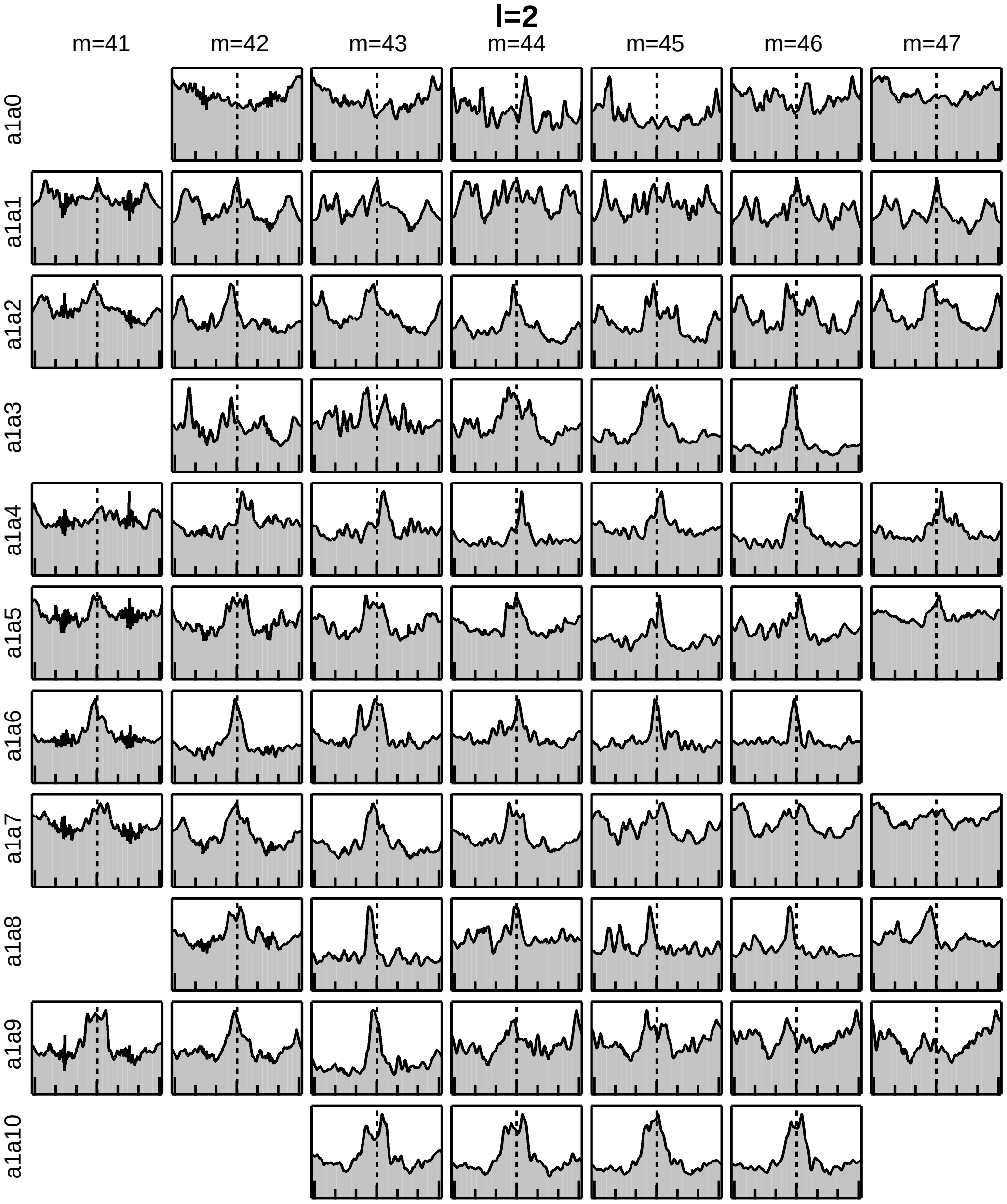

Figure 6.15: Profile plots for the a1aX experiment with $l = 2$. The plots show the intensity (ordinate) versus angular position (abscissa) of the circumferential intensity at the surrounding wall. The axes labels are omitted due to the lack of space. The y axis shows the photoluminescence intensities and the x axis shows the angle α from $-180°$ to $180°$ as in the figures 6.12 (c) and 6.12 (d). The topmost row shows profile plots of the microdisk a1a0 without a hole. The hole distance d is decreasing from microdisk a1a1 to a1a10.

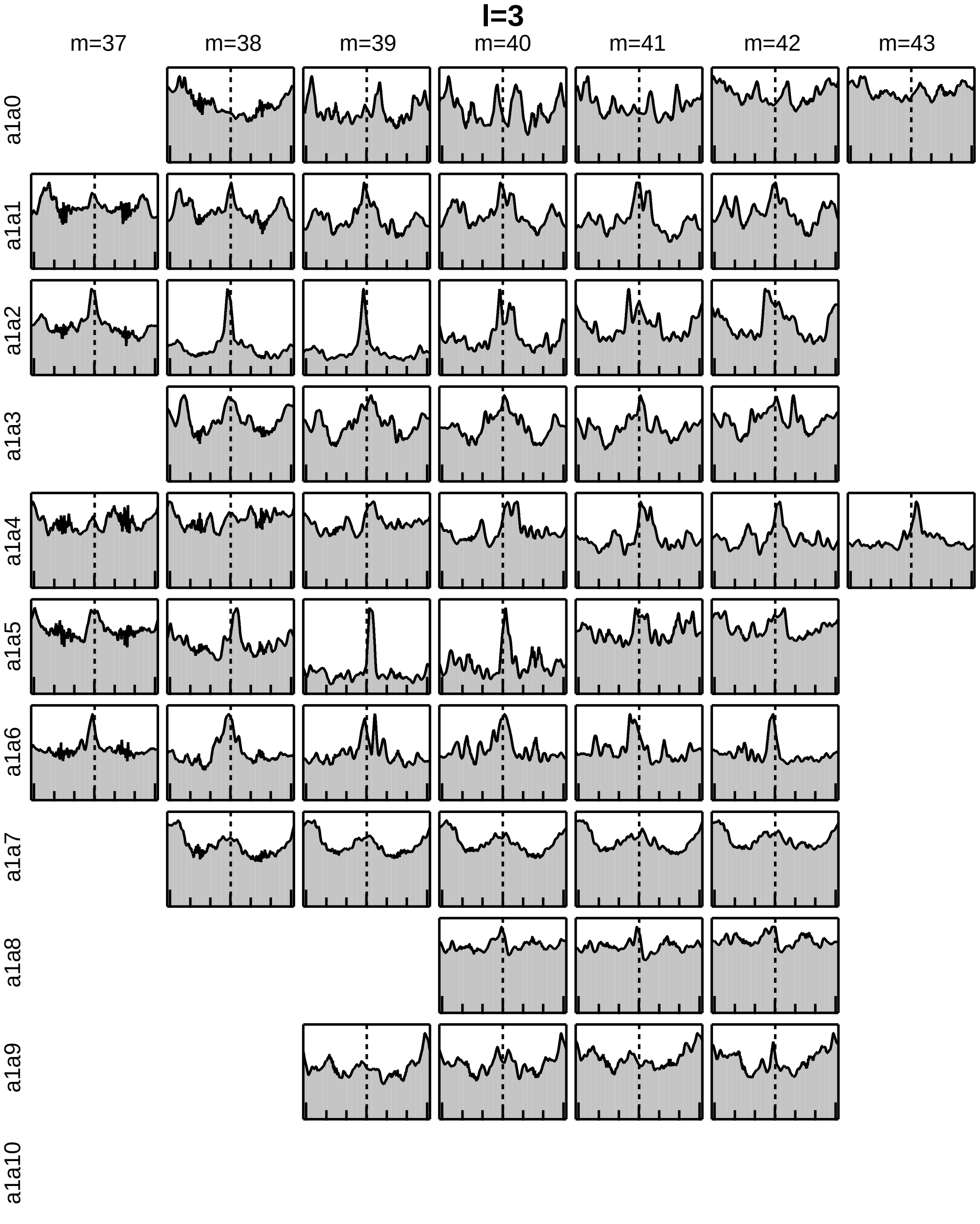

Figure 6.16: Profile plots for the a1aX experiment with $l = 3$. The plots show the intensity (ordinate) versus angular position (abscissa) of the circumferential intensity at the surrounding wall. The axes labels are omitted due to the lack of space. The y axis shows the photoluminescence intensities and the x axis shows the angle α from $-180°$ to $180°$ as in the figures 6.12 (c) and 6.12 (d). The topmost row shows profile plots of the microdisk a1a0 without a hole. The hole distance d is decreasing from microdisk a1a1 to a1a10.

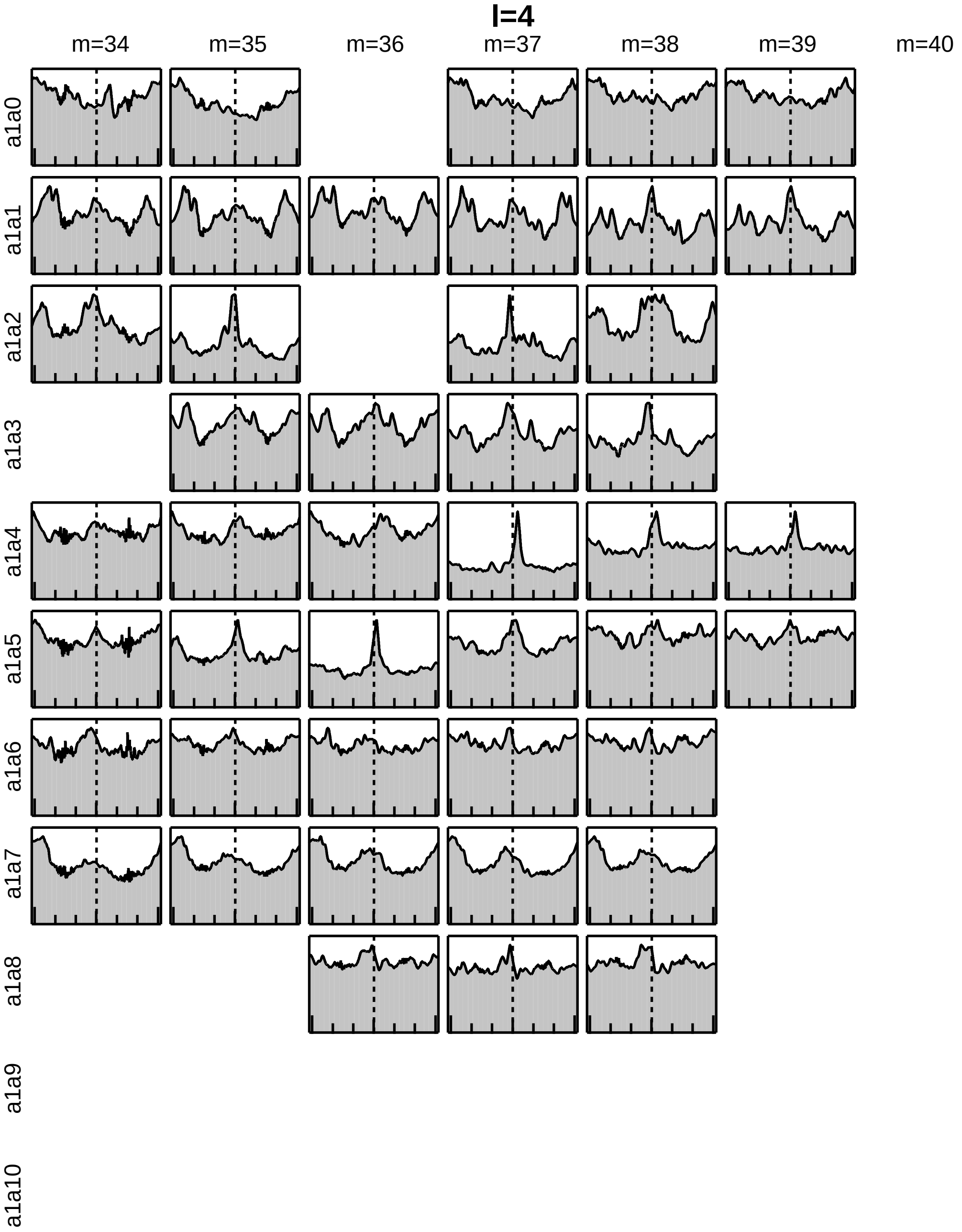

Figure 6.17: Profile plots for the a1aX experiment with $l = 4$. The plots show the intensity (ordinate) versus angular position (abscissa) of the circumferential intensity at the surrounding wall. The axes labels are omitted due to the lack of space. The y axis shows the photoluminescence intensities and the x axis shows the angle α from $-180°$ to $180°$ as in the figures 6.12 (c) and 6.12 (d). The topmost row shows profile plots of the microdisk a1a0 without a hole. The hole distance d is decreasing from microdisk a1a1 to a1a10.

The topmost row displays the ring profiles of the ordinary microdisk a1a0 without a hole while the other rows are sorted from top to bottom according to the hole distance d. As explained for the ring profiles above, the dashed line marks the point in the upward direction of the emission images and is labelled with 0°. For the a1aX experiment this direction coincides with the direction of the hole with respect to the center of the microdisk. The left and right border of each profile show the intensity in the ring profile for the opposite anti-clockwise and clockwise direction, respectively. Each profile is normalized to its highest intensity. Due to the lack of space, we omitted to apply axes labels to the plots. Keep in mind, that each profile plot has exactly the same axes labels as the profiles shown in the figures 6.12 (c) and 6.12 (d).

We now investigate the general tendencies observed in the figures 6.14, 6.15, 6.16 and 6.17. In the observations and analysis we interpret the intensity patterns in the profiles as emission directions. However, one should keep in mind that these profiles deliver a good indication for a directional emission behavior but do not represent direct measurements of the emission direction.

We first examine the profiles from the microdisk a1a0, since they constitute a reference for the microdisks with a hole. Most obvious is the lack of a favored emission direction in these profiles. For most whispering-gallery modes of a1a0 the intensity is distributed quite homogeneously. The peaks which do occur, like $l = 1$, $m = 50$ or $l = 2$, $m = 44$, are not very pronounced and do not appear at the same positions every time. The only regular pattern in these profiles seems to be a slighly enhanced emission in downward direction (180°) compared to the upward direction (0°), visible as broad dip in near the dashed line in the profiles.

The profiles of the microdisk a1a1 do not display very distinct unidirectional emission patterns as well. But in contrast to microdisk a1a0, we do observe in a few profiles a slightly directed emission towards 0°, mainly as a reoccurring peak near the dashed line. However, these peaks reoccur together with other peaks observed at different angles like the double peak near −130°.

The situation changes dramatically for the microdisks a1a2 to a1a10. For all these microdisks we can find at least one profile that displays a very clear peak in the direction close to 0°. On the other hand, no microdisk continually displays a single peak for all whispering-gallery modes. These occurrences of peaks do not seem to follow an obvious regular pattern.

The most striking result yields the comparison between the profiles of the microdisk a1a0 without a hole and all other microdisks. Since the examined microdisks are elliptically shaped with the major axis lying in the y direction, it is not per se clear that the geometrical hole causes the observed unidirectional emission or if rather the ellipticity explains this effect. With the profiles of the microdisk a1a0 we can rule out the latter possibility. If the ellipticity played a major role for the unidirectional emission, we should be able to observe similar emission behaviors for the microdisk a1a0 and the microdisks with a hole.

Some microdisks sometimes display extremely distinct unidirectional emission, like the microdisk a1a5 for the whispering-gallery mode $l = 3$, $m = 39$ with a very narrow intensity distribution of about 22°. In other cases unidirectional emission behavior is visible, but spreads over a much broader angle, like the microdisk a1a3 for the whispering-gallery mode $l = 2$, $m = 45$, where the distribution spreads over roughly 61°. These peaks often appear in groups of adjacent azimuthal mode numbers m. Occasionally, in these groups the profile with most pronounced and narrow intensity distribution is enclosed by profiles with less pronounced and narrow intensity distributions. This effect can be observed for the microdisk a1a6 for the radial mode number $l = 1$ or for microdisks a1a2 and a1a5 with $l = 3$. Although the physical cause for this effect is not clear, we suggest the following interpretation. Two whispering-gallery modes are required to constitute an avoided resonant crossing mode: A high-Q whispering-gallery mode with a low radial mode number l and a low-Q whispering-gallery mode with higher l, which emits unidirectionally due to the influence of the hole. The low-Q mode is strongly broadened compared to the same but unaffected mode. The broadening could have the effect that one low-Q mode potentially crosses more than one high-Q mode. For example a low-Q mode with $Q = 25$ has a width (FWHM) of 50 meV. Comparing this energetic range with our experiments shows that there are about 3 high-Q whispering-gallery mode in an energy range of 50 meV. If one low-Q mode has the ability to generate avoided resonance crossings with more than one high-Q mode, we would expect to see adjacent unidirectional emission patterns.

Finally, we note once more that the spectra of the microdisks were taken with different parameters. These parameters, especially the exciting laser intensity, do have an effect on emission images as explained above. A list of the experimental setting parameters for each microdisk in the experiment a1aX can be found in appendix C.

6.5 Q factors and lasing

The goal of this work was to generate high-Q unidirectional whispering-gallery modes. We have shown in the previous sections that we are able to successfully generate unidirectional emission behavior from pierced microdisks. This section briefly analyzes the Q factors of the whispering-gallery modes in the a1aX experiment. The analysis is preceded by a few remarks on the relationship between lasing and the Q factor.

The Q factor is a quantity defined by the photon lifetime in a cavity. For excitation intensities below the laser threshold it is predicted that the line width (FWHM) of a whispering-gallery mode decreases with increasing excitation power. This effect can be explained in two ways. First, with increasing excitation power more excitons exist in the resonator leading to less absorption of the light in the resonator. Less absorption leads according to equation 2.43 to narrower line widths [19]. The other approach explains the line width narrowing by increasing time coherence in the system [29]. Both approaches depend linearly but with different sensitivity on the excitation power. According to Michler et al. the exciton bleaching occurs below the laser threshold and the time coherence prevails above the laser threshold [30]. Excitation power dependent measurements should thus show a nonlinear emission intensity curve. At the laser threshold we expect to observe a bend in the intensity curve.

This effect has an implication on the determination of the Q factor as an indicator of the quality of the resonant cavity. If the Q factor shall give an estimate of the resonator quality, the Q factor should be measured near the transparency threshold, since the increase of the time coherence is not directly dependent on the cavity quality.

In order to ascertain if the pierced microdisks are able to perform lasing, we carried out an experiment with varying excitation power. The experiment was performed at a temperature of $T = 4.4\,\mathrm{K}$ on the microdisk a1a8 with our *Ti*:*Sa* laser which was tuned to 767.2 nm. In contrast to the defocussed experiments for the spatial emission images the laser spot was focussed, e.g. on the center of a microdisk. We varied the excitation intensity from 1 mW to 32 mW in 1 mW steps. Note that the excitation intensity was not measured at the location of the sample (cf. figure 3.1) and cannot give absolute information about the excitation density on the sample.

The results of this experiment are depicted in figure 6.18. This graph shows the emission intensity of the whispering-gallery mode $m = 50$, $l = 1$ as a waterfall plot in dependence of the excitation intensity. For each intensity the curve was fitted with a Lorentz function in order to evaluate the position x_0, the intensity I and the width w (FWHM) of the whispering-gallery mode. The results of this evaluation are plotted in figure 6.19. In the figures (a) and (b) we observe an increase of the emission intensity I and a decrease of the line width w with increasing excitation power. Obviously, I and w do not behave linearly with the excitation power. On the other hand, there is no discernible kink in both curves, which could indicate the onset of laser action. The Q factor derived from x_0 and w lies between 3.58×10^3 and 25.9×10^3 and is shown in figure (c). The high Q factor compare very well to the Q factors measured by other groups for similar microdisks without a hole [19, 29]. Higher Q factors (up to 6.6×10^5) have been measured for different microdisk and under different conditions [31, 32].

A look at the emission image of the $m = 50$, $l = 1$ whispering-gallery mode of the microdisk a1a8 in figure 6.14 reveals, that the unidirectionality is not the most pronounced compared to other whispering-gallery modes. The whispering-gallery mode $m = 50$, $l = 1$ on the microdisk a1a4, which has a very clear unidirectional emission behavior, has a Q factor of 19.5×10^3. The Q factors for all whispering-gallery modes in the a1aX experiment are listed in appendix C. The Q factors tend to be lower for higher radial mode numbers l. Most Q factors are larger than 1×10^3 for all l. The Q factors for $l = 1$ reach almost up to 30×10^3. For $l = 1$ we often observe a splitting of the whispering-gallery mode. This splitting occurs, if the degeneracy of the two opposed wave propagation directions, clockwise and anti-clockwise in the microdisk, is lifted. In this case the Q factors as well as the energetic position was given for both peaks of the whispering-gallery mode. The Q factors of appendix C in combination with the emission images in the figures 6.14, 6.15, 6.16 and 6.17 demonstrate the existence of very high Q, highly directional whispering-gallery modes in the a1aX experiment.

We furthermore Note that the energetic whispering-gallery mode position x_0 shifts with the excitation power, as shown in figure 6.19 (d). For very low excitation powers x_0 shifts rapidly towards higher energies. At roughly 3 mW the blueshift stops and x_0

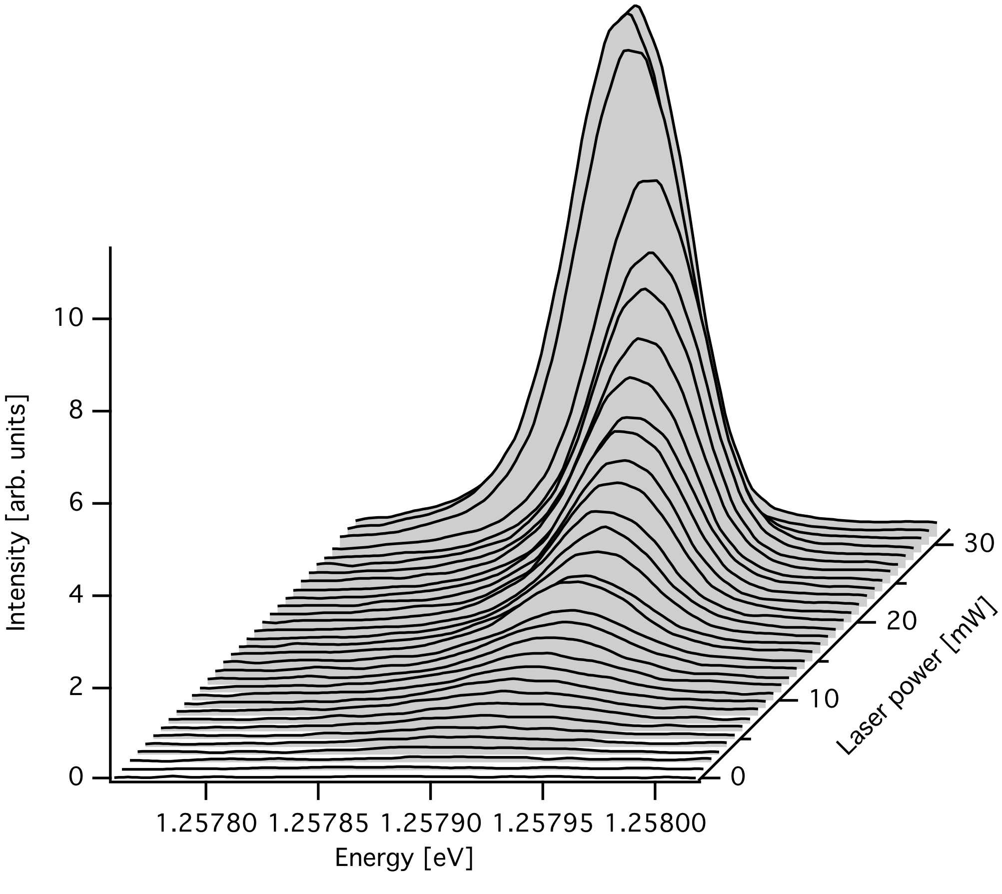

Figure 6.18: Excitation power dependent measurements on the $m = 50$, $l = 1$ whispering-gallery mode for the microdisk a1a8. The excitation power varies from 1 mW to 32 mW in 1 mW steps.

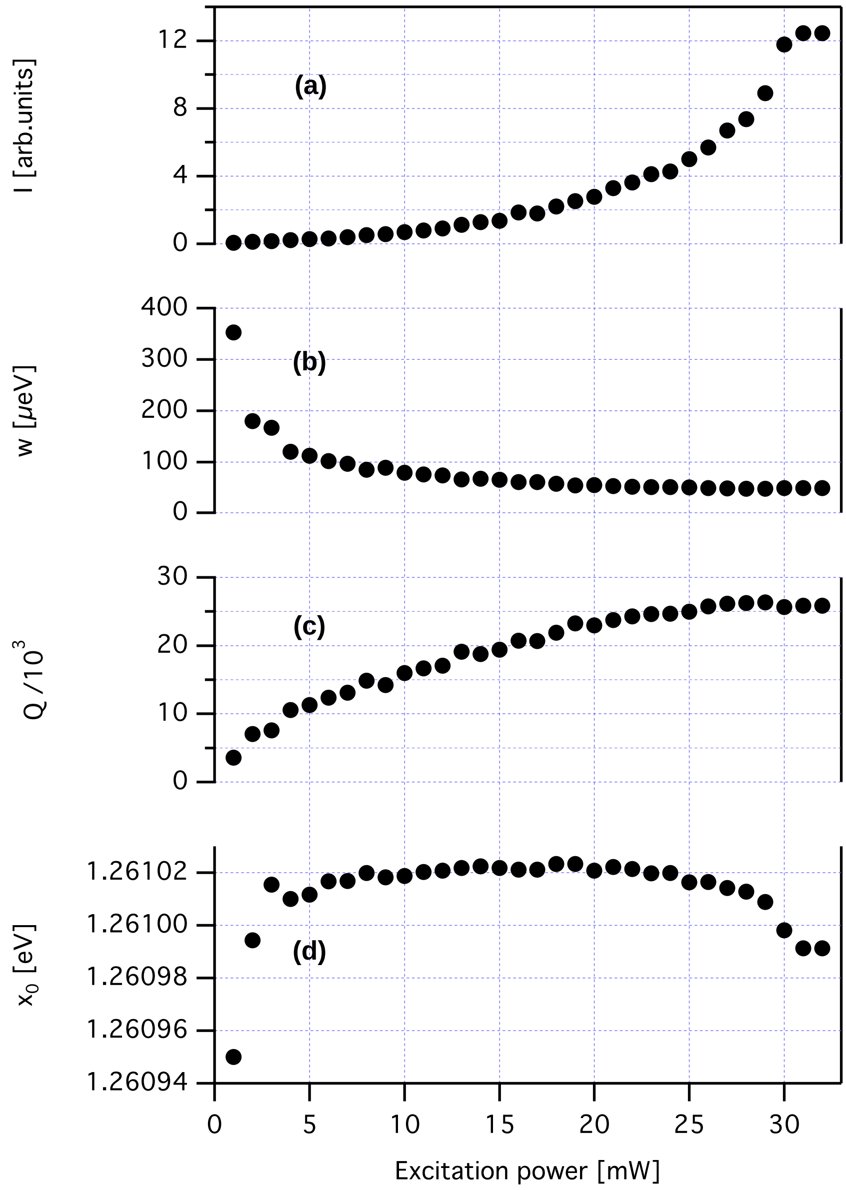

Figure 6.19: Variation of whispering-gallery mode parameters with excitation power. The parameter are obtained by fitting Lorentz functions to the photoluminescence spectra shown in figure 6.18. The emission intensity I and the width w clearly show a non-linear behavior with the excitation power in (a) and (b). The Q factors in (c) lie between 3.58×10^3 and 25.9×10^3. With higher excitation power the energetic whispering-gallery mode position x_0 shifts to lower energies (d).

remains almost constant. Near 20 mW x_0 gently shifts towards lower energies. For the redshift with high excitation powers we can give the following explanation. The band gap of $GaAs$ depends on the temperature of the sample [27]. At high excitation powers the sample is heated by the excitation laser, which leads to a lower band gap energy and thus a redshift in the photoluminescence spectra. We have no physical explanation for the blueshift at lower excitation powers, but the whispering-gallery mode intensity is very low and thus the error of the fit may be quite high.

In conclusion, the excitation intensity dependent measurements clearly indicate that the pierced microdisks emit in the laser regime. The Q factors are very high and compare quite well to similar ordinary microdisks. The combination of very high Q factors and occasionally very clear unidirectional emission suggests that indeed avoided resonance crossings occur in the a1aX experiment.

7 Conclusion

In this work we experimentally investigated the spatial emission behavior of pierced microdisks. In order to achieve this goal, we fabricated ordinary and pierced microdisks, developed a theoretical model to energetically allocate the whispering-gallery modes and conducted experiments on the microdisks. In this conclusion, we summarize each of these steps and provide an outlook for possible future research on pierced microdisks.

The fabrication of microdisks was based on electron-beam lithography and a two-step wet-etching process. For the first wet-etching step we used an etching solution based on hydrobromic acid HBr. With our etching solution we achieved to fabricate microdisks with very high quality factors of the observed whispering-gallery modes. The investigation of SEM images showed that the etching solution produces microdisks with a slight ellipticity. We attribute this effect to the non-isotropic etching of our solution. Although the ellipticity is rather small, we cannot entirely eliminate the possibility that it has an impact on the unidirectional emission of the pierced microdisks. It would thus be recommendable to further experiment with the compound of the etching solution in order to find a completely isotropic etching solution. The fabrication of pierced microdisks was challenging, since the deep etching process with HBr is strongly diffusion controlled and thus very sensitive on stirring. In particular, nominally equal air holes show strong variations in their diameters. Furthermore, the microdisk radius cannot be reduced arbitrarily, since the size of the air hole always relates with the etching depth. Both problems could be solved by combining a wet etching process for the boundary of the microdisk with a dry etching process for the air hole. A fabrication process would look like this: In the first step the air holes are pierced into the sample with the help of electron-beam lithography and ion-beam etching (RIE, Ar^+). In the second step the microdisks are defined by again using electron-beam lithography but then a wet-etching solution. Due to the highly anisotropic ion-beam etching the hole radii do not depend on the etching depth and this process yields more reproducible results compared to the wet etching. This way the microdisk radii could be reduced and the reproducibility could be enhanced.

In order to allocate the whispering-gallery mode numbers, we developed a theoretical model based on two different well known models. Our model combines the calculation of resonant whispering-gallery modes in a two-dimensional microdisk with a model for the calculation of resonant modes in a coplanar wave guide. Our model allows the calculation of the energetic positions of the whispering-gallery modes, their energetic widths and their field distributions. We furthermore incorporated a material dependent dispersion. In chapter 5 we used this model to allocate whispering-gallery modes for varying microdisks radii. Mapping the energetic position of the calculated whispering-gallery modes against the microdisk radius produces meaningful patterns. In principle, these patterns could be used to quickly allocate experimentally observed whispering-gallery modes. We investigated this model more closely by comparison to experiments on microdisks with a fixed radius. This investigation showed, that the energetic positions of whispering-gallery modes are very sensitive to the dispersion of the material. Due to this observation, we think that a theoretical model has to be carefully adapted to the material dispersion in order to yield correct results. We took this approach for the experiments on pierced microdisks and could approve the results by comparison to finite-difference time-domain simulations. Interestingly, the pierced microdisks generate only whispering-gallery modes in transverse electric polarization. The ordinary microdisks on the other hand seem to emit whispering-gallery modes in both polarizations.

For the investigation of the spatial emission behavior of pierced microdisks we designed a sample layout to obtain spatial emission information from the microdisks with our experimental setup. Our micro-photoluminescence setup offers the possibility to measure spectra while preserving the spatial information in one direction. The microscope objective collects light emitted into a certain angle. Neither the sample nor the detector can be rotated in this setup. We considered these setup characteristics to create a sample design that allows for the spatial investigation of the microdisk emission. The new layout benefits from the planar emission behavior of the microdisks: each microdisk is surrounded by a circular wall that scatters the near-field emission of the microdisk. We take a series spectra along adjacent positions in x direction. In each spectrum the y information is preserved. We are able to generate spatially and energetically resolved emission images of a microdisk out of these spectra. The spatial resolution is limited by the number of the adjacent spectra. The analysis of the emission images shows that the pierced microdisks indeed show unidirectional emission. The quality factors are generally very high, reaching up to 30×10^3. On whispering-gallery modes with a high unidirectional emission behavior we measure quality factors up to 20×10^3. These quality factors are comparable to the ones measured on ordinary microdisks with similar disk parameters. These high quality factors and very narrow unidirectional emission angles make the pierced microdisks very promising systems for a unidirectionally emitting whispering-gallery mode resonator. For further research on this topic it would be interesting to investigate pierced microdisks in an experimental setup that allows for the direct measurement of the microdisk emission direction. This could confirm the observations made in our experiments.

Appendices

Appendix A

Effective refractive index for resonant waveguide modes

In a coplanar resonator resonances occur if

$$1 - r^2 e^{i2Hk_z} = 0 \tag{A.1}$$

is fulfilled, where r is the complex reflection coefficient for a light wave coming from inside the microdisk and H is the height of the microdisk. The reflection coefficient r can be calculated with the Fresnel Formulae according to the polarization of the light to

$$r_{TE} = \frac{k_z - k'_z}{k_z + k'_z} \qquad \text{or} \qquad r_{TM} = \frac{k_z - n^2 k'_z}{k_z + n^2 k'_z}. \tag{A.2}$$

We rewrite equation A.1 to

$$e^{-i2Hk_z} = r^2 \tag{A.3}$$

and apply the Fresnel Formulae for r in TE polarization[1]:

$$e^{-i2Hk_z} = \left(\frac{k_z - k'_z}{k_z + k'_z} \right)^2. \tag{A.4}$$

---

[1] We omit a detailed calculation for TM polarization, since the principle is the same and present the results of TM calculation at the end of this chapter.

We now rewrite this equation in a more convenient form and later on substitute k_z by n_{eff}:

$$\begin{aligned}
\pm e^{-iHk_z} &= \frac{k_z - k'_z}{k_z + k'_z} \\
\pm e^{-iHk_z} &= \frac{1 - \frac{k'_z}{k_z}}{1 + \frac{k'_z}{k_z}} \\
\pm e^{-iHk_z}\left(1 + \frac{k'_z}{k_z}\right) &= 1 - \frac{k'_z}{k_z} \\
\pm e^{-iHk_z} \pm e^{-iHk_z}\frac{k'_z}{k_z} + \frac{k'_z}{k_z} &= 1 \\
\frac{k'_z}{k_z}\left(\pm e^{-iHk_z} + 1\right) &= 1 \mp e^{-iHk_z} \\
\frac{k'_z}{k_z} &= \frac{1 \mp e^{-iHk_z}}{1 \pm e^{-iHk_z}} \\
\frac{k'_z}{k_z} &= \frac{1 \mp e^{-iHk_z}}{1 \pm e^{-iHk_z}} \cdot \frac{e^{ik_z\frac{H}{2}}}{e^{ik_z\frac{H}{2}}} \\
\frac{k'_z}{k_z} &= \frac{e^{ik_z\frac{H}{2}} \mp e^{-ik_z\frac{H}{2}}}{e^{ik_z\frac{H}{2}} \pm e^{-ik_z\frac{H}{2}}}. \qquad \text{(A.5)}
\end{aligned}$$

According to equation 2.13 we can write for $\frac{k'_z}{k_z}$

$$\frac{k'_z}{k_z} = \frac{\frac{\omega}{c_0}\sqrt{n'^2 - n_{\mathit{eff}}^2}}{\frac{\omega}{c_0}\sqrt{n^2 - n_{\mathit{eff}}^2}} = \sqrt{\frac{n'^2 - n_{\mathit{eff}}^2}{n^2 - n_{\mathit{eff}}^2}} \qquad \text{(A.6)}$$

and with the relations

$$\sin\alpha = \frac{e^{i\alpha} - e^{-i\alpha}}{2i} \qquad \text{and} \qquad \cos\alpha = \frac{e^{i\alpha} + e^{-i\alpha}}{2} \qquad \text{(A.7)}$$

we can write equation A.5 as follows:

$$\sqrt{\frac{n'^2 - n_{\mathit{eff}}^2}{n^2 - n_{\mathit{eff}}^2}} = \begin{cases} \frac{e^{ik_z\frac{H}{2}} - e^{-ik_z\frac{H}{2}}}{e^{ik_z\frac{H}{2}} + e^{-ik_z\frac{H}{2}}} \\ \\ \frac{e^{ik_z\frac{H}{2}} + e^{-ik_z\frac{H}{2}}}{e^{ik_z\frac{H}{2}} - e^{-ik_z\frac{H}{2}}} \end{cases} \tag{A.8}$$

$$\sqrt{\frac{n'^2 - n_{\mathit{eff}}^2}{n^2 - n_{\mathit{eff}}^2}} = \begin{cases} \frac{2i\sin\left(k_z\frac{H}{2}\right)}{2\cos\left(k_z\frac{H}{2}\right)} \\ \\ \frac{2\cos\left(k_z\frac{H}{2}\right)}{2i\sin\left(k_z\frac{H}{2}\right)} \end{cases} \tag{A.9}$$

$$\sqrt{\frac{n'^2 - n_{\mathit{eff}}^2}{n^2 - n_{\mathit{eff}}^2}} = \begin{cases} i\tan\left(k_z\frac{H}{2}\right) \\ \\ \frac{1}{i}\cot\left(k_z\frac{H}{2}\right). \end{cases} \tag{A.10}$$

$$\tag{A.11}$$

Applying k_z in the form

$$k_z = \frac{\omega}{c_0}\sqrt{n^2 - n_{\mathit{eff}}^2} \tag{A.12}$$

leads to

$$\sqrt{\frac{n'^2 - n_{\mathit{eff}}^2}{n^2 - n_{\mathit{eff}}^2}} = \begin{cases} i\tan\left(\frac{\omega}{c_0}\sqrt{n^2 - n_{\mathit{eff}}^2}\frac{H}{2}\right) \\ \\ \frac{1}{i}\cot\left(\frac{\omega}{c_0}\sqrt{n^2 - n_{\mathit{eff}}^2}\frac{H}{2}\right) \end{cases} \tag{A.13}$$

which we can ultimately write as

$$\sqrt{\frac{n'^2 - n_{\mathit{eff}}^2}{n_{\mathit{eff}}^2 - n^2}} = \tan\left(\frac{H\omega}{2c_0}\sqrt{n^2 - n_{\mathit{eff}}^2}\right) \tag{A.14}$$

$$\sqrt{\frac{n_{\mathit{eff}}^2 - n'^2}{n^2 - n_{\mathit{eff}}^2}} = \cot\left(\frac{H\omega}{2c_0}\sqrt{n^2 - n_{\mathit{eff}}^2}\right). \tag{A.15}$$

These are transcendent equations which have to be solved numerically for n_{eff}.

For the TM polarization the derivation of these equations is carried out in the same way as described above. Applying the Fresnel formulae for TM polarization to equation A.3 yields:

$$\sqrt{\frac{n'^2 - n_{\mathit{eff}}^2}{n_{\mathit{eff}}^2 - n^2}} = n^2\tan\left(\frac{H\omega}{2c_0}\sqrt{n^2 - n_{\mathit{eff}}^2}\right) \tag{A.16}$$

$$\sqrt{\frac{n_{\mathit{eff}}^2 - n'^2}{n^2 - n_{\mathit{eff}}^2}} = n^2\cot\left(\frac{H\omega}{2c_0}\sqrt{n^2 - n_{\mathit{eff}}^2}\right). \tag{A.17}$$

Appendix B

Emission images of the a1aX experiment

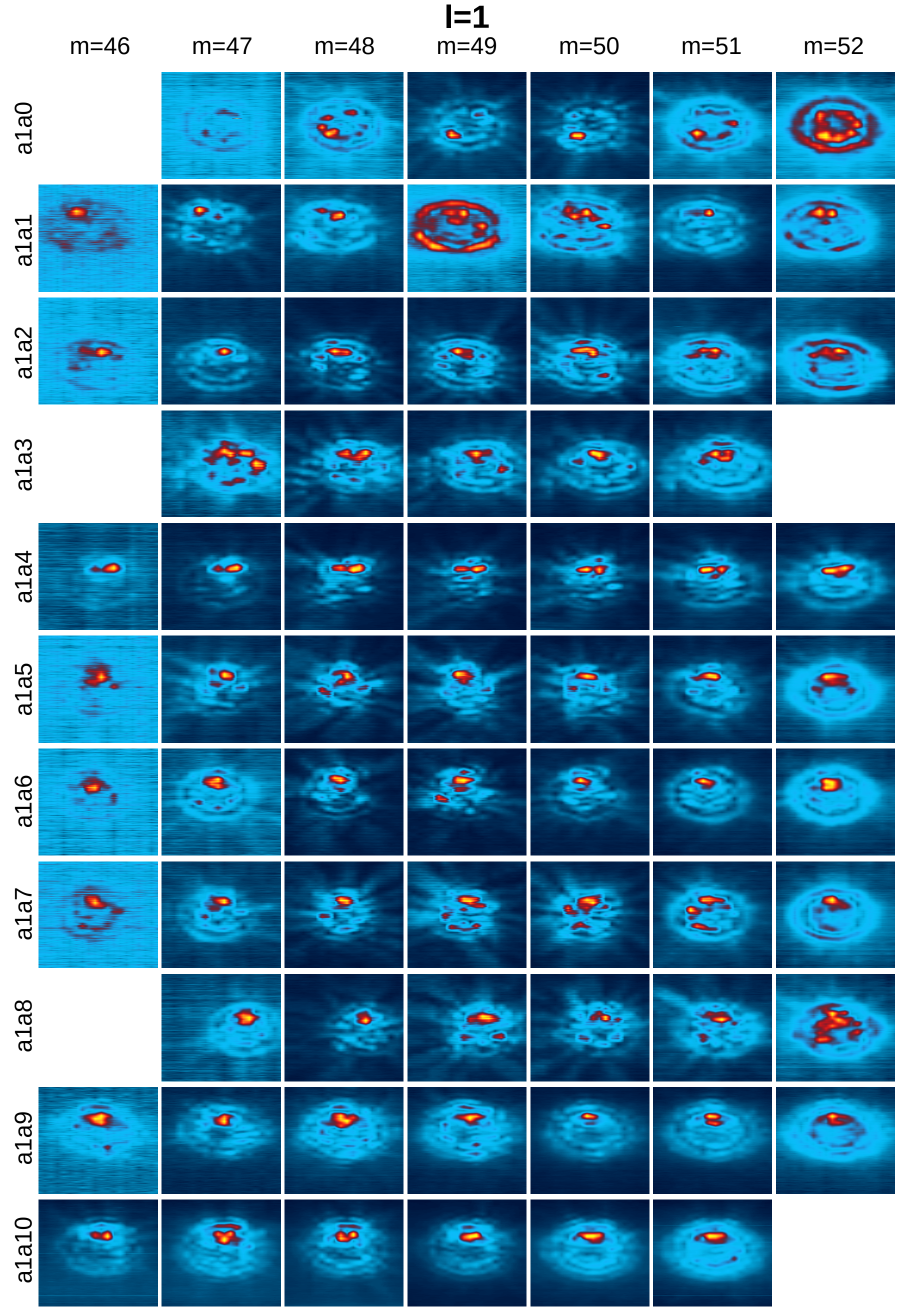

Figure B.1: Emission images of the a1aX experiment, $l = 1$

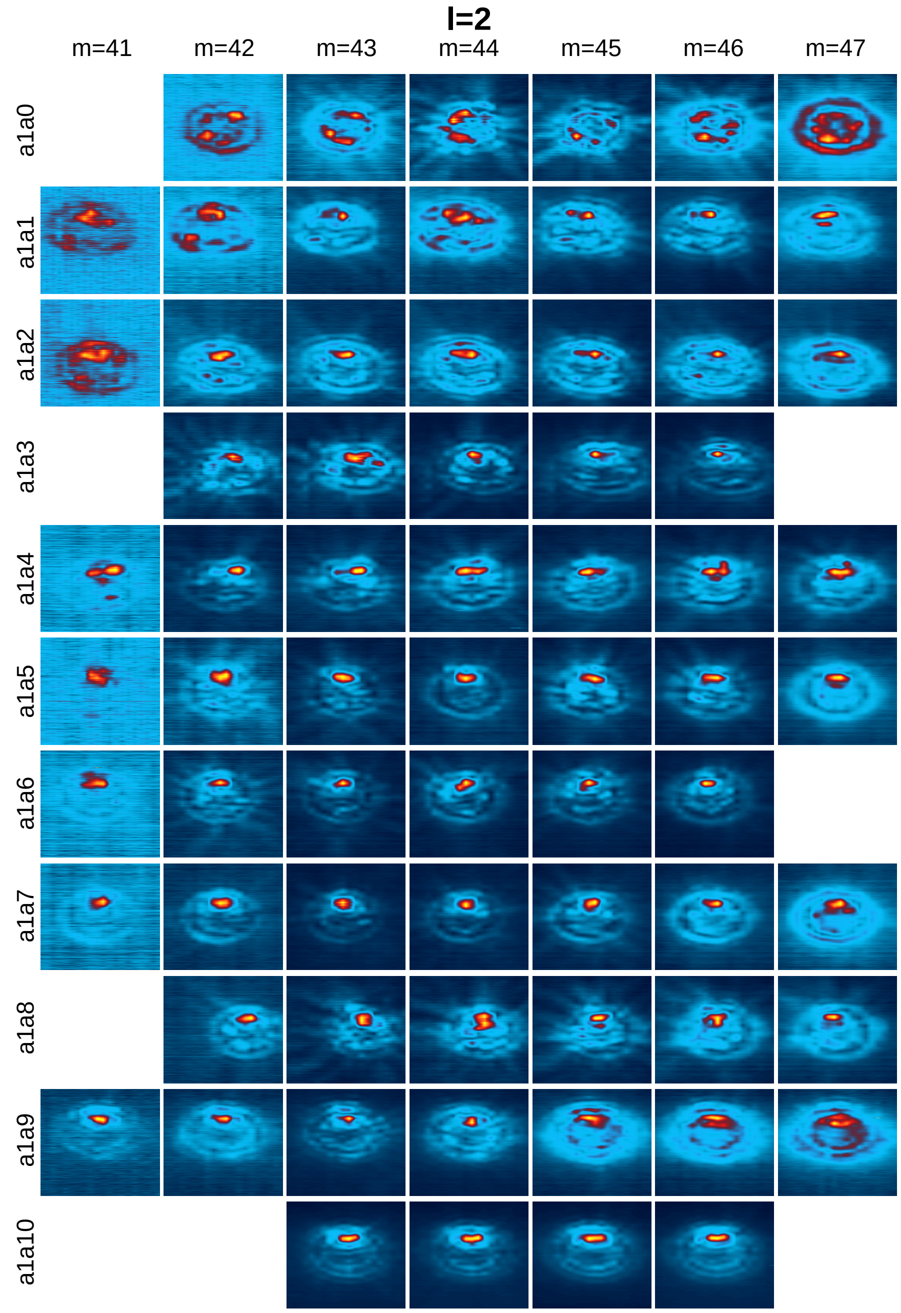

Figure B.2: Emission images of the a1aX experiment, $l = 2$

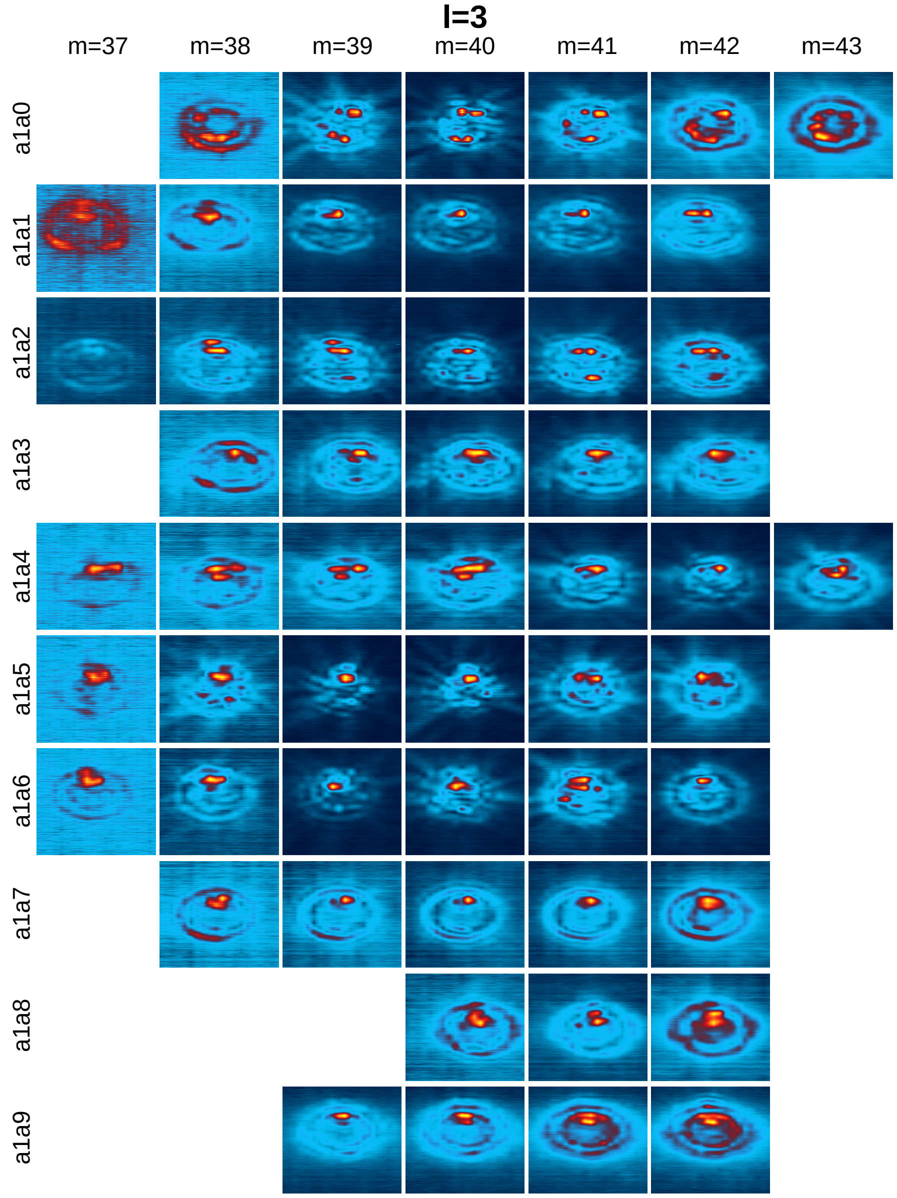

Figure B.3: Emission images of the a1aX experiment, $l = 3$

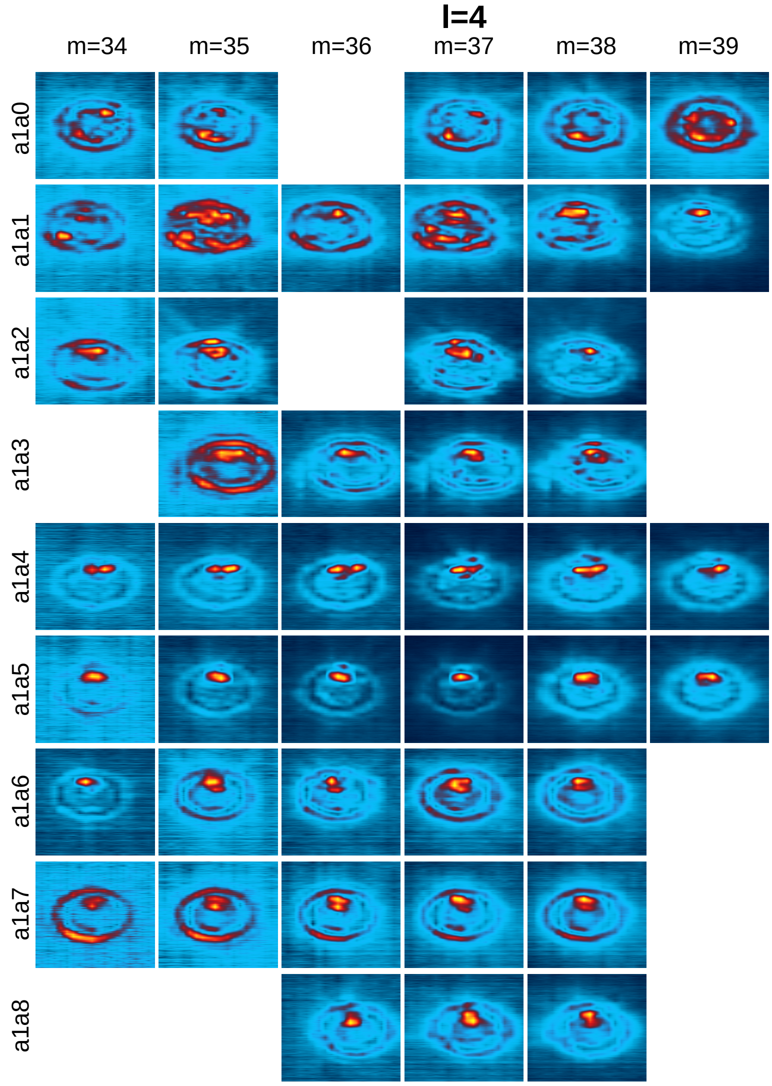

Figure B.4: Emission images of the a1aX experiment, $l = 4$

Appendix C

Experimental data in the a1aX experiment

	$m = 46$	$m = 47$	$m = 48$	$m = 49$	$m = 50$	$m = 51$	$m = 52$
a1a0		1.1977	1.2162	1.2348 1.2348	1.2531	1.2713	1.2893
a1a1	1.1838	1.2022 1.2023	1.2205	1.2384 1.2388	1.2567	1.2745	1.2921
a1a2	1.1828	1.2012	1.2196 1.2197	1.2378 1.2378	1.2557	1.2735 1.2736	1.2913
a1a3	1.2752	1.2023 1.2024	1.2206	1.2386	1.2566 1.2567	1.2744 1.2745	
a1a4	1.1857 1.1858	1.2042	1.2227	1.2408 1.2409	1.2589	1.2768	1.2946
a1a5	1.1867	1.2051 1.2052	1.2235 1.2236	1.2417 1.2418	1.2598 1.2598	1.2776 1.2777	1.2954
a1a6	1.1898	1.3047	1.2268	1.245	1.2631	1.281	1.2988
a1a7	1.1863 1.1864	1.2048 1.2049	1.2233	1.2414	1.2595	1.2774 1.2774	1.2951
a1a8		1.2063	1.2247	1.2429	1.2609	1.2788	1.2965
a1a9	1.1921	1.2106 1.2107	1.2289 1.229	1.2471 1.2471	1.2651	1.283	1.3007
a1a10	1.1943	1.2127	1.2311	1.2492 1.2493	1.2673	1.2852	

Table C.1: Energetic position of the $l = 1$ whispering-gallery modes.

	$m = 46$	$m = 47$	$m = 48$	$m = 49$	$m = 50$	$m = 51$	$m = 52$
a1a0		18923	11198	27474 51495	25132	14104	18002
a1a1	7836.5	22533 27446	14279	8393.3 7479.8	17249	18742	12375
a1a2	10314	7910.1	20467 22271	16548 23338	19477	16860 18615	9551
a1a3	8224	22063 26696	19171	17169	20883 22764	15956 23837	
a1a4	13965 13942	15954	25623	24825 26695	19472	8003.8	7269.2
a1a5	18763	26125 28889	28429 29684	25956 27362	24718 27663	21854 25487	13669
a1a6	15806	7203	23012	22325	14444	8376.4	9493.1
a1a7	28577 29071	27712 29892	27496	24604	25479	23507 24837	10841
a1a8		13411	17517	23374	24386	12588	10216
a1a9	7337	11757 16750	14041 18710	14263 20376	10850	8958	7662.9
a1a10	8214	10981	6861.6	10858 11644	7713.6	5121.5	

Table C.2: Q factors of the $l = 1$ whispering-gallery modes.

	$m = 41$	$m = 42$	$m = 43$	$m = 44$	$m = 45$	$m = 46$	$m = 47$
a1a0		1.2003	1.2195	1.2385	1.2574	1.2761	1.2952
a1a1	1.1869	1.2057	1.2242	1.2426	1.2611	1.2796	1.2978
a1a2	1.2426	1.2049	1.2236	1.242	1.2606	1.279	1.2973
a1a3	1.2752	1.2061	1.2248	1.2433	1.2617	1.28	
a1a4	1.1886	1.2075	1.2264	1.2451	1.2634	1.282	1.3002
a1a5	1.1898	1.2087	1.2277	1.2467	1.2645	1.2829	1.3012
a1a6	1.1926	1.2117	1.2306	1.2493	1.2679	1.2863	
a1a7	1.1891	1.208	1.2268	1.2456	1.2641	1.2825	1.3008
a1a8		1.2099	1.2286	1.2473	1.2658	1.2842	1.3024
a1a9	1.1958	1.2151	1.2337	1.2522	1.2706	1.2889	1.3071
a1a10			1.237	1.2552	1.2736	1.2917	

Table C.3: Energetic position of the $l = 2$ whispering-gallery modes.

	$m = 41$	$m = 42$	$m = 43$	$m = 44$	$m = 45$	$m = 46$	$m = 47$
a1a0		10152	17931	19410	22272	22220	6799.4
a1a1	8431.9	10794	12619	10382	13012	13257	12710
a1a2	10021	11237	6728.3	6531.8	10752	9801.6	9000.1
a1a3	8224	27257	21393	16421	10758	7417.4	
a1a4	9075.4	7261.8	10022	7704.5	4396	8023.1	8435.3
a1a5	12228	15067	14560	6611.5	11040	16633	7791.6
a1a6	9381.3	14213	14113	11918	14031	9209	
a1a7	8530.3	13676	17346	14564	11478	8068.8	6492.1
a1a8		10803	22301	16349	13999	10951	6542.6
a1a9	2598.5	2005.5	9305.2	12818	10788	5888.3	4784.2
a1a10			2593.5	2303.6	2408.2	2196.7	

Table C.4: Q factors of the $l = 2$ whispering-gallery modes.

	$m = 37$	$m = 38$	$m = 39$	$m = 40$	$m = 41$	$m = 42$	$m = 43$
a1a0		1.2039	1.2235	1.243	1.2625	1.2822	1.3002
a1a1	1.1925	1.2108	1.2295	1.2483	1.267	1.2858	
a1a2	1.1915	1.2099	1.2286	1.2475	1.2662	1.2849	
a1a3	1.2752	1.212	1.2302	1.2487	1.2672	1.2858	
a1a4	1.1927	1.2118	1.2309	1.2499	1.2689	1.2877	1.3064
a1a5	1.1938	1.213	1.2322	1.2513	1.2702	1.2891	
a1a6	1.1967	1.216	1.2352	1.2544	1.2734	1.2922	
a1a7		1.2134	1.2325	1.2513	1.2705	1.2891	
a1a8				1.2546	1.2731	1.2918	
a1a9			1.2383	1.257	1.2745	1.2954	
a1a10							

Table C.5: Energetic position of the $l = 3$ whispering-gallery modes.

	$m = 37$	$m = 38$	$m = 39$	$m = 40$	$m = 41$	$m = 42$	$m = 43$
a1a0		16160	18322	22199	16172	11981	8817.7
a1a1	8273.2	10433	10983	9031.6	12103	6751.8	
a1a2	3371.5	8042.7	12603	17310	13142	12617	
a1a3	8224	10739	10219	11147	10388	9646.9	
a1a4	3120.9	3470.5	9239.5	8181.3	6262.7	9120.2	6627.5
a1a5	13659	15303	20615	15395	22403	14505	
a1a6	7745.9	8920.8	13537	15194	18398	15335	
a1a7		3084.9	2172.6	2477.1	3479.5	6157.2	
a1a8				1426.9	2452.6	1140.8	
a1a9			814.9	735.62	1691.1	350.65	
a1a10							

Table C.6: Q factors of the $l = 3$ whispering-gallery modes.

	$m = 34$	$m = 35$	$m = 36$	$m = 37$	$m = 38$	$m = 39$	$m = 40$
a1a0	1.2192	1.2364		1.256	1.2757	1.2945	
a1a1	1.2066	1.2265 1.2267	1.2465	1.2625	1.2813	1.3001	
a1a2	1.2062	1.2241		1.2612	1.28		
a1a3		1.2269	1.2447	1.263	1.2816		
a1a4	1.206	1.225	1.2442	1.2638	1.2828	1.3018	
a1a5	1.2073	1.2266	1.2457	1.2656	1.2849	1.3038	
a1a6	1.2105	1.2299	1.2501	1.269	1.2886		
a1a7	1.2115	1.2298	1.2484	1.2672	1.2857		
a1a8			1.2518	1.2706	1.2893		
a1a9							
a1a10							

Table C.7: Energetic position of the $l = 4$ whispering-gallery modes.

	$m = 34$	$m = 35$	$m = 36$	$m = 37$	$m = 38$	$m = 39$	$m = 40$
a1a0	10957	7579.3		3541.9	8650.1	11758	
a1a1	6196.4	16736 7557.4	3143.4	11932	12495	10547	
a1a2	11377	4766.7		7066.8	4575.5		
a1a3		8317.8	5972.6	7779.7	9561.4		
a1a4	3657.5	3864.1	3483.1	3440.4	1672.2	3322.6	
a1a5	2805.5	4715.3	5296.5	5878.4	6019.2	3968.5	
a1a6	6482.7	3875.5	4956.2	6720.4	1506.6		
a1a7	1137.5	2965.1	1830.1	2321.9	2823.5		
a1a8			1326.8	2010.7	2222.5		
a1a9							
a1a10							

Table C.8: Q factors of the $l = 4$ whispering-gallery modes.

	Laser	λ/nm	I/mW	T/K	t_{exp}/s	Slices
a1a0	Ti:Sa	767.2	50	4.3	5	20
a1a1	Ti:Sa	767.2	70	4.4	2	20
a1a2	Ti:Sa	767.2	50	5.0	5	20
a1a3	Ti:Sa	767.2	50	6.0	5	20
a1a4	Ti:Sa	767.2	48	4.3	5	20
a1a5	Ti:Sa	767.2	46.5	4.3	5	20
a1a6	Ti:Sa	767.2	46.5	4.3	5	20
a1a7	Ti:Sa	767.2	46.5	4.3	5	20
a1a8	Ti:Sa	767.2	47.5	4.3	5	20
a1a9	$HeNe$	632	0.268	4.7	6	20
a1a10	$HeNe$	632	0.256	4.6	29	20

Table C.9: Experimental setup parameters in the a1aX experiment.

Bibliography

[1] Kerry J. Vahala. Optical microcavities. *Nature*, 424(6950):839–846, 2003. doi: 10.1038/nature01939.

[2] S. L. McCall, A. F. J. Levi, R. E. Slusher, S. J. Pearton, and R. A. Logan. Whispering-gallery mode microdisk lasers. *Applied Physics Letters*, 60(3):289–291, 1992. doi: 10.1063/1.106688.

[3] V.S. Ilchenko and A.B. Matsko. Optical resonators with whispering-gallery modes-part ii: applications. *Selected Topics in Quantum Electronics, IEEE Journal of*, 12 (1):15–32, Jan.-Feb. 2006. ISSN 1077-260X. doi: 10.1109/JSTQE.2005.862943.

[4] G. D. Chern, H. E. Tureci, A. Douglas Stone, R. K. Chang, M. Kneissl, and N. M. Johnson. Unidirectional lasing from InGaN multiple-quantum-well spiral-shaped micropillars. *Applied Physics Letters*, 83(9):1710–1712, 2003. doi: 10.1063/1.1605792.

[5] M. Kneissl, M. Teepe, N. Miyashita, N. M. Johnson, G. D. Chern, and R. K. Chang. Current-injection spiral-shaped microcavity disk laser diodes with unidirectional emission. *Applied Physics Letters*, 84(14):2485 – 2487, 2004. doi: 10.1063/1.1691494.

[6] Chil-Min Kim, Jinhang Cho, Jinhyung Lee, Sunghwan Rim, Sang Hun Lee, Kwang Ryung Oh, and Jong Hoi Kim. Continuous wave operation of a spiral-shaped microcavity laser. *Applied Physics Letters*, 92(13):131110, 2008. doi: 10.1063/1.2902174.

[7] Jens U. Nöckel, A. Douglas Stone, Gang Chen, Helene L. Grossman, and Richard K. Chang. Directional emission from asymmetric resonant cavities. *Opt. Lett.*, 21(19):1609, 1996. URL `http://ol.osa.org/abstract.cfm?URI=ol-21-19-1609`.

[8] Claire Gmachl, Federico Capasso, E. E. Narimanov, Jens U. Nöckel, A. Douglas Stone, Jérôme Faist, Deborah L. Sivco, and Alfred Y. Cho. High-power directional emission from microlasers with chaotic resonators. *Science*, 280(5369):1556–1564, 1998. doi: 10.1126/science.280.5369.1556.

[9] Jan Wiersig and Martina Hentschel. Combining directional light output and ultralow loss in deformed microdisks. *Physical Review Letters*, 100(3):033901, 2008. doi: 10.1103/PhysRevLett.100.033901.

[10] M. S. Kurdoglyan, Soo-Young Lee, Sunghwan Rim, and Chil-Min Kim. Unidirectional lasing from a microcavity with a rounded isosceles triangleshape. *Opt. Lett.*, 29(23): 2758–2760, 2004. doi: 10.1364/OL.29.002758.

[11] Jan Wiersig and Martina Hentschel. Unidirectional light emission from high-Q modes in optical microcavities. *Physical Review A*, 73(3):031802, 2006. doi: 10.1103/PhysRevA.73.031802.

[12] Lord Rayleigh. The problem of the whispering gallery. *Philos. Mag.*, 20:1001, 1910.

[13] Max Born and Emil Wolf. *Principles of optics.* Cambridge Univ. Press, 7 edition, 1999.

[14] R. E. Slusher, A. F. J. Levi, U. Mohideen, S. L. McCall, S. J. Pearton, and R. A. Logan. Threshold characteristics of semiconductor microdisk lasers. *Applied Physics Letters*, 63(10):1310–1312, 1993. doi: 10.1063/1.109714.

[15] A. N. Pikhtin and A. D. Yas'kov. *Sov. Phys. Semicond.*, 14(4):389–392, 1980.

[16] Martina Hentschel. *Mesoscopic wave phenomena in eletronic and optical ring structures.* PhD thesis, Technische Universität Dresden, 2002.

[17] John D. Jackson. *Classical Electrodynamics.* John Wiley and Sons, New York, 3rd edition, 1999.

[18] Tobias Kipp. *Lateral strukturierte Halbleiter-Mikroresonatoren.* PhD thesis, Universität Hamburg, 2004.

[19] B. Gayral, J. M. Gerard, A. Lemaitre, C. Dupuis, L. Manin, and J. L. Pelouard. High-Q wet-etched GaAs microdisks containing InAs quantum boxes. *Applied Physics Letters*, 75(13):1908–1910, 1999. doi: 10.1063/1.124894.

[20] TD Lee, PH Cheng, JS Pan, RS Tsai, Y Lai, and K Tai. Far-field emission narrowing effect of microdisk lasers. *Applied Physics Letters*, 72:2223–2225, 1998. doi: 10.1063/1.121328.

[21] E. Peter, A. Dousse, P. Voisin, A. Lemaître, D. Martrou, A. Cavanna, J. Bloch, and P. Senellart. Highly directional radiation pattern of microdisk cavities. *Applied Physics Letters*, 91:151103, 2007. doi: 10.1063/1.2789956.

[22] Jens U. Nöckel and A. Douglas Stone. Ray and wave chaos in asymmetric resonant optical cavities. *Nature*, 385(2):45–47, January 1997. doi: 10.1038/385045a0.

[23] N. B. Rex, H. E. Tureci, H. G. L. Schwefel, R. K. Chang, and A. Douglas Stone. Fresnel filtering in lasing emission from scarred modes of wave-chaotic optical resonators. *Phys. Rev. Lett.*, 88(9):094102, Feb 2002. doi: 10.1103/PhysRevLett.88.094102.

[24] Jan Wiersig. Boundary element method for resonances in dielectric microcavities. *Journal of Optics A: Pure and Applied Optics*, 5(1):53–60, 2003. doi: 10.1088/1464-4258/5/1/308.

[25] X. S. Wu, L. A. Coldren, and J. L. Merz. Selective etching characteristics of HF for $\text{Al}_x\text{Ga}_{1-x}\text{As}$. *Electronics Letters*, 21(13), 1980.

[26] Brent E. Little and Sai T. Chu. Estimating surface-roughness loss and output coupling in microdisk resonators. *Opt. Lett.*, 21(17):1390, 1996. URL `http://ol.osa.org/abstract.cfm?URI=ol-21-17-1390`.

[27] Y. P. Varshni. Temperature dependence of the energy gap in semiconductors. *Physica*, 34:149, 1967.

[28] T. Kipp, H. Welsch, Ch. Strelow, Ch. Heyn, and D. Heitmann. Optical modes in semiconductor microtube ring resonators. *Physical Review Letters*, 96(7):077403, 2006. doi: 10.1103/PhysRevLett.96.077403.

[29] H. Cao, J. Y. Xu, W. H. Xiang, Y. Ma, S.-H. Chang, S. T. Ho, and G. S. Solomon. Optically pumped InAs quantum dot microdisk lasers. *Applied Physics Letters*, 76 (24):3519–3521, 2000. doi: 10.1063/1.126693.

[30] P. Michler, A. Kiraz, Lidong Zhang, C. Becher, E. Hu, and A. Imamoglu. Laser emission from quantum dots in microdisk structures. *Applied Physics Letters*, 77(2): 184–186, 2000. doi: 10.1063/1.126918.

[31] Matthew Borselli, Thomas Johnson, and Oskar Painter. Beyond the rayleigh scattering limit in high-Q silicon microdisks: theory and experiment. *Opt. Express*, 13 (5):1515–1530, 2005. doi: 10.1063/1.1811378.

[32] C. P. Michael, K. Srinivasan, T. J. Johnson, O. Painter, K. H. Lee, K. Hennessy, H. Kim, and E. Hu. Wavelength- and material-dependent absorption in GaAs and AlGaAs microcavities. *Applied Physics Letters*, 90(5):051108, 2007. doi: 10.1063/1.2435608.

Acknowledgments

This thesis would not have been written without the help of a lot of people. I especially wish to thank:

Prof. Dr. Detlef Heitmann for his support and for giving me the opportunity to do my PhD thesis in his research group,

Prof. Dr. Ulrich Merkt for being second referee of my dissertation and for helping me to actually get things done,

Prof. Dr. Wolfgang Hansen for being the second referee of my disputation,

Prof. Dr. Jan Wiersig for bringing my attention to pierced microdisks, for fruitful discussions and help on this subject,

Dr. Tobias Kipp for his outstanding supervision and informative discussions,

Chrstian Strelow for his formidable help with physical questions and for the simulations,

the MBE Team –most notably Dr. Christian Heyn, Dr. Andreas Schramm and Dr. Holger Welsch– for providing me with samples,

all my colleagues and lab partners for providing the enjoyable and motivating working environment in which I had the pleasure to work,

the DFG for financing my work within the Graduiertenkollegs 463 and 1286,

Timo Kökenhoff and Tobias Krohn for trouble-free teamwork with sometimes troublesome computer systems,

Tim Köppen, Christian Strelow, Nis Kötting and Birte Pawlack for proofreading my thesis,

all my friends and my family for their support,

Birte for her love, patience and for being there.